1-1-1971

Light Scattering and Microscopic Investigations of Mesophase Transitions of Cholesteryl Myristate.

Saleh Abd el Karim Jabarin
University of Massachusetts Amherst

LIGHT SCATTERING AND MICROSCOPIC INVESTIGATIONS OF MESOPHASE TRANSITIONS OF CHOLESTERYL MYRISTATE

A Dissertation Presented

By

SALEH ABD el KARIM JABARIN

Submitted to the Graduate School of the
University of Massachusetts in
partial fulfillment of the requirements for the degree of

DOCTOR OF PHILOSOPHY

August 1971

Major Subject: Polymer Science & Engineering

LIGHT SCATTERING AND MICROSCOPIC INVESTIGATIONS OF MESOPHASE TRANSITIONS OF CHOLESTERYL MYRISTATE

A Dissertation Presented

By

SALEH ABD el KARIM JABARIN

Approved as to style and content by:

Richard S. Stein
(Chairman of Committee)

Roger S. Porter
(Head of Department)

Robert L. Powell
(Member)

James A. Faucett
(Member)

August 1971

ACKNOWLEDGEMENTS

I gratefully acknowledge the help, encouragement and guidance of Professor Richard Stein, who directed this project. I also thank Professor F. Price for his helpful suggestions. I sincerely appreciate the encouragements of Professors R.S. Porter and R. Rowell. Thanks to Dr. J. Wendorff for stimulating discussions throughout this research.

I am grateful to my wife Dorothy for proofreading and typing the manuscript, and to Mrs. Donna Wolf for her help in typing this thesis.

I would like to acknowledge with thanks the financial support of Xerox Corporation during the three years of the study.

TABLE OF CONTENTS

ABSTRACT

LIGHT SCATTERING AND MICROSCOPIC INVESTIGATIONS

OF

MESOPHASE TRANSITIONS OF CHOLESTERYL MYRISTATE

By

SALEH ABD el KARIM JABARIN

Advisor: R.S. Stein

Submitted in partial fulfillment of the requirements

for the degree of Doctor of Philosophy

The solid state of cholesteryl myristate may exist in a negatively birefringent spherulitic form of randomly and non-randomly correlated aggregates of crystals best characterized by an orientation correlation distance which was found to be in the order of 1 micron.

Cholesteryl myristate exhibits a smectic and cholesteric mesophase both when heating from the solid and when cooling from the isotropic melt. The morphology of the smectic phase is the same upon heating and cooling. It is best described as consisting of regions having crystal orientation randomly correlated. For the cholesteric phase, however, non-randomness leads to correlated regions having definite shape. On heating to the cholesteric phase there is a transition from the solid state or the smectic phase to a cholesteric phase having disc-like non-random orientation correlation. The isotropic--

cholesteric phase transition, occuring on cooling, on the other hand, occurs in two steps. The first is a rapid transformation to a turbid "blue" homeotropic state consisting of particles of sizes less than one micron, while the second is a much slower transition to a more macroscopically ordered focal-conic spherulitic state. The latter transformation may be described by nucleation and growth kinetics similar to those obeyed by crystalline polymers. The process can be followed by direct microscopic observation, by the depolarized light transmission technique or by the low angle light scattering procedure. The light scattering is similar to that observed for a spherulitic polymer and is shown to arise principally from fluctuation in the orientation direction of anisotropic structures. Spherulite sizes, orientation of the optic axes, and kinetic parameters are determined. The kinetics of transformation fit the Avrami equation giving an n value of 3. The analysis of the temperature dependence of the growth and nucleation rates yields very small small interfacial energy products, $\sigma_1 \sigma_2$, of 0.1 and 0.2 erg^2/cm^4 for growth and nucleation respectively.

DEDICATION

Dedicated to my parents, Abd el Karim and Khadra Jabarin, for their encouragement and sacrifices over the years, and to my wife, Dorothy, for her encouragement in pursuing higher education.

C H A P T E R I

INTRODUCTION

A. General Properties of Liquid Crystals

Liquid crystals are materials that exhibit properties typical of liquids, such as the ability to flow, and many of the properties of crystals, such as molecular order. A material capable of exhibiting liquid crystalline phases, or as they are more properly called "mesomorphic" states, passes through one or more "mesophases" on heating before becoming an isotropic liquid. These mesophases occur at reproducible temperatures.

Liquid crystals were first discovered by the Austrian botanist, Friedrich Reinitzer,[1] in 1888. He observed that the compound, cholesteryl benzoate, appeared to have two distinct melting points. The solid material became a cloudy liquid at 145°C and on further heating turned into a clear liquid at 179°C. Lehmann[2] in 1889 showed that the cloudy intermediate phase contained regions which have crystalline-like properties such as moelcular anisotropy. He suggested the name "liquid crystals".

The reason for the existence of the mesomorphic states is qualitatively explained[3] by the molecular arrangement of the compounds which exhibit a liquid crystalline behavior. It is found that these compounds have molecules that are elongated, and in some cases flattened, and which contain

one or more polar groups.[3,4] The geometry of the molecules favors a parallel alignment to one another. In the crystalline state, the molecules are arranged parallel to one another and are held together by local attachments due to the polar groups and also by Van der Waals attraction forces. Therefore, on heating the material to the liquid state characterized by random arrangement of molecules, the transition occurs in stages. The weaker attachments break first and leave the molecules with some freedom of movement before sufficient thermal energy is acquired to overcome the tendency toward parallel arrangement. In other words, the system has the ability to flow but remains birefringent because the molecules have a preferred orientation.

Based on a classification proposed by Friedel[5] in 1922, three types of liquid crystalline states or mesophases are recognized. These are the smectic (soap-like), nematic (thread-like), and the cholesteric mesophases.

In the smectic mesophase, the molecules are arranged side-by-side in a series of stratified layers.[3,6,7] The long axes of the molecules are paralled to one another and perpendicular to the plane of its layer, giving two-dimensional order. The molecules may be arranged, however, either in regular rows or in random formation within each layer. In some smectic mesophases, the molecules are further ordered by being arranged in paired rows within individual layers.[4,6]

Under polarized light, the smectic mesophase behaves optically like a crystalline material. The velocity of light transmitted along the long axes of the molecules is slower than the velocity across the long axis. Such materials are optically positive.

The molecules in the nematic mesophase, have their long axes parallel, but they are not separated into distinct layers as the molecules of the smectic phase. Thus one-dimensional order rather than two-dimensional order occurs. Nematic liquid crystals are also optically positive.

The cholesteric mesophase is exhibited by derivatives of cholesterol, but not by cholesterol itself. In the cholesteric mesophase, the molecules are arranged in layers.(6) In each layer the molecules have their long axis parallel to the plane of the layer, but not arranged in regular rows. The side chain methyl groups which project from the plane of the molecule cause the long axes of successive layers to be displaced slightly, so that consecutive displacement traces out a helical path.(6) The unique molecular architecture of cholesteric liquid crystals gives rise to a number of peculiar optical properties(6) which include optical activity, circular dichroism and birefringence. The optical sign of the cholesteric phase is negative.

The birefringence, or double refraction, is shown by all three types of liquid crystals. Depending on conditions, a specific mesophase may exhibit a series of textures or

birefringent patterns under crossed polaroids. These textural variations within a mesophase have been explained by suggesting that the increase in temperature causes a decrease in lateral order and an increase in flexibility of the layers, thus permitting the possible adoption of a different molecular arrangement.[8] Therefore, liquid crystals or mesophases are characterized by two levels of order. A short range order (as measured by x-rays) characteristic of distance between molecules and layers as well as the orientation of molecules with respect to each other. The second is the existence of long range order (10^3 A^o and above) responsible for the scattering of visible light observed in the mesophases.

Chatelain[9,10] has studied the angular dependence of the scattered intensity of a nematic liquid crystal. His results indicate that the scattered intensity is very strong at low angles and that liquid crystals strongly depolarize light. deGennes and the Orsay Liquid Crystal Group[11,12] have made theoretical calculations of long wavelength order fluctuations in nematic systems and they were able to explain Chatelain's measurements.

Stein, et al,[13,14] have studied the light scattering from a series of cholesteryl esters. The results indicate that the scattering arises from the existence of regions having correlated orientation with dimensions comparable to the wavelength of light.

B. Objectives

The objectives of this thesis are to study; (i) the molecular ordering in a cholesteric liquid crystal system from the point of view of characterizing the size and the orientation of the ordered regions in each of the mesophases exhibited by the system as well as the solid state, (ii) the effect of thermal history on the orientation of the ordered regions of the mesophases, and (iii) kinetics of the isotropic--cholesteric phase transition.

C. Methods of Characterization

The optical properties resulting from molecular ordering in liquid crystals were described above. It was shown that liquid crystals are optically heterogeneous and exhibit scattering of visible light. Therefore the light scattering methods offer a convenient way to study the structure of liquid crystals. It has been shown[13,14,15] that the statistical approach inherent in certain theories of the scattering from solid polymers was ideally suited to characterize the dimensions, shape and arrangement of the oriented regions.

Two kinds of light scattering methods were employed in this study, the photographic and the photometric techniques. The photographic method is a convenient means of rapidly but qualitatively recording the scattering pattern and its changes with time and temperature. The photometric

technique, on the other hand, involves the measurement of the absolute scattering intensity as a function of the scattering angle as well as the polarization angle. The exact description of each method will be given later.

The polarizing microscope was used to study the textural variation of the mesophases upon heating and cooling. Also, it was used to follow the formation and the sizes of oriented regions as a function of time and temperature.

Depolarized light intensity transmission was used to study the kinetics of the isotropic--cholesteric phase transition.

C H A P T E R I I

EXPERIMENTAL

A. Material

The cholesteryl ester chosen for this study is cholesteryl myristate. This material was supplied by Applied Science Laboratories, State College, Pa., Lot 648-38. The laboratory had purified the sample by column chromatography and proved the purity to be better than 99% by thin layer chromatography. The purity was confirmed by Barrall *et al*,[16] using spectrometric analyses. However, more recent work by Davis and Porter[63] indicated that the purity was 98.1% as determined by the shape of the differential scanning calorimetric curves. This latter value is probably more accurate since the melting point depression reflects impurities due to isomers not detected by chromatography.

Cholesteryl myristate was chosen from among other esters because it exhibits three sharp reversible transitions in a convenient range of temperatures. The transition temperatures are:

$$\text{Solid} \underset{73.6^{o}C}{\longleftrightarrow} \text{Smectic Mesophase} \underset{79.7^{o}C}{\longleftrightarrow} \text{Cholesteric Mesophase} \underset{84^{o}C}{\longleftrightarrow} \text{Isotropic Liquid}$$

The chemical structure of cholesteryl myristate is given below; it has a molecular weight of 579.03.

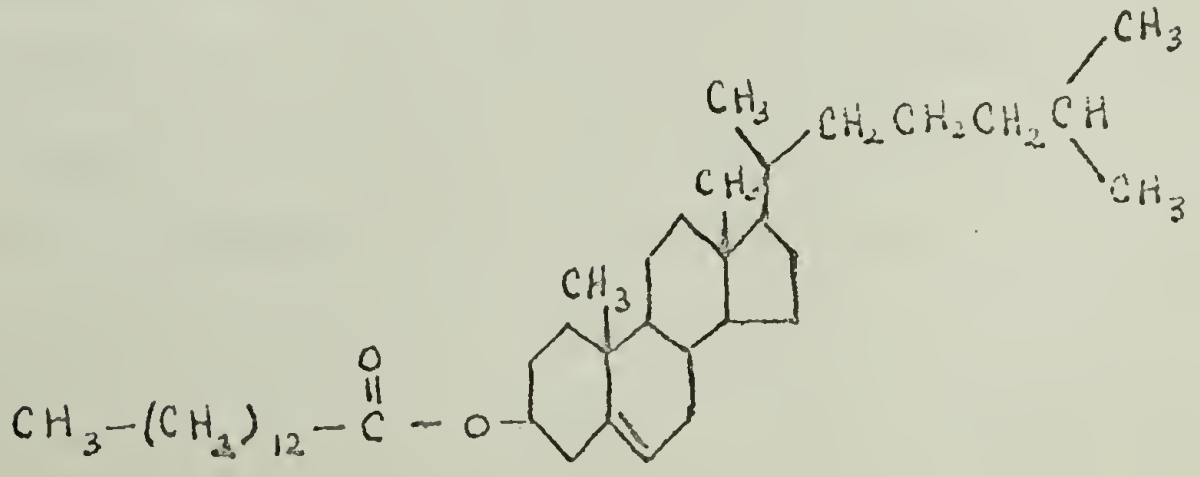

The refractive index is 1.504, calculated from the Lorentz and Lorenz equation.

To study the inherent properties of cholesteryl esters, it is very important that they be pure. If a cholesteryl is not really pure one can observe transitional peculiarities such as extra mesophases or missing mesophases as has been shown by Davis and Porter.[17]

B. Preparation of Samples and Treatment of Cover Slips

Samples for both light scattering and microscopy work were prepared between microscope cover slips. The material in stock is in the form of a powder. Tha material was heated to about 5°C above the melting point, namely 90°C, and held at this temperature for half an hour. The sample was then cooled quickly to the desired temperature. The thickness of the sample was controlled using copper and brass spacers. The thicknesses covered the range 0.5 mil to 12 mils. Detailed information concerning the heat treatment of the samples will be given in later parts of this thesis.

For study of the solid state, this procedure was followed to prepare samples. A small amount of the powder was placed on a microscope cover slide and then heated slowly to the isotropic melting point. Another cover slip was placed on top with a minimum amount of disturbance, then the temperature was raised to 90°C for a few minutes. The sample was then cooled at the rate of 2°/min. to room temperature. An

immersion oil of matching refractive index, such as silicon oil was used on some samples to fill voids or cracks in the sample.

The cover slips were cleaned with potassium permanganate sulfuric acid solution and rinsed with distilled water, then dried between lens paper in a desicator.

C. Microscopy

The photomicrographs were obtained using a Carl Zeiss polarizing microscope type Standard WL in combination with a Mettler Fp2 hot stage. The microscope is equipped with an attachment camera. The films used were of the type Kodak Plus-X Pan black and white panchromatic film 24x36mm. The photomicrographs were taken when the polarizer and analyzer were crossed.

D. Depolarized Light Intensity

The depolarized light intensity was measured by a photoelectric light measuring device. The measurements were made possible by equipping the microscope with a beam splitter. The light measuring device consists of a vacuum photoelectric cell and a four stage photometer. The photometer device amplifies the photoelectric current and indicates it on a micro ammeter. The angular aperature is 9^{o} for the 0.16 numerical aperature objective lens used in this study.

E. Photographic Light Scattering

The light scattering pictures were taken by using the small angle photographic light scattering apparatus which has been described elsewhere.[18] Basically it consists of a light source which is a Spectra-Physics Model 130 helium--neon gas laser for which $\lambda_o = 6358A^o$, rotating analyzer type HN36 plastic mounted polaroid and photographic film. Stray radiation was eliminated by passing the incident laser beam through a 1--2 mm. pinhole located about 1 cm. below the sample. The exposure time was regulated by a camera type shutter. The patterns were recorded on 4 x 5" Polaroid Land Film Type 57.

F. Photometric Light Scattering

The photometric light scattering measurements were conducted using the low-angle light scattering apparatus, which is a modification of the low-angle instrument described originally by Plaza and Stein[19] and it was more fully described by Chu.[18] A brief description and the calibration of the aparatus are given in Appendix I.

C H A P T E R I I I

THEORY OF LIGHT SCATTERING

The amplitude of scattered light by the ith volume element of a system is given by the Rayleigh approximation as follows:[20]

$$A_i = K(\vec{M}_i \cdot \vec{O}) \cos k(\vec{r}_i \cdot \vec{s}) \qquad \text{(III-1)}$$

where $\vec{M}_i$ is the induced dipole moment in the ith volume elementat a distance $\vec{r}_i$ from an origin; $k = 2\pi/\lambda$, where λ is the wavelength in the medium; $\vec{s} = \vec{s}' - \vec{s}_o$, where $\vec{s}'$ and $\vec{s}_o$ are unit vectors along the scattered and incident beams; and $\vec{O}$ is a unit vector perpendicular to the scattered light beam and along the polarization direction. A more accurate definition of $\vec{O}$ has been given by Prins and co-workers.[21] The vector $\vec{O}$ has two components and they are defined as follows:

$\vec{O}_{\parallel}$ is a vector perpendicular to the scattered beam lying parallel to the plane of $\vec{s}'$ and of the incident polarization direction. $\vec{O}_{\perp}$ is a vector perpendicular to the scattered beam lying perpendicular to the plane of $\vec{s}'$ and of the incident polarization direction. The consequences of the two definitions of the $\vec{O}$ vector will be discussed in the next section.

K is a constant and the induced dipole $\vec{M}_i$ is given by

$$\vec{M}_i = |\alpha_i| \vec{E}_i \qquad \text{(III-2)}$$

where $\vec{E}_i$ is the incident electric field of the light wave and $|\alpha_i|$ is the polarizability tensor of the ith element.

The total scattering may be calculated by two approaches, The "model" approach and the statistical approach.

A. Model Approach

In the model approach one assumes a scattering entity and the experiments are used to determine parameters defining the model. The calculation of the total scattering involves summing A_i over all elements of the system to obtain an expression for the total amplitude, which is then squared to obtain the intensity.

The scattering from anisotropic spheres. The scattering from spheres having different radial and tangential polarizabilities, α_r and α_t, have been calculated.[22] The equations for I_{Vv} and I_{Hv} are given by:

$$I_{Vv} = K' v_o^2 (3/U^3)^3 [(\alpha_t - \alpha_s)(2\sin U - U\cos U - \mathrm{Si}U) + (\alpha_r - \alpha_s)(\mathrm{Si}U - \sin U) + (\alpha_t - \alpha_r)\cos^2(\theta/2) \cos^2\mu\ (4\sin U - U\cos U - 3\mathrm{Si}U)]^2 \quad \text{(III-3)}$$

$$I_{Hv} = K v_o^2 (3/U^3)^2 [(\alpha_t - \alpha_r)\cos^2(\theta/2)\sin\mu\cos\mu\ (4\sin U - U\cos U - 3\mathrm{Si}U)]^2 \quad \text{(III-4)}$$

where v_o is the volume of the sphere; $U = 4\pi R/\lambda)\sin(\theta/2)$; where R is the radius of the sphere; λ is the wavelength of the light in the medium; and θ is the polar scattering angle. α_t, α_r and α_s are the tangential and radial polarizabilities of the sphere and the polarizability of the surroundings. μ is the azimuthal scattering angle. It is assumed that α_t, α_r and α_s are sufficiently close together that the light wave is not affected appreciably on passing through the sphere

boundary, so that the Rayleigh-Gans approximation can be used for calculation of the scattering. Vv designates the polarization direction of the incident and scattered beams as vertical and Hv designates horizontal polarization of the scattered beam. SiU designates the integral

$$SiU = \int_0^u \frac{\sin x}{x}\, dx \qquad \text{(III-5)}$$

It is seen that I_{Hv} arises entirely from the anisotropy of the spherulite and depends strongly upon the azimuthal angle μ. I_{Vv}, on the other hand, contains three terms, the last of which arises from anisotropy and is dependent upon μ. The first two terms in I_{Vv} depend upon the difference between the spherulite polarizabilities and that of the surroundings, and they are independent of μ.

Equation III-4 for Hv scattering predicts that at a particular μ, the intensity of scattering will go through a maximum with increasing scattering angle θ. The intensity is zero at zero angle ($U = 0$) and at large angle ($U \to \infty$). This results from the dependency of the term $3/U^3(4\sin U - U\cos U - 3SiU)$ on U. The maximum intensity occurs at U=4.1. This corresponds to a scattering angle θ_m given by:

$$(4\pi R/\lambda)\sin(\theta_m/2) = 4.1 \qquad \text{(III-6)}$$

Therefore, the determination of the angular position of the scattering maximum serves to characterize the average size of the spherulites.

Scattering from discs. The scattering from thin aniso-

tropic discs of radius R oriented normally to the incident beam can be represented by:[23]

$$I_{Vv} = K^2v^2(2/w^2)^2\{(\alpha_t - \alpha_s)[wJ_1(w) + J_o(w) - 1] + (\alpha_r - \alpha_s')[1 - J_o(w)] + (\alpha_t - \alpha_r)[2 - 2J_o(w) - wJ_1(w)]\cos^2\mu\}^2 \quad \text{(III-7)}$$

and $$I_{Hv} = K^2v^2(2/w^2)^2\{(\alpha_t - \alpha_r)[2 - 2J_o(w) - wJ_1(w)]\sin\mu\cos\mu\}^2 \quad \text{(III-8)}$$

where $w = kR\sin\theta = 2\pi/\lambda\, R\sin\theta$ and J_o and J_1 are Bessel functions of the first kind with order zero and one respectively.

The above equations apply to the case where the principle polarizability of the spherulites are at 0^o or 90^o to the spherulite radius and predict Vv scattering patterns having maximum intensity in the polarization direction and Hv scatpatterns with maximum intensity at 45^o to the polarization direction.

A more general theory has been developed for the scattering from two-dimensional spherulites,[24] where the optic axis lies in the plane of the disc but tilted at an angle β to the radius. In this case the intensity of the scattered beam is given by:

$$I_{Vv} = Kc^2E_o^2\cos^2\rho_1A^2(2/w^2)^2\{\alpha_1[1 - J_o(w)] + \alpha_2[wJ_1(w) - (1 - J_o(w))] - (\alpha_1 - \alpha_2)\cos^2\gamma[2(1 - J_o(w)) - wJ_1(w)]\}^2 \quad \text{(III-9)}$$

and $$I_{Hv} = Kc^2E_o^2(\alpha_1 - \alpha_2)^2A^2\cos^2\rho_2\sin^2 2\gamma\,(1/w^2)^2\{2[1 - J_o(w)] - wJ_1(w)\} \quad \text{(III-10)}$$

where $\xi = \mu + \beta$ and $w = (2\pi/\lambda)R\sin\theta$ and $A = \pi R^2$ (the area of the disc) and

$$\cos\rho_1 = \frac{\cos\theta}{\left[\cos^2\theta + \sin^2\theta\cos^2\mu\right]^{\frac{1}{2}}} \qquad \text{(III-11)}$$

$$\cos\rho_2 = \frac{\cos\theta}{\left[\cos^2\theta + \sin^2\theta\sin^2\mu\right]^{\frac{1}{2}}} \qquad \text{(III-12)}$$

These equations are similar to the equations given as equations III-7 and 8, except that μ is replaced by $\xi = \mu + \beta$. Thus the light scattering pattern will be rotated through the azimuthal angle by the amount β. The variation of such spherulitic patterns with θ exhibits a maximum corresponding to $w = (2\pi/\lambda)R\sin\theta = 3.9$. (III-13)

B. Statistical Approach

For systems where it is not possible to characterize the scattering in terms of a discrete model, the statistical approach is most useful. This approach employs the correlation function technique, where the probability of correlation of the average refractive index, anisotropy, and the optic axis orientation between two scattering elements separated by a given distance is described.

This method permits the separation of contributions to scattering arising from average refractive index, anisotropy, and orientation fluctuations in that the latter two types contribute to Hv scattering, whereas, all three contribute to Vv scattering. The method is particularly useful to study

the internal heterogeneity of the spherulites. The scattering resulting from internal heterogeneity usually occurs at larger scattering angles.

The statistical approach starts with the following equation:

$$I = \iint A_i A_j \cos k(\vec{r}_{ij} \cdot \vec{s})\, dr_i\, dr_j \qquad \text{(III-14)}$$

where A_i and A_j are the scattering amplitudes from the ith and jth elements and $\vec{r}_{ij}$ is the vector separation. $\vec{s} = \vec{s}_o - \vec{s}_1$, where $\vec{s}_o$ and $\vec{s}_1$ are unit vectors along the incident and scattered rays.

Scattering may arise as a consequence of fluctuations in the average refractive index (density) of the medium, the local anisotropic and the orientation of the optic axis of the anisotropic regions. Scattering from density fluctuations may be statistically described in terms of correlation function. For the Rayleigh-Gans case, the Debye and Bueche theory[25] leads to the following equation for the scattering intensity:

$$I = K \langle (\Delta\alpha)^2 \rangle_{av} \int_{r=0}^{\infty} \gamma(r)(\sin(hr)/hr) r^2\, dr \qquad \text{(III-15)}$$

where $h = (4\pi/\lambda)\sin(\theta/2)$, λ is the wavelength of the light in the medium ($\lambda = \lambda_o/n$; λ_o being the wavelength in vacuum and n the refractive index of the medium); θ is the scattering angle, $(\Delta\alpha)$ is the difference between the local polarizability of a volume element and the mean polarizability of the medium called the polarizability fluctuation. $\langle (\Delta\alpha)^2 \rangle_{av}$ is the mean square value of the polarizability fluctuations,

$\gamma(r)$ is the density correlation function defined by:

$$\gamma(r) = \frac{\langle (\Delta\alpha)_i (\Delta\alpha)_j \rangle_r}{\langle (\Delta\alpha')^2 \rangle_{av}} \qquad \text{(III-16)}$$

where $(\Delta\alpha)_i$ and $(\Delta\alpha)_j$ are the polarizability fluctuations of the ith and jth volume elements and the symbol $\langle\ \rangle_r$ designates an average over all pairs of volume elements separated by a distance r. The density correlation function, $\gamma(r)$, decreases from unity at $r = 0$ to zero at $r = \infty$. $\gamma(r)$ can be obtained from a Fourier inversion of the dependence of the scattered intensity upon θ. The Debye and Bueche theory of density fluctuations has been generalized to take into account both fluctuations in density and in orientation.

Random orientation fluctuations. This theory has been developed by Stein and Wilson[26] and involves the assumption of "random orientation fluctuations", i.e., it is assumed that the correlation in orientation depends only upon the separation of the scattering elements and does not depend upon the orientation of the optic axis with respect to the line interconnecting the two volume elements. The results of the theory are given in the following equations:

$$I_{Vv} = K\left\{(\Delta\alpha)^2_{av}\int_0^\infty \gamma(r)\,\frac{\sin(hr)}{hr}\,r^2\,dr \right. \qquad \text{(III-17)}$$
$$\left. + 4/45\,\langle\delta^2\rangle_{av}\int_0^\infty f(r)\left[1 + \frac{\langle\Delta^2\rangle_{av}}{\langle\delta^2\rangle_{av}}\,\psi(r)\right]\frac{\sin(hr)}{hr}\,r^2 dr\right.$$

and $$I_{Hv} = 1/15\ K\langle\delta^2\rangle_{av}\int_0^\infty f(r)\left[1 + \frac{\langle\Delta^2\rangle_{av}}{\langle\delta\rangle_{av}}\Psi(r)\right]\frac{\sin(hr)}{hr}\ r^2dr$$

where δ is the anisotropy of a volume element defined by

$$\delta = \alpha_1 - \alpha_2 \qquad \text{(III-19)}$$

where α_1 and α_2 are the longitudinal and transverse polarizability of the volume element and Δ is the fluctuation in the anisotropy;

$$\Delta_i = \delta_i - \langle\delta\rangle_{av} \qquad \text{(III-20)}$$

f(r) is the orientation correlation function defined by:

$$f(r) = \frac{3\langle\cos^2\theta_{ij}\rangle_r - 1}{2} \qquad \text{(III-21)}$$

where θ_{ij} is the angle between the axes of the principle polarizability of the ith and jth elements. f(r) is zero where there is no correlation in orientation and it is equal to unity if the optic axes are parallel. $\Psi(r)$ is a correlation function for fluctuation in the magnitude of the anisotropy defined by:

$$\Psi(r) = \frac{\langle(\Delta)_i(\Delta)_j\rangle_r}{\langle\Delta^2\rangle_{av}} \qquad \text{(III-22)}$$

If all the volume elements have the same anisotropy, $\langle\Delta^2\rangle_{av} = 0$, and equation III-18 reduces to

$$I_{Hv} = 1/15\ K\langle\delta^2\rangle_{av}\int_0^\infty f(r)\ \frac{\sin(hr)}{hr}\ r^2dr \qquad \text{(III-23)}$$

f(r) can be determined by Fourier inversion of I_{Hv}. It may also be represented by either an exponential function

$$f(r) = \exp(- r/a_1) \qquad \text{(III-24)}$$

or a Gaussian function

$$f(r) = \exp(- r^2/a_2^2) \qquad \text{(III-25)}$$

where a is a persistance distance of orientation correlations. The subscripts 1 and 2 indicate different values of a. If equation III-24 is substituted into equation III-23, the integration yields

$$(I_{Hv})^{-\frac{1}{2}} = c(1 + a_1^2 h^2) \qquad \text{(III-26)}$$

where $c = (2/15\ K\langle\delta^2\rangle_{av} a_1^3)^{-\frac{1}{2}}$ and $K = 64\pi^5/\lambda_o^4$. A plot of $I_{Hv}^{-\frac{1}{2}}$ against h^2 should give a straight line with the ratio of the slope to the intercept being equal to a_1^2. The intercept is equal to c, which is proportional to the anisotropy. If equation III-25 is used in equation III-23, the integration yields

$$I_{Hv} = A a_2^6 \exp(-a_2^2 h^2/2) \qquad \text{(III-27)}$$

A plot of ln I_{Hv} against h^2 gives a straight line with a negative slope equal to $a_2^2/2$.

$\gamma(r)$ may also be determined since

$$K\langle(\Delta\alpha)^2\rangle \int \gamma(r) \frac{\sin(hr)}{hr} r^2 dr = I_{Vv} - 4/3\ I_{Hv} \qquad \text{(III-28)}$$

Therefore, for isotropic scattering elements, $\langle\delta^2\rangle = 0$, and $I_{Hv} = 0$, and equation III-17 reduces to equation III-15. If all the scattering arises from anisotropy fluctuations so that $\langle(\Delta\alpha)^2\rangle_{av} / \langle\delta^2\rangle_{av}$ is very small, then I_{Hv} will approach its maximum value of $3/4\ I_{Vv}$.

The "random orientation fluctuation" theory predicts that the scattering is cylindrically symmetrical about the incident

beam at small θ and it is independent of the angle of rotation of the polarizer or analyzer with respect to the scattering plane, so long as they are rotated together. However, it is dependent upon the angle of the polarization direction of the polarizer and the analyzer with respect to each other. If the polarizer and analyzer are simultaneously rotated about their normals by an angle, Ψ, keeping them parallel, $I_{\parallel}$, or keeping them perpendicular, I_{+}, there will be no variation in the scattering intensity with Ψ at small scattering angles, θ, for samples having no macroscopic orientation.

According to the Stein-Wilson theory[26] the relationship of $I_{\parallel}$ and I_{+} and the polarization angles are

$$I_{\parallel} \text{ when } \Psi_a = \Psi_p$$

$$\text{and } I_{+} \text{ when } \Psi_a = \Psi_p + 90$$

where Ψ_a and Ψ_p are the angle of the analyzer and polarizer from the vertical direction respectively. Recently, Prins and co-workers[21] have defined $I_{\parallel}$ and I_{+} in a different way. $I_{\parallel}$ is the component parallel to the plane through the polarization direction of the incident beam and the scattering direction, $\vec{s}'$; I_{+} is the component perpendicular to this plane. With this definition for $I_{\parallel}$, Ψ_a is related to Ψ_p by

$$\tan \Psi_a = \cos\theta \tan \Psi_p$$

while for I_{+},

$$\tan \Psi_a = -\cot \Psi_p / \cos\theta$$

Therefore the Stein-Wilson definition of $I_{\parallel}$ and I_{+} is an approximation of the Prins definition and it is only valid at

small θ.

Non-random orientation fluctuations. The reason for the independence of the scattered intensity of the angle Ψ at low scattering angles for the random orientation fluctuation case is a consequence of the shape of the correlated region. If the probability of the correlation in orientation of optic axes of two scattering elements is independent of the angle between the vector connecting them and the optic axis vector, then the average dimension of the correlated region will be independent of the direction in which this is measured relative to the optic axis direction.

If the orientation fluctuations are non-random, the probability of optic axes being parallel depends upon the angle between the optic axes and the vector connection them. A general theory for such systems has been developed.[27] The theory includes correlation functions which characterize the way in which the angular dependence of orientation correlation varies with the separation of the scattering elements. The theory predicts a great variation of the scattered intensity with Ψ. The mathematical formulation of the theory is quite complex and it has been worked out for special cases such as discs. The results were presented in the first section of this chapter.

C H A P T E R I V

RESULTS AND DISCUSSION

A. Solid State

Previous work[13,14] on cholesteryl myristate in the solid state has demonstrated that the photographic light scattering patterns result primarily from the existance of anisotropic regions having correlated orientation with dimensions comparable with the wavelength of light. The following section deals with quantitative measurements of the size and the arrangement of the correlated regions, using the photometric light scattering method.

In order to apply a quantitative light scattering theory, it was essential to prepare samples with fifty percent transmission or higher. For this purpose several samples were prepared in the manner described earlier. Table IVA-1 gives the thickness and the transmission of the samples prepared. It is seen that only the last two samples have satisfactory transmission for use. Microscopic observations on these samples, when viewed between crossed polars, show a morphology consisting of highly birefringent platelets of irregular shape with wrinkled appearance similar to that observed by Barrall et al.[28]

The variation in $I_{\parallel}(Vv)$ and $I_{+}(Hv)$ intensity with scattering angle for J-9 and J-8 samples was measured. The data were corrected for reflection, refraction and secondary

TABLE IVA-1. RELATIONSHIP BETWEEN PERCENT TRANSMISSION AND SAMPLE THICKNESS OF CHOLESTERYL MYRISTATE IN THE SOLID STATE

CODE	THICKNESS mils	% TRANSMISSION
J-4	1.5	21
J-5	1.2	29
J-6	0.9	39
J-7	0.8	46
J-8	0.6	54
J-9	0.4	67

scattering (see Appendix I). Figures IVA-1 and IVA-2 give the results of J-9. These curves indicate that there is a very rapid drop of intensity with angle. This is characteristic of large scatterers (compared to the wavelength of light). I_+ and $I_{||}$ are comparable in intensity indicating that essentially all of the scattering arises from fluctuations in orientation.

The dependence of the scattered intensity on polarization direction was measured. This was done by rotating the polarizer and analyzer simultaneously about their normals through an angle, Ψ , keeping them parallel, $I_{||}$, or keeping them perpendicular, I_+. The variation of I_+ and $I_{||}$ with Ψ for J-9 sample at several scattering angles is given in Figures IVA-3, IVA-4, and IVA-5. The relative intensities are normalized to unity at $\Psi = 0$. It is evident from these figures that there is a slight variation of intensity with Ψ, at least at small scattering angles, indicating non-randomness. The same results were found for J-8 sample as shown in Figures IVA-6 and IVA-7.

I_{Hv} is greater than the maximum value of 3/4 I_{Vv} predicted by random orientation correlation theory. The discrepancy may in part be due to the non-randomness and to secondary scattering since the percent transmission is not very high. It is found that the ratio of I_{Hv} to I_{Vv} for both samples fluctuates between 1.0 and 0.71 at different scattering angles. When comparing the ratio of I_{Hv} to I_{Vv} at each

angle, it is found that J-8, the sample with lower percent transmission has higher values than J-9, the sample with higher percent transmission, indicating that the secondary scattering is the main cause of the discrepancy noted above. In order to improve the transmission, the sample held between cover slips was dipped into a beaker full of silicon oil of matching refractive index. The beaker in turn was placed in a dessicator and a vacuum was applied forcing the silicon oil to penetrate the sample and fill any microvoids which might be present. After several hours, the sample was taken out and the percent transmission was measured again. However, the percent transmission increased by only a few percent. Therefore, another method was tried, and silicon oil was introduced into the sample before it crystallized from the melt. Sample J-1 was prepared in this manner. The structure of this sample in the solid state shows birefringent spherulites exhibiting a maltese cross when viewed between cross polars, where the dark bands are parallel to the polarization directions, indicating that the optic axes are either parallel or perpendicular to the spherulite radii. Such maltese crosses were not observed in samples J-8 or J-9. The size of the spherulites are rather large. The radius was measured photometrically by scanning the scattered intensity through scattering angle θ under the condition that Ψ_1 is 45° and Ψ_2 is -45°. The maximum intensity occurs at $\theta = 10'$, which corresponds to a radius of 150μ.

The dependence of the scattered intensity on the polarization direction was also measured at different values of θ. Figure IVA-8 gives the result when $\theta = 5^{\circ}$. Two facts are evident from this figure. The variation of intensity with Ψ is greater than the previous two samples, namely J-8 and J-9. I_{+} exhibits a maximum at $\Psi = 45^{\circ}$ and a minimum at $\Psi = 90^{\circ}$, while $I_{||}$ shows a maximum at $\Psi = 90^{\circ}$ indicating that the optic axes are oriented at 90° to the radius. These results were also obtained at 10° and 15°. The above data indicates that the silicon oil affects the morphology of the solid state.

The silicon oil was also found to affect the transitions as observed by differential scanning calorimetry. When a pure sample of cholesteryl myristate is heated from room temperature to above the isotropic melting point, one observes three peaks on the DSC trace, corresponding to the three transitions, namely solid --> smectic --> cholesteric --> isotropic melt. When mixing the same amount of cholesteryl myristate with a drop of silicon oil, the two peaks corresponding to the last two transitions disappear both on heating and cooling. These results were found to be independent of the amount of cholesteryl myristate, indicating that the silicon oil interacts with the cholesteryl mytistate in the smectic and the cholesteric mesophases. Therefore, it was decided not to use any immersion oil in the studies.

It was shown above that essentially all of the scattered intensity arises from orientation correlations. Samples J-8 and J-9 give very small Ψ-deperdence. Therefore the random orientation correlation theory can be applied to the I_{Hv} scattered intensity to calculate the correlation distance and the average anisotropy. Equation III-26, given in chapter III, was applied. The equation assumes that the orientation correlation function is described by an exponential function. The results are given in Figures IVA-9 and IVA-10 for the J-8 and J-9 samples respectively. The plots are linear over a wide range of angles indicating that the exponential function is suitable. If assuming a Gaussian function (as was done in equation III-27) were more appropriate, the plot of ln I_{Hv} versus h^2 should be linear, which was not found to be so. Because the intensity was measured absolutely, one can calculate the average anisotropy, $\langle \delta^2 \rangle_{av}$, from the intercepts in Figures IVA-9 and IVA-10. The correlation distance, a, is calculated from the ratio of the slope to the intercept as explained in chapter III. The results are summarized in Table IVA-2. The values of a, correspond to the width of striation in the microscopic pictures.

TABLE IVA-2. CHARACTERISTIC VALUES OBTAINED FROM LIGHT SCATTERING BY CHOLESTERYL MYRISTATE FILMS IN THE SOLID STATE (λ_o = 5460 A^o)

SAMPLE	TEMPERATURE ^oC	THICKNESS mils	a microns	$\langle \delta^2 \rangle^{\frac{1}{2}}$
J-9	25	0.4	1.03	1.24×10^{-5}
J-8	25	0.6	1.07	1.56×10^{-5}

B. Morphological Differences Occuring During Heating and Cooling Cycles

The morphological differences occuring during heating and cooling cycles were observed by performing the following experiments. The sample was heated to 90°C and held at this temperature for half an hour. The sample was then cooled very quickly to a temperature which lies in the temperature range of the cholesteric phase. Temperature equilibrium was achieved within 1 to 2 minutes. After waiting for some time, as indicated later, the sample was cooled again to a temperature corresponding to smectic phase and then to the solid state. After waiting for at least thirty minutes at 30°C, the sample was heated fast to the smectic, then to the cholesteric phase. Typical photomicrographs and light scattering pictures were taken for each mesophase.

Figure IVB-1 shows two photomicrographs for 1.5 mil thick sample at 80°C after thirteen and twenty minutes. It is seen that the growth started at one center which grows uniformally in the radial direction. It is important to notice that not all nuclei started at the same time. This can be seen from the small maltese cross on the picture on the right.

Figure IVB-2 shows the morphology obtained for both cooling from the isotropic melt and heating from the smectic phase. It is easily seen that the two morphologies are different. The picture on the right shows a maltese cross which

was not observed in the picture on the left which was taken on cooling from the melt. However, one can see the center of the growing objects very clearly.

The difference in morphology is also indicated by the Hv light scattering patterns shown in Figure IVB-3. On cooling, one obtains an Hv pattern with 90° orientation and a very bright spot in the center. On the other hand, the pattern obtained for the sample when heated from the smectic phase is an Hv pattern with 45° orientation. The Vv pattern and the interpretation of the light scattering pictures will be presented in later sections. At the present only morphological differences will be given.

Figure IVB-4 shows the morphology of the sample at 75°C (smectic phase) when cooled from 80°C and when heated from 60°C. It is seen that there is no difference in morphology between the two pictures and thus one can conclude that the smectic phase has the same morphology when cooled from the cholesteric phase and when heated from the solid state. It is worthwhile to indicate that the change in morphology in going from the cholesteric phase to the smectic phase or from the solid state to the smectic phase is very fast (almost instantaneous). It is also interesting to indicate a common feature for both pictures which is the circular arrays around a common center. In fact, when cooling from the cholesteric to the smectic phase, one can see a counter-clockwise motion of particles that produced the above patterns.

The light scattering patterns for the smectic phase at 75°C are shown in Figure IVB-5, where you can see the more or less circular Hv and Vv patterns.

The morphology in the solid state at 60°C is shown in Figure IVB-6 for cooling from 75°C and when heating to 60°C from 30°C. Here one can see that the morphology is different for the two cases. In fact, the morphology at 60°C for the one which was cooled from 75°C is exactly the same morphology as that of the smectic at 75°C. On the other hand, the morphology of the sample upon heating from 30°C is the same as that which is obtained at 30°C.

In order to make sure that the morphology at each of the mesophases is independent of the number of heating and cooling cycles, the above experiments were repeated three times in the same manner and the same morphology was observed each time. Also the same scattering patterns as those shown were observed.

The morphology obtained when heating the sample very fast from 30°C to 80°C is exactly the same as that obtained when heating from 75°C to 80°C. (See Figure IVB-2.)

When the sample was cooled very fast from the isotropic melt to 75°C and to 60°C without stopping at the cholesteric phase, there was no growth of any kind during the time after temperature equilibrium was achieved. This time was at least half an hour.

Although the aforementioned morphological changes were described for the 1.5 mil sample thickness, the same observations

were found for the other sample thicknesses also. The same experiments were done for 0.5, 1.0, and 3.0 mil samples. The 3.0 mil sample and thicker samples, which will be discussed below, exhibit an intermediate state in the cholesteric phase before the appearance of the circular objects. This state was observed in the following way: when the sample was cooled quickly from the isotropic melt to the cholesteric phase and immediately after the sample reached temperature equilibrium, the field of view became a pale blue color. This color lasted for a few seconds and sometimes for a few minutes depending on the temperature when the observation was made. The color lasted for longer periods of time at the higher temperature range of the cholesteric phase. The blue color faded away as the circular objects started to appear and grow. The Hv light scattering pattern corresponding to the blue state is a diffuse circular pattern. The blue color is more intense in thicker samples. It was observed in a 6 mil and a 12 mil sample.

Another point which should be mentioned here is that the above observations concerning the morphological differences in each of the mesophases were found in the whole temperature range of the smectic phase (between 79.7°C and 73.6°C). However, in the cholesteric phase there seems to be differing morphologies in the lower temperature range and the higher temperature range. This point will be discussed in the next section.

C. The Isotropic--Cholesteric Phase Transition

The morphology of the isotropic--cholesteric phase transition was studied as a function of temperature and sample thickness. The results will be presented in the order of sample thickness. Both the microscopic pictures and the photographic light scattering patterns will be shown together where it is possible.

The experimental procedure was as follows: The sample was heated to 90°C and held at that temperature for half an hour. The sample was then cooled very quickly to the desired temperature. After temperature equilibrium has been achieved, photomicrographs and light scattering patterns were taken at sucessive time intervals.

0.5 Mil sample thickness. Figure IVC-1 shows the microscopic pictures at 80°C at different time intervals. Here one can see well defined maltese crosses where the dark bands are parallel to the polarization directions, indication a spherulitic structure. The spherulites grow radially in a uniform manner except when they impinge on each other.

The corresponding Hv light scattering patterns are given in Figure IVC-1b. The Hv pattern taken fifteen minutes after reaching 80°C consists of a four-leaf clover which is typical for spherulites of high polymers. This pattern becomes smaller and more intense with time and another diffuse pattern

surrounding the initial one appears which becomes more intense at longer times. This outer pattern, however, has 90° orientation, i.e., along the polarization direction, with a definite minimum in intensity along the zero and the ninety degree directions. The interpretation of the light scattering patterns and comparison of spherulite sizes as obtained by microscopy and light scattering will be presented later in this section.

1.5 Mil sample thickness. Figure IVC-2 shows the growing centers at sucessive times at 79.8°C. It is noted that not all of the growing centers start at the same time. The internal morphology of the radially growing center becomes more and more pronounced with time. This type of growth is independent of sample position as shown in Figure IVC-3 for the same sample at the same temperature. Figure IVC-4 shows the growth with time at 80°C. Two things are apparent from these photomicrographs: first, not all of the nuclei appear at the same time and secondly, one can see a very clear maltese cross which with time becomes more like a circular pattern with detailed internal morphology. The corresponding Hv light scattering patterns are given in Figure IVC-5. Each of the patterns is composed of two patterns, at least at short time intervals. The center pattern is an Hv pattern with 45° orientation, while the outer one is at 90° orientation. At longer times, the center pattern becomes more intense, but it also becomes more circular and the outer pattern becomes more intense, but with a ninety degree orientation. It is also noted that there

is a definite minimum in the intensity along the zero or ninety degree direction.

Figure IVC-6 shows the growth at different times at 80.5°C. The growth, as seen in these photomicrographs, is in a uniform radial direction. The internal structure of the growing centers becomes clearer with time. The growth as a function of time was also studied at 81°C as shown in Figure IVC-7.

Figures IVC-8 and IVC-9 show the variation of growth with time at 81.5°C and 82°C respectively. It is worthwhile to indicate here that while at these two temperatures, the morphology is very similar, it differs from those observed at lower temperatures. The internal structure of the growing centers at 81.5°C and 82°C appears to be elongated particles, while at lower temperatures the internal structure is more like small grains. Also, at higher temperatures, there is no sharp boundary, but at lower temperatures the boundaries are very sharp.

The difference in the internal morphology of the spherulites at the low temperature and at the high temperature range of the cholesteric phase is more clearly demonstrated in the photomicrographs of Figure IVC-10, which have a higher magnification. The light scattering patterns bear out the differences also. Figure IVC-11 gives the Hv and Vv patterns at temperatures between 79.8°C and 81°C and Figure IVC-12 shows the light scattering patterns at 82°C. It should be

pointed out that the initial Hv pattern at 82°C is the typical 45° oriented Hv pattern obtained at lower temperatures. It is seen from Figures IVC-11 and IVC-12, that the Hv pattern for the whole temperature range is composed of two parts, the central pattern with 45° orientation and the outer pattern with 90° orientation. The corresponding Vv pattern is composed of the central part which is very intense while the outer part has a 45° orientation. One can also see that the Hv pattern for the lower temperature range has a definite minimum in intensity along the zero and the ninety degree direction, but in the higher temperature range, no such minimum is detected. This is most clearly shown in Figure IVC-12 at 82°C. Figure IVC-12 should be compared with Figure IVC-10, where the internal structure of the growing object is more rod shaped.

3 Mil sample thickness. Figure IVC-13 shows the development of growth with time at 81°C. The growing regions started as small maltese crosses and them grew in a uniform radial direction. The growth was also followed by taking Hv light scattering pictures. These are given in Figure IVC-14. At short times one can see a four-leaf clover pattern at the center with 45° orientation, surrounded by a weak four-leaf clover pattern with a 90° orientation. As time progresses, the center pattern becomes smaller while the outer becomes stronger, but loses its symmetry. After a long period of time, the pattern becomes a circular pattern. The same

observations are true for other temperatures in the cholesteric phase as shown in Figure IVC-15 and Figure IVC-16 at 82°C.

6 Mil sample thickness. The growth or crystallization in the cholesteric phase was followed as a function of time and temperature. The following observations were made in the temperature range between 80°C and 82°C. Initially as the temperature reaches equilibrium, the field of view becomes blue. The blue color lasts for a short time. Many birefringent particles appear as the blue color fades away. Larger and more intense particles appear later, which continue to grow and the whole field of view will be covered with these. The development of their growth is seen in Figure IVC-17. (The temperature is 81.5°C.) The corresponding Hv light scattering patterns are given in Figure IVC-18. These patterns show that up to 20 minutes the pattern has circular symmetry. However, at 25 minutes, a four-leaf clover pattern with 45° orientation appears at the center, which as time passes becomes smaller and more intense.

Cholesteryl myristate in the cholesteric phase is known to exhibit a blue color just below the isotropic--cholesteric transition temperature.[7] It has been reported that the color disappears as the temperature is lowered and a new texture appears. Friedel[5] and Gray[7] were concerned with textural changes in the cholesteric phase at different temperatures. The present results are different from previous work in that

the texture changes at constant temperature were followed as a function of time.

Interpretation of the light scattering patterns. The results seen for thin samples, that is, those which are less than three mils in thickness, indicate that the growth in the cholesteric phase is in a uniform radial direction. At the onset of "crystallization", one can see well defined maltese crosses in the photomicrographs. The corresponding Hv light scattering patterns show well defined four-leaf clover patterns with 45^{o} orientation. This kind of growth is characteristic of a spherulitic growth. At longer time intervals of "crystallization", it was shown that another four-leaf clover Hv pattern develops but with 90^{o} orientation. It is possible to calculate the diameter of the spherulites which give rise to these two patterns of Hv light scattering. The calculated values can be compared directly with the microscopic pictures. The spherulite size can be calculated using equation III-13 for two-dimensional spherulites. The results of the calculation and the measured values can be found in Table IVC-1. The agreement between the two methods is very good. Therefore, one can conclude that the center Hv pattern arises from scattering due to the spherulites in which the optic axes of the molecules are oriented at zero or ninety degrees with respect to the radius of the spherulite. It should be noted here that the diameters of these spherulites are large and in fact reach the order of magnitude of three

TABLE IVC-1. SPHERULITE SIZE AS OBTAINED FROM LIGHT SCATTERING AND FROM MICROSCOPY.

SAMPLE THICKNESS MILS	TEMPERATURE °C	TIME OF CRYSTALL. MIN.	FIGURE	DIAMETER, μ L.S	DIAMETER, μ MICROSC.
0.5	80	15	IVC-1, IVC-1b	76	80
1.5	80	15	IVC-4, IVC-5	400	450
3.0	82	23	IVC-15, IVC-16	200	200

or four times the thickness of the sample. Therefore, they must be two dimensional spherulites, i.e., discs.

The outer Hv pattern with ninety degree orientation, on the other hand, is a result of the scattering from the microstructure of the spherulite. For example, from Figure IVC-1b, the calculated diameter from light scattering at 80°C is eighty microns while the size of the "crystallites" inside the sperulite is on an order of 10 microns for the 0.5 mil sample, in Figure IVC-1. This conclusion is also true for the 1.5 mil sample. The calculated diameter at 80°C from light scattering is about 25 microns and the observed size of the "crystallites" is also about 25 microns. (See Figures IVC-3 and IVC-5.) For the 3 mil sample, the outer pattern is circular and it is not possible to calculate sizes from the light scattering pattern. However, the size obtained by microscopy is about 16 microns at 80°C. There are several reasons that might account for the circular symmetry of the outer Hv pattern. In thicker samples, the secondary scattering is strong and as a result circular symmetry is usually observed. The other possibility is the effect of optical activity of the cholesteric phase on the light scattering patterns. It was shown by Picot and Stein[29] that the optical activity has the effect of making the Hv pattern more circular with increasing sample thickness.

The outer Hv light scattering pattern with 90° orientation

observed when cooling the sample from the isotropic melt to the cholestcric phase in thin samples deserves more attention. This kind of pattern has been observed in cholesteryl propionate in the cholesteric phase.[14] However, it is not mentioned whether this pattern for the propionate was obtained when cooling from the melt or when heating from the solid state. Such patterns have also been observed in polytetrafluoroethylene[30] and in polyethylene terephthalate.[31] The patterns could be explained if the optic axes were tilted at approximately 45^{o} from the direction of the radius of the spherulite according to the theories developed in chapter III. When heating the sample either from the solid or from the smectic phase to the cholesteric, an Hv pattern with 45^{o} orientation is always obtained in thin samples. The intensity of the scattered light decreases monatonically along the $\pm 45^{o}$ direction. This behavior has been explained in terms of disc-like non-random correlation.[14]

In the present study concerning cholesteryl myristate, the outer Hv pattern exhibits a definite maximum in thc intensity along the zero and the ninety degrees direction as it was shown in Figurc IVC-5. The position of this maximum does not change with time indicating that the size of the particles giving rise to this scattering remains constant with time and only their number increases. This fact can be seen by investigating the photomicrographs in Figure IVC-4. The same conclusion is true for the 0.5 mil sample as shown

in Figure IVC-1b. The presence of a maximum in the outer Hv pattern indicates that the particles are spherulites in which the optic axis is oriented at 45^{o} to the radius of the spherulite. However, at higher temperatures, such as $82^{o}C$, the intensity decreases monatonically along the zero and ninety degree directions, indicating that the scattering results from rod type aggregates with the optic axis oriented at 45^{o} to the long axis of the rod. This is in agreement with the photomicrographs shown in Figure IVC-10. The Vv pattern always has the $\pm 45^{o}$ orientation as shown in Figure IVC-11 and IVC-12. Therefore, one can conclude that at temperatures below $81^{o}C$, the internal structure of the big spherulites is spherulites in which their optic axes are at 45^{o} to the radius, while the overall direction of the optic axis of the big spherulites is at zero or ninety degrees to the radius. At higher temperatures, the internal structure of the spherulites consists of rods with the optic axes of the molecules at 45^{o} to the long axis of the rod.

As it was shown above, the Hv light scattering pattern in the smectic phase, irrespective of sample thickness, is always circularly symmetrical. This type of pattern, obtained both by cooling from the cholesteric phase or heating from the solid state. This kind of scattering arises from random orientation fluctuation.

The blue phase in the cholesteric phase gives a diffuse circular Hv pattern, which results from scattering of small

particles randomly distributed and not resolvable by the optical microscope. Measurements of the size is important and this will be presented in section F of this chapter.

D. Kinetics of Spherulite Formation

It was shown in the previous section that cholesteryl myristate exhibits a transition from an isotropic melt to the cholesteric mesophase upon cooling. This transition was shown to occur in two steps. The first step is a rapid transformation to a turbid blue phase, while the second is a much slower transition to a macroscopically ordered spherulitic state. Therefore, it is important to study the kinetics of the spherulite formation.

The experimental procedure is the same as was described earlier, where the sample was heated to 90°C, well above the cholesteric isotropic transition. The sample was kept at that temperature for at least half an hour, then quickly cooled to the desired temperature under isothermal conditions. Photomicrographs were taken at different time intervals. The radius and the number of spherulites were then measured. Growth and nucleation rates were determined as functions of temperature and sample thickness.

Growth rate. The variation of spherulite radii with time for 1.5 mil sample at various temperatures is given in Figure IVD-1 and is seen to be linear. This indicates that the process is diffusion independent, since if it were not, the radius should depend upon the square root of time. The spherulite growth rate, G, is obtained from the slopes of the plots of spherulite radius versus time. Table IVD-1 gives the growth

TABLE IVD-1. GROWTH RATES AT VARIOUS TEMPERATURES FOR 1.5 MIL CHOLESTERYL MYRISTATE SAMPLE

$T^{\circ}C$	$\Delta T^{\circ}C$	G(μ/min.)
79.8	4.2	32.0
80.0	4.0	29.4
80.5	3.5	17.7
81.0	3.0	8.0
81.5	2.5	10.0
82.0	2.0	11.8

rate at different temperatures, along with the degree of supercooling if the isotropic--cholesteric temperature is taken to be 84.0°C. It is worth noticing that the growth rate at 81.5°C and 82°C is higher than that at 81°C. This result is reproducible since the growth rate at 82°C was measured on two different days. This anomaly might be explained by comparing the morphology or texture of the spherulites obtained at 81.5°C and at 82°C with the texture of the spherulites at the lower temperature as was shown previously in Figures IVC-4 through IVC-12. It was concluded from these photomicrographs and the light scattering patterns that the internal morphology of the spherulites at 81.5°C and 82°C consists of rod shaped aggregates while at lower temperatures the internal structure of the spherulites is spherulitic.

Similar kinetic studies were carried out on different sample thicknesses. Figures IVD-2 and IVD-3 show the dependence of the spherulite radius on time at various temperatures for 1 mil and 3 mil thick samples respectively. The growth is independent of diffusion for all of these cases as indicated by the linearity of the plots. The growth rates obtained and the degrees of supercooling are given in Table IVD-2. The effect of sample thicknesses on the growth rate is given in Figure IVD-4. The growth rate at any temperature is independent of sample thickness between 1.5 and 3.0 mil.

In order to analyze the temperature dependence of the growth rate, it is instructive to consider briefly the growth

TABLE IVD-2. GROWTH RATES AT VARIOUS TEMPERATURES FOR 1.0 AND 3.0 MIL CHOLESTERYL MYRISTATE SAMPLE

$T^{o}C$	$\Delta T^{o}C$	$G(\mu/min.)$
1.0 MIL SAMPLE		
79.8	4.2	37
80.0	4.0	23
80.5	3.5	9
81.0	3.0	3.6
3.0 MIL SAMPLE		
79.8	4.2	30
80.0	4.0	27
80.5	3.5	19
81.0	3.0	12

rate theory. When the linear growth rate of spherulites is characterized by a negative temperature coefficient, the conclusion is usually made that the growth of the spherulites is controlled by a secondary nucleation process. In other words, the spherulites grow when new crystallites are formed on the tips of the preexisting spherulites generated by the primary process. Therefore, a distinction must be made between the growth of a crystallite generated by the primary nucleation act and the evolution of a spherulite as new crystallites are formed.

The growth rate, G, for spherulitic growth which is nucleation controlled is given by

$$G = G_o \exp\left(- \frac{\Delta E_D^* + \Delta F^*}{kT} \right) \qquad \text{(IV-1)}$$

where G_o is a constant and ΔE_D^* is the activation energy for transport. ΔF^* is the critical free energy for nucleation, k Is the Boltzman constant and T is the temperature. The assumptions involved in equation IV-1 are that the deposition of a new layer of crystalline material to an already completed crystal face is determined by the rate of appearance of small crystals upon that face, and once a nucleus is formed, the entire face becomes rapidly covered up with a new layer of crystalline material.

When the nucleation is two dimensional, ΔF^* is[32,33,34]

$$\Delta F^* = \frac{4 b_o (\sigma_1 \sigma_2)_G}{\Delta f_u} \qquad \text{(IV-2)}$$

and for cylindrical three-dimensional nuclei

$$\Delta F^* = \frac{8\pi \sigma_2^2 \sigma_1}{(\Delta f_u)^2} \qquad \text{(IV-3)}$$

where Δf_u is the free energy of fusion per unit volume of the crystal, σ_1 and σ_2 are the lateral interfacial energy and excess interfacial free energy per unit area, respectively; and b_o is a fixed lattice spacing of the crystal. The subscript G refers to the growth process.

It is noted that ΔF^* is directly proportional to the product of the surface free energies, σ_1 and σ_2, but inversely proportional to the thermodynamic driving force, Δf_u. Δf_u is related to the heat of fusion per unit volume, Δh_f, by the following relation:

$$\Delta f_u = \frac{\Delta h_f (T_T - T)}{T_T} = \frac{\Delta h_f (\Delta T)}{T_T} \qquad \text{(IV-4)}$$

where T_T is the transition temperature and ΔT is the degree of supercooling.

Substituting the expressions for ΔF^* given in equations IV-2 and IV-3 for the two and three-dimensional nucleus into equation IV-1, the following equation is obtained for two-dimensional growth:

$$G = G_o \exp\left(\frac{-\Delta E_D^*}{kT}\right) \exp\left(\frac{-4b_o \sigma_1 \sigma_2 T_T}{\Delta h_f (\Delta T) kT}\right) \qquad \text{(IV-5)}$$

and for three-dimensional growth:

$$G = G_o \exp\left(\frac{-\Delta E_D^*}{kT}\right) \exp\left(\frac{-8\pi \sigma_2^2 \sigma_1 T_T^2}{(\Delta h_f)^2 kT (\Delta T)^2}\right) \qquad \text{(IV-6)}$$

Therefore, the analysis of the temperature coefficient of the growth rate should yield information in regard to the secondary nucleation act, thus aiding in elucidating details of the growth mechanism.

Equations IV-5 and IV-6 predict that a plot of ln G versus $T_T/T\Delta T$ or ln G versus $T_T^2/T(\Delta T)^2$ should be linear and the slopes will be proportional to the product of the interfacial energies, $\sigma_1 \sigma_2$. Such plots were constructed from the growth data for cholesteryl myristate. The results are given in Figures IVD-5, IVD-6, and IVD-7 for samples with thicknesses of 1 mil, 1.5 mil, and 3 mil, respectively. It is seen that in the three figures, ln G versus $T_T/T\Delta T$ is linear while ln G versus $T_T^2/T(\Delta T)^2$ is not. One must then conclude that the growth is two-dimensional. The slope of the straight line for the two-dimensional case is equal to $4b_o \sigma_1 \sigma_2 / \Delta h_f k$ hence, $\sigma_1 \sigma_2$ can be calculated. Δh_f is equal to 0.41 cal./gm.[35] Assuming b_o is 10 A^o, the calculated $\sigma_1 \sigma_2$ are given in Table IVD-3, along with the range of the critical radius of the nuclei which was obtained from $r = 2(\sigma)_{av} / \Delta f$, where $\sigma_{av} = (\sigma_1 \sigma_2)^{\frac{1}{2}}$. It should be noted here that the choice of b_o = 10 A^o is an arbitrary choice. The value of b_o does not affect σ_{av} seriously since σ_{av} is proportional to $(b_o)^{\frac{1}{2}}$.

Nucleation rate. The number of nuclei per unit volume at several temperatures were measured as a function of time. The data are plotted in Figures IVD-8 and IVD-9 for 1 mil and

TABLE IVD-3. INTERFACIAL ENERGIES OBTAINED FROM GROWTH RATES OF CHOLESTERYL MYRISTATE SAMPLES.

SAMPLE THICKNESS mils	$(\sigma_1\sigma_2)_G$ $erg^2/cm.^4$	σ_{av} $erg/cm.^2$	RANGE OF r A^o
1.0	0.140	0.37	400—550
1.5	0.084	0.29	320—430
3.0	0.056	0.24	200—280

3 mil sample thicknesses respectively. It can be seen from both of these figures that the nuclei density increases steadily for an interval of time after which the number of nuclei levels off to a constant value. It should be emphasized that the leveling off occurs with only 50 to 75% transformation completed. In other words, the leveling off did not occur as a result of complete transformation.

The steady increase in the number of nuclei with time is indicative of sporadic nucleation. The nucleation rate, $\dot{N}$, can be obtained from the initial slopes. The resulting data are given in Table IVD-4, along with the nucleation density, $\bar{N}$, at the leveling off for samples of 1 mil and 3 mil thicknesses. Such behavior has also been observed in some polymeric systems.[36,37,38] The results suggest a sporadic heterogeneous nucleation with first power dependence of nucleation rate on time. The heterogeneous nucleation is the process of birth of small crystalline regions on or near surfaces such as the container walls or adventitious impurities such as the dust particles and it has zero order dependence on time. The homogeneous nucleation, on the other hand, is a result of random fluctuation of order in the melt and it depends on the first power of time. A more general discussion can be found in an article by Price.[39]

The rate of nucleation in condensed systems for either homogeneous or heterogeneous nucleation has been developed by Turnbull and Fisher.[40] The nucleation rate per unit

TABLE IVD-4. NUCLEATION RATE AT VARIOUS TEMPERATURES FOR 1.0 AND 3.0 MIL CHOLESTERYL MYRISTATE SAMPLE

$T^{o}C$	$\Delta T^{o}C$	$\dot{N}$ $1/\mu^3 \cdot min.$	$\bar{N}$ $1/\mu^3$
1.0 MIL SAMPLE			
79.8	4.2	333×10^{-9}	762×10^{-9}
80.0	4.0	260×10^{-9}	457×10^{-9}
80.5	3.5	29×10^{-9}	381×10^{-9}
81.0	3.0	7.6×10^{-9}	375×10^{-9}
82.0	2.0	5.1×10^{-9}	165×10^{-9}
82.5	1.5	2.0×10^{-9}	100×10^{-9}
3.0 MIL SAMPLE			
79.8	4.2	24×10^{-9}	82×10^{-9}
80.0	4.0	16.5×10^{-9}	64×10^{-9}
80.5	3.5	4.5×10^{-9}	55×10^{-9}

volume and time is given by:

$$\dot{N} = N_o \exp\left(- \frac{\Delta E_D^* + \Delta F^*}{kT} \right) \qquad \text{(IV-7)}$$

where ΔE_D^* is the activation energy for transport across the liquid-nucleus interface, N_o is a constant and ΔF^* is the free energy of the formation of the nucleus of critical dimensions. This quantity depends on the geometry of the nucleus and on the kind of nucleation process, as will be seen below.

If the process is homogeneous, ΔF^* can be calculated for various nuclear geometries. For three-dimensional use, ΔF^* is given by the following equation:

$$\Delta F^* = \frac{A \sigma_1 \sigma_2^2 T_T^2}{\Delta h_u^2 (\Delta T)^2} = \frac{A(\sigma_1 \sigma_2^2)}{(\Delta f_u)^2} \qquad \text{(IV-8)}$$

where A is a geometric factor equal to 8π for cylindrical nuclei and equal to 32 for block shaped nuclei.

In the most general case of heterogeneous nucleation, one lets a crystal phase be in contact with a surface. Then define σ_s as the interfacial energy between the surface and the melt. Define σ_{os} as the interfacial energy between the surface and the crystal. ΔF^* for a two-dimensional process is given by:

$$F^* = \frac{4 b_o \sigma_1 \sigma_2}{\Delta f - \Delta\sigma / b_o} \qquad \text{(IV-9)}$$

where $\Delta\sigma = \sigma + \sigma_{os} - \sigma_s$ (IV-10)

Substituting equation IV-9 in equation IV-7, one obtains the following equation:

$$\dot{N} = N_o \exp\left(-\frac{\Delta E_D^*}{kT}\right) \exp\left(-\frac{4b_o \sigma_1 \sigma_2 T_T}{k \Delta h_f T \Delta T}\right)\left(\frac{1}{1 - \frac{\Delta \sigma T_T}{b_o \Delta T \Delta h_f}}\right) \qquad \text{(IV-11)}$$

In this case we see that a plot of $\ln \dot{N}$ versus $T_T/T\Delta T$ will not give a straight line. It can be seen from equation IV-11, that the maximum value of $\Delta\sigma T_T / b_o(\Delta T)(\Delta h_f)$ is unity. Therefore, it is possible to calculate an upper limit of $\Delta\sigma$ and it is found to be equal to 0.02 erg/cm.^{2} and 0.01 erg/cm.^{2} for 4.2°C and 3°C supercooling respectively. These values are extremely small and therefore to a first approximation the second exponential in equation IV-11 can be assumed to be unity. In this case then, ΔF^* for two and three-dimensional nucleation is given in equations IV-12 and IV-13 respectively.

$$\Delta F^* = 4b_o \sigma_1 \sigma_2 / \Delta f_u \qquad \text{(IV-12)}$$

$$\Delta F^* = 8\pi \sigma_2^2 \sigma_1 / \Delta f_u^2 \qquad \text{(IV-13)}$$

Equation IV-12 is for a block shaped nucleus with one fixed dimension. For disc-like nuclei where only the raduis increases, ΔF^* is given by

$$\Delta F^* = \pi b_o \sigma_2^2 / \Delta f_u \qquad \text{(IV-14)}$$

When the expressions for ΔF^* given in equations IV-12 and IV-13 are substituted into equation IV-7, the following equation is obtained for the two-dimensional nucleation:

$$\dot{N} = N_o \exp(-\frac{\Delta E_D^*}{kT}) \exp(\frac{-4b_o \sigma_1 \sigma_2 T_T}{\Delta h_f kT \Delta T}) \qquad \text{(IV-15)}$$

While for the three-dimensional cylindrical case:

$$\dot{N} = N_o \exp(\frac{-\Delta E_D^*}{kT}) \exp(\frac{-8\pi \sigma_2^2 \sigma_1 T_T^2}{(\Delta h_f)^2 kT(\Delta T)^2}) \qquad \text{(IV-16)}$$

It can be seen from the above equations, IV-15 and IV-16, that a plot of $\ln \dot{N}$ versus $T_T/T\Delta T$ or $T_T^2/T(\Delta T)^2$ for the two cases should yield a straight line. Such polts were constructed for cholesteryl myristate. This is given in Figures IVD-10 and IVD-11 for 1 mil and 3 mil samples respectively. It is seen that in both cases, while $\ln \dot{N}$ versus $T_T/T\Delta T$ is linear, $\ln \dot{N}$ versus $T_T^2/T(\Delta T)^2$ is not, indicating two-dimensional nucleation.

The calculated $\sigma_1 \sigma_2$ from the slopes of the linear plots in Figures IVD-10 and IVD-11 are given in Table IVD-5, along with $\sigma_{av} = (\sigma_1 \sigma_2)^{\frac{1}{2}}$ and the range of the critical nuclei radii.

Comparing the results of $(\sigma_1 \sigma_2)_N^{\cdot}$ in Table IVD-5 obtained from nucleation rates with $(\sigma_1 \sigma_2)_G$ in Table IVD-4 obtained from growth rates, we see that they are larger for the first case than in the latter case. This indicates that more energy is required to produce the primary nucleus and less energy to cause it to grow into a two-dimensional spherulite.

The values of interfacial energy obtained from nucleation or growth rate are very small. This indicates that very small forces hold the system together to produce a particular texture.

TABLE IVD-5. INTERFACIAL ENERGIES OBTAINED FROM NUCLEATION RATES OF CHOLESTERYL MYRISTATE SAMPLES.

SAMPLE THICKNESS mils	$(\sigma_1\sigma_2)_N^{\cdot}$ erg^2/cm.^{4}	σ_{av} erg/cm.^{2}	RANGE OF r A^o
1.0	0.242	0.49	550—720
3.0	0.162	0.40	400—600

This is reasonable, since textures in liquid crystals are easily changed by small mechanical disturbances such as movement of cover slips.

The above results show that both the growth rate and the nucleation rate are dependent on sample thickness. A possible explanation for the nucleation dependence is that in thin films, when one nucleus develops as a result of molecular organization, it induces the creation of other nuclei nearby and on the other side of the sample. In thicker samples, the opposite surface is further away from the first nucleus and is less likely to be influenced by it. The growth rate dependence on thickness is possibly due to higher viscosity in thinner samples, caused by orientation effects of the surface.

E. Depolarized Light Intensity

The depolarized light transmission technique has been used by many workers studying crystallization kinetics.[41-46]

The experimental procedure involves the measurement of the depolarized light intensity versus time. The DLI versus time plots are converted to fit the Avrami equation by using the following equation:

$$\theta_a = \frac{I_\infty - I_t}{I_\infty - I_o} = \exp(-Kt^n) \qquad \text{(IV-17)}$$

where I_t is the transmitted intensity at time t and I_o and I_∞ are the values of I_t at $t = 0$ and $t = \infty$ respectively. θ_a is the fraction of untransformed material. The parameters K and n in the equation describe the rate and mechanism of crystallization.

The DLI technique has some advantages over the measurement of crystallization kinetics by dilatometry or by differential thermal analysis. These are: the time required for temperature equilibrium is short, the inhomogeneity in temperature is minimized since the observed portion of the specimen is very small, and the use of a binocular tube enables one to follow the course of crystallization visually. However, the disadvantage of this method is the difficulty of interpreting the DLI on a molecular basis. This point has been discussed by Stein.[13,47]

The DLI technique is particularly useful in studying

the isotropic--cholesteric phase transition in cholesteryl myristate for two reasons. First, cholesteryl myristate exhibits a transition (described earlier) from an isotropic melt to the cholesteric mesophase upon cooling which occurs in two steps. A rapid transition to a turbid blue phase followed by a slower transition to a macroscopically ordered spherulitic state. Dilatometry[48] and differential scanning calorimetry are not sensitive to this slower transition but depolarized light intensity is sufficiently sensitive to detect the transition. Secondly, it is difficult to measure growth or nucleation rate in thick samples (demonstrated previously), so it is important to obtain overall rate kinetics in thick samples.

The DLI versus time was measured at several temperatures for 3 mil and 6 mil samples. The results are given in Figure IVE-1 and IVE-2. From these data, the Avrami exponent n and the rate constant K in equation IV-17 may be obtained by plotting $\ln(-\ln \theta_a)$ versus ln t. These plots are given in Figures IVE-3 and IVE-4. In constructing such plots, the induction period, τ , during which no interaction with the polarized light occurs, was subtracted from t. A summary of the results is given in Table IVE-1. It is seen that n is equal to 3. It is known from nucleation data presented earlier, that the process is sporadic and it is also known that the size of the spherulites exceeds the thickness of the sample. Therefore, n = 3 must mean that the growth is

TABLE IVE-1. SUMMARY OF KINETIC DATA FOR CHOLESTERYL MYRISTATE.

T°C	n	K, $min.^{-3}$	$t_{\frac{1}{2}}$, min.	τ, min.
3.0 MIL SAMPLE				
80.0	2.94	100×10^{-5}	8	4
80.5	3.00	11×10^{-5}	20	18
81.0	2.92	2.7×10^{-5}	40	55
6.0 MIL SAMPLE				
80	3.0	1420×10^{-5}	4.5	0.5
81	3.0	15.7×10^{-5}	20	15
82	3.1	2.11×10^{-5}	30	20

disc shaped.

The mathematical formulation of the kinetic phase changes and the derivation of the Avrami equation is found in many sources.[34,49] It is useful to consider the kinetic rate constant, K, given in the Avrami equation IV-17. It depends upon the kind of nucleation (sporadic or heterogeneous) and on the geometry of the growth. Table IVE-2 gives the expressions of K and the values of n for spherulitic growth and disc growth. It should be mentioned that the values of n in the heterogeneous case are given for the lower limit. It is possible that n for three-dimensional growth may have the range of $3 \leq n \leq 4$ and for two-dimensional $2 \leq n \leq 3$. For detailed explanation of these possibilities, the reader is referred to an extensive discussion given by Mandelkern.[34]

If the assumption is made that one primary nucleus gives rise to one disc or one spherulite, then by a direct measurement of both the rate of formation and growth, the crystallization rate constant K can be calcualted from the expressions of K given in Table IVE-2 for both the sporadic and the heterogeneous processes. A comparison can be made between this quantity and the corresponding value determined from measurements of the overall rate of crystallization. Such calculations were carried out for the formation of the two-dimensional spherulites in cholesteryl myristate. The results are given in Table IVE-3. In these calculations it was assumed that ρ_2/ρ_1 was equal to unity. This assumption

TABLE IVE-2. K AND n FOR VARIOUS TYPES OF NUCLEATION AND GROWTH

TYPE OF GROWTH	SPORADIC NUCLEATION		HETEROGENEOUS NUCLEATION	
	K	n	K	n
Spherulites	$(\pi/3)\frac{\rho_2}{\rho_1}\dot{N}G^3$	4	$\frac{4\pi}{3}\frac{\rho_2}{\rho_1}G^3\overline{N}$	3
Discs	$\frac{\pi}{3}d\frac{\rho_2}{\rho_1}\dot{N}G^2$	3	$2\pi d\frac{\rho_2}{\rho_1}G^2\overline{N}$	2

$\dot{N}$ = nucleation rate per unit volume

G = growth rate

$\overline{N}$ = number of nuclei per unit volume

d = thickness of the disc

ρ_2 = density of phase 2

ρ_1 = density of phase 1

TABLE IVE-3. COMPARISON OF K AS OBTAINED BY DEPOLARIZED LIGHT INTENSITY AND MICROSCOPY FOR 3.0 MIL CHOLESTERYL MYRISTATE SAMPLE.

$T^{o}C$	K	K (microscopy)	
	from DLI	Sporadic K	Heterogenous K
		$min.^{-3}$	$min.^{-2}$
79.8	---	162×10^{-5}	34.8×10^{-3}
80.0	100×10^{-5}	90×10^{-5}	32.1×10^{-3}
80.5	11×10^{-5}	13×10^{-5}	9.4×10^{-3}
81.0	2.7×10^{-5}	---	---

NOTE: THE VALUES OF N AND $\bar{N}$ ARE GIVEN IN TABLE IVD-4.

is justified since no difference between the density of the blue phase (ρ_1) and the density of the spherulitic phase (ρ_2), can be detected by dilatometry. The agreement between the two methods is very good (see Table IVE-3) for the case of sporadic rate constant only.

F. Characterization of the Blue Phase

It was shown in section C of this chapter that cholesteryl myristate exhibits a two step transition when cooled from the isotropic melt to the cholesteric mesophase. The first step is a rapid transformation to a turbid blue phase. This phase gives a diffuse circular Hv light scattering pattern which results from scattering by small particles randomly distributed, but of sizes smaller than the wavelength of light, not resolvable by the optical microscope. The objective of this section is to characterize the size of these particles using the photometric light scattering technique.

The measurements at high temperatures were made using a hot stage cell specially constructed for this purpose and described in Appendix II. The cell is heated electrically and the temperature is measured by means of a thermocouple system and it is regulated to within $\pm$ 0.1^{o}C.

In order to assure sufficient scattered intensity at high temperatures, a 16 mil sample thickness was prepared. The sample was heated to 90^{o}C and held at this temperature for half an hour, then quickly cooled to 82^{o}C. Temperature equillibrium was achieved within three minutes. From microscopic observation, it was known that the blue color at this temperature lasts for at least 25 minutes. Therefore it was essential to measure the scattered intensity in a period of less than 25 minutes. After each set of measurements, the initial point was measured again and no variation from

the initial value was observed, confirming that the entire set of measurements was done on the same phase. The sample was found to have 88% transmission at 82°C. The scattered intensity of the backgournd was subtracted from the experimental results.

The variation of I_{Vv} and I_{Hv} intensity with the scattering angle, θ, at 82°C is given in Figure IVF-1. It is evident from these curves that I_{Vv} is much greater than I_{Hv}. These results indicate that most of the scattered light arises from fluctuations in density and a very small amount arises from fluctuations in orientation.

The dependence of the $I_+(Hv)$ scattered intensity on polarization direction is given in Figure IVF-2 for various scattering angles. It is seen that there is no variation of I_+ with Ψ, indicating random orientation. These results confirm the conclusion made in section C.

These data can be analyzed in terms of the "random orientation correlation theory" discussed in chapter III, and will yield a measure of the correlation sizes.

As a first approximation, one can assume that the density correlation function $\gamma(r)$ and the orientation correlation function $f(r)$ can be represented by exponential functions, $\exp(-r/a_o)$ and $\exp(-r/a)$, respectively. Applying equations III-28 and III-26 to the data given, one obtains the plots given in Figures IVF-3 and IVF-4, for the density and orientation contributions respectively. It is seen in

both figures that the plots are two linear curves (A and B). When assuming a Gaussian form for the correlation function linearity is not obtained. A more accurate correlation function must be determined by Fourier inversion. However, the above data can still be used to give an upper and a lower limit to the value of a. The summary of the results is given in Table IVF-1. It is seen that the a values obtained from the density portion of the scattered light are less than the wavelength of light. This result is consistent with the microscopic observations discussed in section C of this chapter. The results in Table IVF-1 also indicate that the orientation correlations extend over larger distances than the density correlations.

The above experiments and calculations were done on the same sample at 83°C. The same results were obtained.

TABLE IVF-1. SUMMARY OF LIGHT SCATTERING RESULTS OF CHOLESTERYL MYRISTATE AT 82°C (λ_o = 5460 A°)

FIGURE	CONTRIBUTION	CURVE	a	
			κ	A°
IVF-3	DENSITY	A	0.31	3100
IVF-3	DENSITY	B	0.75	7500
IVF-4	ORIENTATION	A	0.44	4400
IVF-4	ORIENTATION	B	1.49	14900

C H A P T E R V

COMPARISONS, CONCLUSIONS and FUTURE WORK

A. Morphology

Liquid crystals are known to adopt a variety of morphologies within mesophases. These morphologies are referred tc as textures. The particular texture adopted by a mesophase depends on a variety of conditions. Among these are: the nature of the compound, the way in which the mesophase is produced and the nature and cleanliness of the supporting surface employed to mount the specimen. In order to define the various textures and the methods used to identify them, a brief discussion will be given for the two mesophases of interest in the present work, namely the smectic and the cholesteric phases. More detailed discussion of this subject, can be found in many sources.(3,7,50)

Smectic mesophase. Two textures are most commonly observed in the smectic mesophase. These are: (1) homeotropic texture is brought by either shearing the sample by cover slip movement or by cooling the isotropic liquid to the smectic phase. It is optically extinct between crossed polaroids since the optic axis in this texture is perpendicular to the supporting surface. Other methods for preparing the smectic homeotropic texture have been described in two books.(7,50)

(2) focal-conic texture is obtained when the smectic phase is supported between glass surfaces. Under the microscope, the preparation contains an arrangement of fine dark lines. These lines are ellipses and hyperbolas or portions of these. The lines appear in pairs and are related to each other in a focal-conic geometry. The ellipse is the locus of the vertices of cones of revolution passing through the hyperbola. The ellipses do not intersect one another and meet only tangentially giving rise to the so called focal-conic "domains". The tangential arrangement of the ellipses is referred to as polygonal texture. The mesophase in this texture is composed of cones whose bases are ellipses and whose apices are the meeting points of a number of hyperbolas. The "domain" of the cone of revolution for a circle and a line, which are related as focal-conic may be devided into series of curved, parallel strata which will entirely fill the cone. The molecules in the strata lie at right angles to these curved surfaces. Therefore at any given position in the "domain", a molecule lies with its major axis in the direction of a line joining a point on the ellipse to a point on the hyperbola. This arrangement causes the optic axis to continuously change throughout the "domain" of a focal-conic group. This is theoretically confirmed by Bragg.[51] The ellipses and hyperbolas are considered to be lines in the neighborhood of which the optic axial direction changes suddenly. Thus they represent optical

discontinuities, either within a "domain", in the case of a hyperbola or between "domains" in the case of an ellipse. As a ray of light passing close to such discontinuity is deviated, the discontinuity in the direction of the optic axis is seen as a black line. The same reasoning applies for crystalline spherulites. Other textures of the smectic mesophase include oily streaks ("stries huileuses") and "batonnets" (little rods).[3]

Cholesteric mesophase. The textures of the cholesteric mesophase and the conditions under which they are produced may be summarized as follows: when a cholesteric phase is produced by cooling the isotropic melt of the substance, confined between a slide and a cover slip, it usually appears as a fine cloud, the particles of which coalesce on further cooling to give a confused, and usually fine-grained structure, which shows certain resemblances to the focal-conic texture of the smectic phase, and depending on the preparation, definite focal-conic groups can be distinguished. The fine cloud texture often exhibits a weak blue or violet color when viewed between crossed polars.[52,53] This is called homeotropic cholesteric texture. Friedel[5] could not estimate the size of the particles in this texture because they are too small to be resolved under the microscope. The focal-conic texture in the cholesteric phase differs from that of the smectic in that it is always optically negative and that the major axes of the molecules lie at right angles

to the lines drawn between points on the ellipse and points on the hyperbolas, thus they lie parallel to the strata.[3,7,50] When the homeotropic or the focal-conic texture is disturbed by imparting small movements to the cover slip over the preparation, it gives rise to the planar texture. In some cases the change occurs very fast but it rarely forms spontaneously by just cooling. In the planar texture, the optic axis is normal to the plane of thepreparation, and the optical sign is negative. The planar cholesteric texture is very strongly optically active. The optical effects of this texture were first explained by deVries[54] and have been studied by Fergason et al.[55,56] When the sample is introduced into a wedge-shaped space provided by slightly tilted glass or mica plates, the planar texture is formed spontaneously on cooling the melt to the cholesteric phase. The optical patterns appear as bright and dark lines which follow the contours of the wedge. The separation between them corresponds to a constant change of thickness of the wedge. These lines were originally interpreted by Grandjean as planes of discontinuity perpendicular to surface and have been called Grandjean planes.[7,50] However recent work[4] showed that the Grandjean texture in a thin wedge is due to orientation influence of the surface.

It should be pointed out that the polygonal regions of the focal-conic texture discussed above represent a simple case and only observed under very favorable conditions.

In many cases in which the polygonal arrangement arises, the ellipses are not in the planes of the surfaces of the preparation, and the cones lie with their bases in various planes of inclination to the surface.(7)

In the present study concerning cholesteryl myristate morphology, it is shown that upon cooling from the isotropic melt to the cholesteric phase, the initial texture adopted is the "blue" form which is the homeotropic texture. It is demonstrated that the cholesteric homeotropic texture is composed of particles randomly distributed with sizes averaging 0.3 to 0.7 microns. These conclusions are in agreement with the observations made by other workers.(52,53) The second texture which is formed against the homeotropic texture is a more macroscopically ordered spherulitic texture. The microstructure of the spherulites are small focal-conic groups arranged in a radially symmetrical array. Similar results were observed by Elser(57) on cholesteryl n-alkyl carbonates.

It is found in this study that the orientation of the optic axes in the spherulitic form of the cholesteric phase was dependent on whether the cholesteric phase is produced by cooling from the melt or heating from the smectic phase. On heating to the cholesteric phase, the orientation of the optic axis was perpendicular to the spherulite radius, while when cooling from the melt, the optic axis was oriented at 45° to the radius. The change in optic axis direction is due to different orientation of

the focal-conic groups with respect to the radius of the spherulite. These differences are difficult to identify by microscopy while they are easily detected by light scattering experiments.

B. Light Scattering

It has been demonstrated in this thesis that the scattering of light from liquid crystals is similar to that observed for spherulitic polymers. The scattering is shown to arise principally from fluctuations in the orientation direction of anisotropic regions which have dimensions comparable with the wavelength of light. This conclusion is in agreement with the results of earlier studies made by Chatelain[9,10] on a nematic liquid crystal and more recently by Stein et al[13,14] on some cholesteryl esters. Chatelain studied the light scattering properties of p-azoxyanisole using a thin film which was obtained by melting the crystals between a glass slide and a cover slip. Both glass surfaces were rubbed to induce orientation in the system. He found that the intensity of the scattered light decreased as the angle of scattering increased, and also that nematic liquid crystals strongly depolarize light. It was found that the intensity of the scattered light can be expressed by:

$$E = K / (\sin \theta)^{1.6} \qquad \text{(VB-1)}$$

where E is the scattered intensity, K is a constant and θ is the scattering angle.

Chatelain was able to explain his results by assuming a model which consists of spherical regions of radius 0.1 micron and containing 10^6 molecules. The principal molecular axial direction fluctuates throughout the anistropic medium from one region to another. DeGennes[12] has shown that the strong angular dependence of scattering and the depolarization of light in nematic liquid crystals can be explained by long wavelength thermal fluctuations of orientation.

Other workers[58] have concluded that the scattering in nematic liquid crystals is also due to large fluctuations in the optical anisotropy of the material brought about by thermal fluctuations in the degree and orientation of alignment of the molecules.

C. Kinetics of the Isotropic-Cholesteric Phase Transition

Cholesteryl myristate is known to exhibit a transition from an isotropic melt to the cholesteric mesophase upon cooling. It is demonstrated above that this transition occurs in two steps. The first is a rapid transformation to a turbid "blue" homeotropic texture while the second is a much slower transition to a more macroscopically ordered form. The latter transformation can be described by nucleation and growth kinetics similar to those obeyed by crystalline polymers. The analysis of the kinetic rate constant, light scattering patterns and the microscopic

observations indicate that the macroscopic morphology is spherulitic, the microsturcture of which is composed of small focal-conic groups. It should be emphasized that the above results were obtained under isothermal conditions. The "blue" homeotropic texture has been observed also by others. Chistyakov and his co-workers[52] found that when slowly cooling cholesteryl myristate sample, they observed single-crystal cholesteryl type regions appearing against a background of the homeotropic texture.

The conslusion drawn from the results presented in this thesis is that the homeotropic cholesteric texture will always give rise to the more macroscopically ordered texture under isothermal conditions.

Price and Wendorff[59] have studied the transformation kinetics of cholesteryl myristate by dilatometric method. The transformation kinetics for the isotropic-cholesteric phase transition was found to fit the Avrami equation giving a value of n = 2. It was concluded that the liquid-cholesteric transformation takes place by the formation of disc-like nucleii which subsequently grow into rods. It was also found that the transition occurs in a very short time. At 2.2^{o}C supercooling, the half time of the transformation was one minute. In the present study it is found that while the transition to the "blue" homeotropic texture occurs in periods of one to two minutes and lasts for one to thirty minutes, depending on the temperature, before the other

texture appears. This latter texture transformation is slow and it takes periods of few minutes up to forty minutes. Comparing these results with the dilatometric results, it can be concluded that the dilatometric measurements are sensitive to the formation of the "blue" homeotropic texture while they are not sensitive to the second transition. In other words there is no volume change associated with the formation of the second texture. Therefore the conclusion can be drawn that while the transformation to the "blue" state is a true thermodynamic transition, the second is only a textural change or morphological transition. Both textures are in the same mesophase.

It was mentioned above that Price and Wendorff concluded that the "blue" texture nucleates as disc-like nucleii which grow into rods. The light scattering measurements of this texture presented in chapter IV section F of this thesis show that the scattered intensity was independent of the azimuthal scattering angle, Ψ , indicating spherical symmetry. If the particles were rods, the scattered intensity should vary greatly with this angle. The conclusion is then that the "blue" phase consists of spherical rather than rod-shaped aggregates.

It was concluded from the light scattering patterns and the microscopic pictures presented in chapter IV section C, that while the spherulites grow with time, the focal-conic

groups of the microstructure do not change in size, but increase in number. Therefore the growth rates reported in section D of chapter IV correspond to growth of spherulites by increasing the number of the microstructural entities (i.e. focal-conic groups). The interfacial energies obtained from the growth rates correspond to the energies required to bring focal-conic groups to the surface of the growing spherulite.

D. Future Work

It has been shown that the isotropic-cholesteric phase transition occurs in two steps. The size, shape and the kinetics of the second transformation has been characterized. The formation of the "blue" phase is fast and the size of the particles has been measured. The kinetics of this phase is that characterized by dilatometry. Therefore it is important to study the transformation kinetics of the "blue" phase by light scattering which gives the shape, orientation and the size of the regions formed. This could be done provided that a hot stage cell is available with which one can lower the temperature of the melt to the cholesteric phase very fast. It is essential that the temperature equilibrium be achieved in less than one minute (see text).

It has been shown that this "blue" phase lasts for time periods sufficient to perform angular dependence of the scattered light.

The average refractive index of a medium composed of two phases is

$$\bar{n} = \phi_1 n_1 + \phi_2 n_2 \qquad \text{IVD-1}$$

where $\bar{n}$ is the average refractive index of the medium, ϕ_1 and ϕ_2 are the volume fractions of phase 1 and phase 2 each of refractive index n_1 and n_2 respectively. The mean square average in fluctuation of the refractive index, $\langle \eta^2 \rangle$ is

$$\langle \eta^2 \rangle = \phi_1 (n_1 - \bar{n})^2 + \phi_2 (n_2 - \bar{n})^2 \qquad \text{VD-2}$$

Substituting equation VD-1 into equation VD-2, the result is

$$\langle \eta^2 \rangle = \phi_1 \phi_2 (n_1 - n_2)^2 \qquad \text{VD-3}$$

$\langle \eta^2 \rangle$ can be calculated from the absolute intensity of the scattered light, (see chapter III). Therefore a measurement of the intensity and angular distribution of the scattered light serves to characterize the size, and the volume fraction of the transformed region. In this case it would be possible to have a direct comparison between dilatometry and light scattering.

R E F E R E N C E S

1. F. Reinitzer, Monatsh.Chem., 9, 421 (1888)

2. O. Lehmann, Z.Physik Chem., 4, 462 (1889)

3. G.H. Brown and W.G. Shaw, Chem.Rev., 57, 1049 (1957)

4. G.H. Brown et al, CRC Critical Reviews in Solid State Sciences (1970)

5. G. Friedel, Ann.Physique, 18, 273 (1922)

6. J.L. Fergason, Sci.Am., 211, 77 (Aug.1964)

7. G.W. Gray, Molecular Structure and Properties of Liquid Crystals, Academic Press, N.Y. (1962)

8. K. Hermann, Z.Krist., 92, 49 (1935)

9. P. Chatelain, Acta Cryst., 1, 315 (1948)

10. P. Chatelain, Acta Cryst., 4, 453 (1951)

11. Orsay Liquid Crystal Group, J.Chem.Phys., 51, 816 (1969)

12. P.G. deGennes, Mol.Cryst. & Liq.Cryst., 7,325 (1969)

13. R.S. Stein, M.B. Rhodes & R.S. Porter, J.Coll. & Interf. Sci., 27, 336 (1968)

14. M.B. Rhodes, R.S. Porter, W. Chu & R.S. Stein, Mol.Cryst. & Liq.Cryst., 10,731 (1970)

15. R.S. Stein, Mol.Cryst. & Liq.Cryst., 6, 125 (1969)

16. E.M. Barrall, R.S. Porter & J.F. Johnson, J.Phys.Chem., 70, 385 (1966)

17. G.J. Davis & R.S. Porter, Mol.Cryst. & Liq.Cryst., 6, 377 (1970)

18. W. Chu, Light Scattering Studies of Polymers, Ph.D. Thesis, Univ. of Mass. (1969)

19. A. Plaza & R.S. Stein, J.Polym.Sci., 40, 267 (1959)

20. H.C. Van De Hulst, Light Scattering by Small Particles, Wiley, N.Y. (1957)

21. W. Prins et al, J.Am.Chem.Soc., 90, 3107 (1968)

22. R.S. Stein & M.B. Rhodes, J.Appl.Phys., 31, 1873 (1960)

23. R.S. Stein, Proceedings of the Interdisciplinary Conference on Electromagnetic Scattering, (M. Kerker,edit.) Pergamon Press, N.Y., 439 (1963)

24. S. Clough, J.J. vanAartsen & R.S. Stein, J.Appl.Phys., 36, 3072 (1965)

25. P. Debye & A.M. Bueche, J.Appl.Phys., 20, 518 (1949)

26. R.S. Stein & P.R. Wilson, J.Appl.Phys., 33, 1914, (1962)

27. R.S. Stein, P.F. Erhardt, S.B. Clough & G. Adams, J.Appl. Phys., 37, 3980 (1966)

28. E.M. Barrall, R.S. Porter & J.F. Johnson, Mol.Cryst. & Liq. Cryst., 3, 103 (1967)

29. C. Picot & R.S. Stein, ONR Technical Report No. 123, Polymer Research Institute, Univ. of Mass. (1969)

30. M.B. Rhodes & R.S. Stein, J.Polym.Sci., 62, 584 (1962)

31. V.G. Baranov, A.V. Kenarov & T.I. Volkov, J.Polym.Sci., Part C, 30, 271 (1970)

32. Fred Gormick & J.D. Hoffman, Industrial & Eng.Chem., 58, 41 (1966)

33. F.P. Price, Encyclopedia of Polym.Sci. & Technology, 8, 63 (1968)

34. L. Mandelkern, Crystallization of Polymers, McGraw Hill Book Co., Inc., N.Y. (1964)

35. G.J. Davis, R.S. Porter & E.M. Barrall, Mol.Cryst. & Liq. Cryst., 10, 1 (1970)

36. A. Sharples, Polymer, 3, 250 (1962)

37. R.S. Stein et al, J.Polym.Sci. Part A3, 3041 (1965)

38. J.N. Hay, J.Polym.Sci., Part A3, 433 (1965)

39. F.P. Price, Nucleation, chap.8, (A.C.Zettlemoyer,edit.) N.Y. (1970)

40. D. Turnbull and J.C. Fisher, J.Chem.Phys., 17,71 (1949)

41. F.P. Price, General Electric Research Lab. Report RL-774 (1952)

42. J. Magill, Brit.J.Appl.Phys., 12, 618 (1961); Polymer, 2, 221 (1961)

43. B. Levy,. J.Appl.Polym.Sci., 5, 408 (1961)

44. I. Kirshenbaum et al, J.Polym.Sci., B, 2, 897 (1964)

45. F.L. Binsbergen, J.Macromol.Sci.B, 4, 837 (1970)

46. F.L. Binsbergen and M. DeLange, Polymer, 11, 309 (1970)

47. S. Clough, M.B. Rhodes & R.S. Stein, J.Polym.Sci., C, 18, 1 (1967)

48. F.P. Price & J. Wendorff, private communication.

49. A. Sharples, Introduction to Polymer Crystallization, Edward Arnold (Publishers), London (1966)

50. N.H. Hartshorne & A. Stuart, Crystals and the Polarizing Microscope, 4th edition, Edward Arnold & Co., London (1970)

51. Sir W. Bragg, Nature, 133, 445 (1934)

52. I.G. Chistyakov & L.A. Gusokova, Soviet Physics--Crystallography, 14, 132 (1969)

53. R.D. Emulat, Mol.Cryst. & Liq.Cryst., 3, 405 (1968)

54. A. deVries, Acta Crystallogr., 4, 219 (1951)

55. J.L. Fergason, Mol.Cryst., 1, 293 (1966)

56. J.L. Fergason, N.N. Goldberg & R.J. Nodalin, Mol.Cryst., 1, 309 (1966)

57. W. Elser, Liquid Crystals, Gordon & Breach, N.Y. (1967)

58. J.D. Litster& W. Stinson III, J.Appl.Phys., 41, 996 (1970)

59. F.P. Price & J.H. Wendorff, paper will appear in J.Phys. Chem., Sept. (1971)

60. R.S. Stein and J. Keane, J.Polym.Sci., 17, 21 (1955)

61. B.R. Jennings & H.G. Jerrad, J.Polym.Sci., A, 2, 2025 (1961)

62. A.L. Plaza, M.S. Thesis, Univ. of Mass., Amherst (1959)

63. A.J. Davis & R.S. Porter, Mol.Cryst. & Liq.Cryst., 10, 1, (1970)

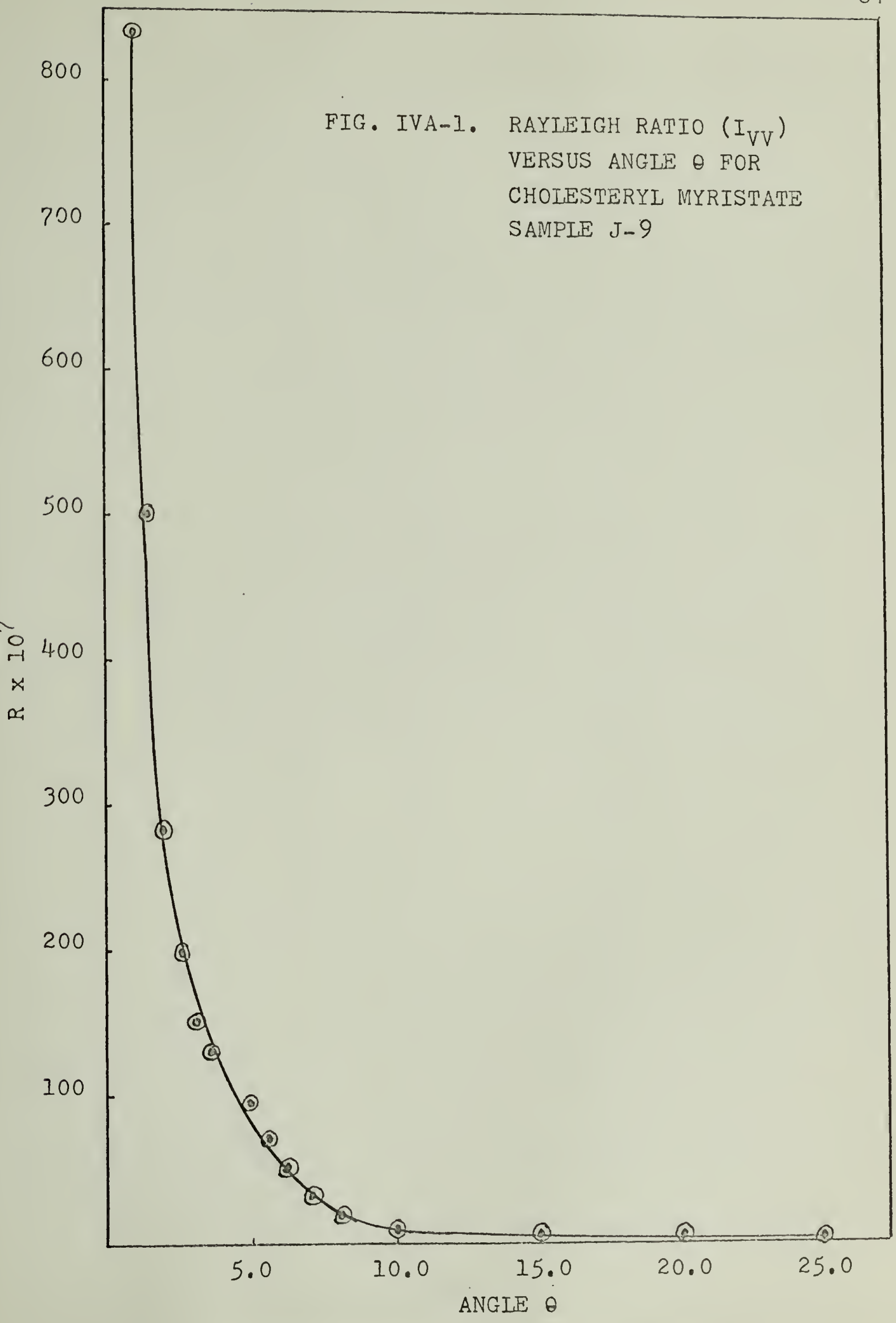

FIG. IVA-1. RAYLEIGH RATIO (I_{VV}) VERSUS ANGLE θ FOR CHOLESTERYL MYRISTATE SAMPLE J-9

FIG. IVA-2. RAYLEIGH RATIO (I_{HV}) VERSUS ANGLE θ FOR CHOLESTERYL MYRISTATE SAMPLE J-9

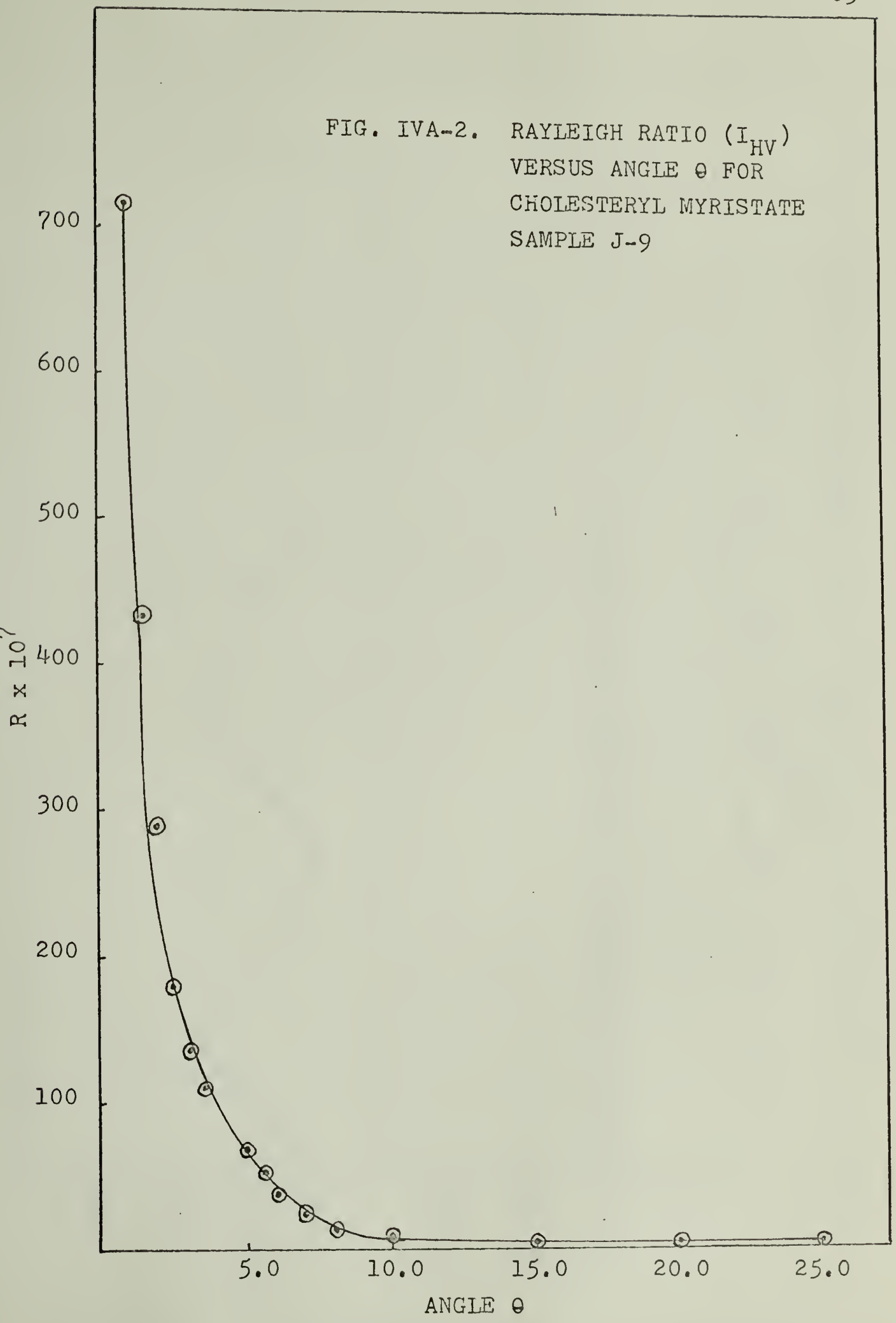

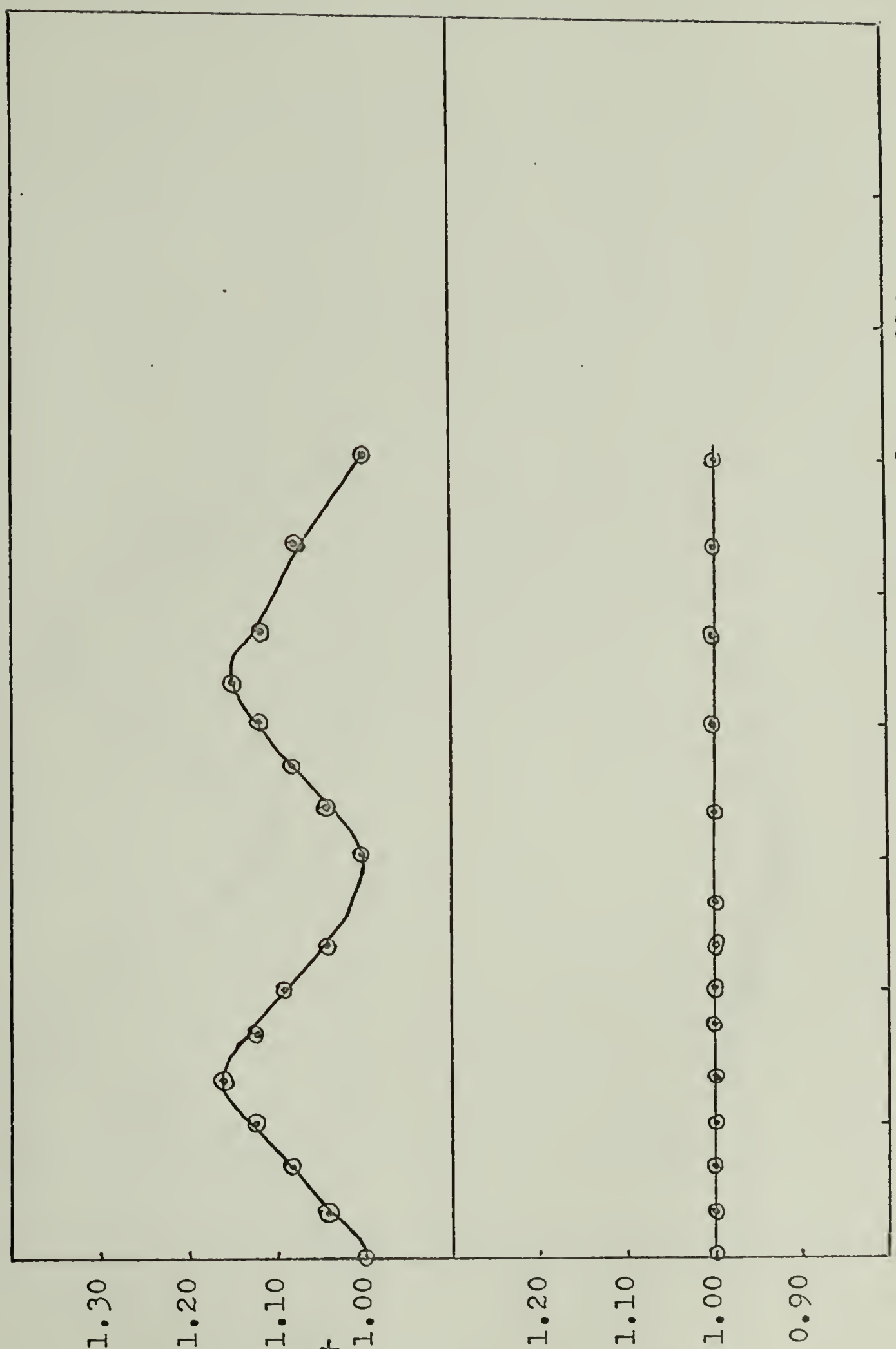

FIG. IVA-3. VARIATION OF $I_{\perp}$ AND $I_{=}$ WITH ψ FOR CHOLESTERYL MYRISTATE SAMPLE J-9 AT $\theta = 2^{\circ}$

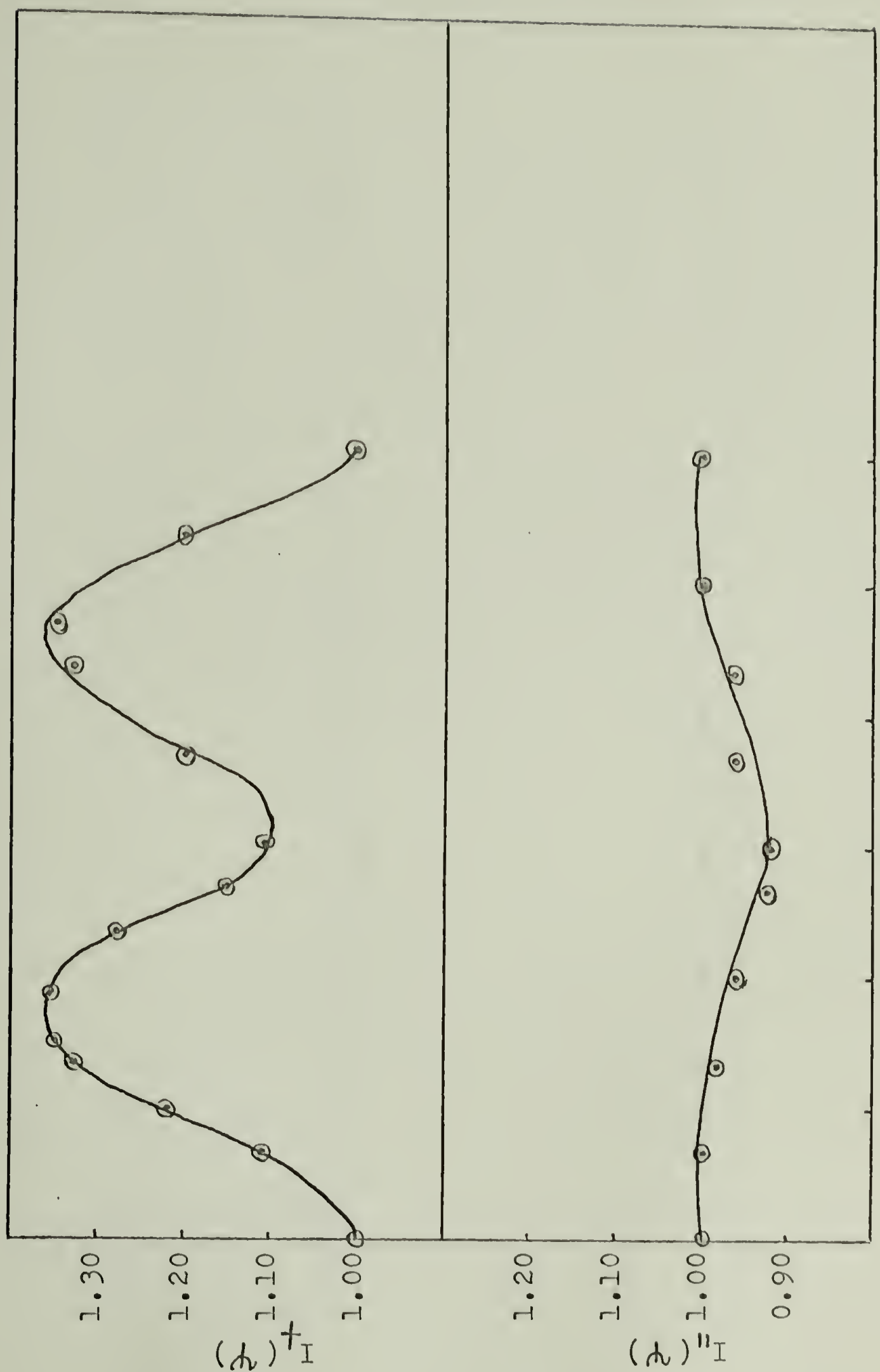

FIG. IVA-4. VARIATION OF I_+ AND $I_=$ WITH ψ FOR CHOLESTERYL MYRISTATE SAMPLE J-9 AT $\theta = 5^\circ$

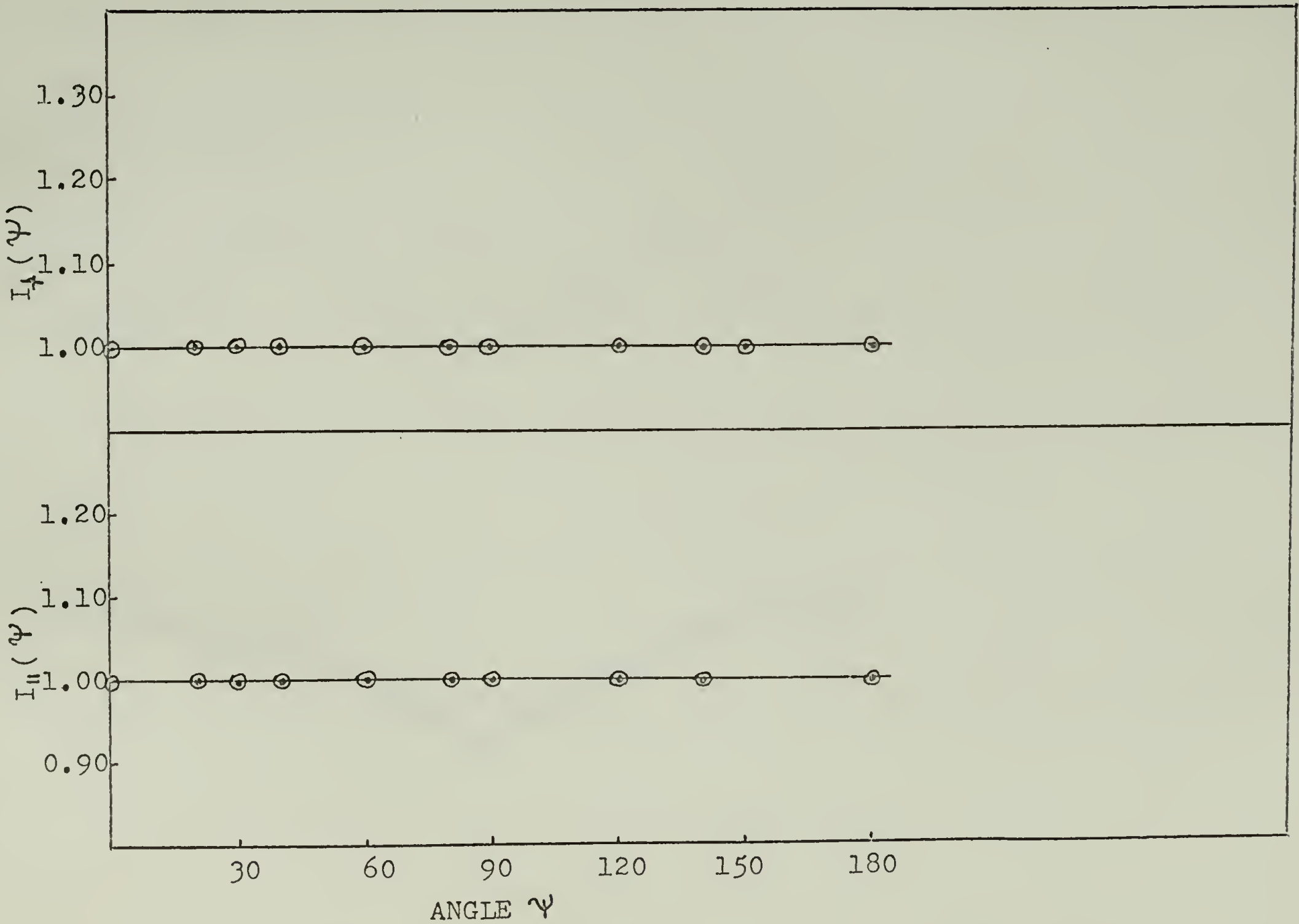

FIG. IVA-5. VARIATION OF $I_\perp$ AND $I_\parallel$ WITH Ψ FOR CHOLESTERYL MYRISTATE SAMPLE J-9 AT $\theta = 10^\circ$

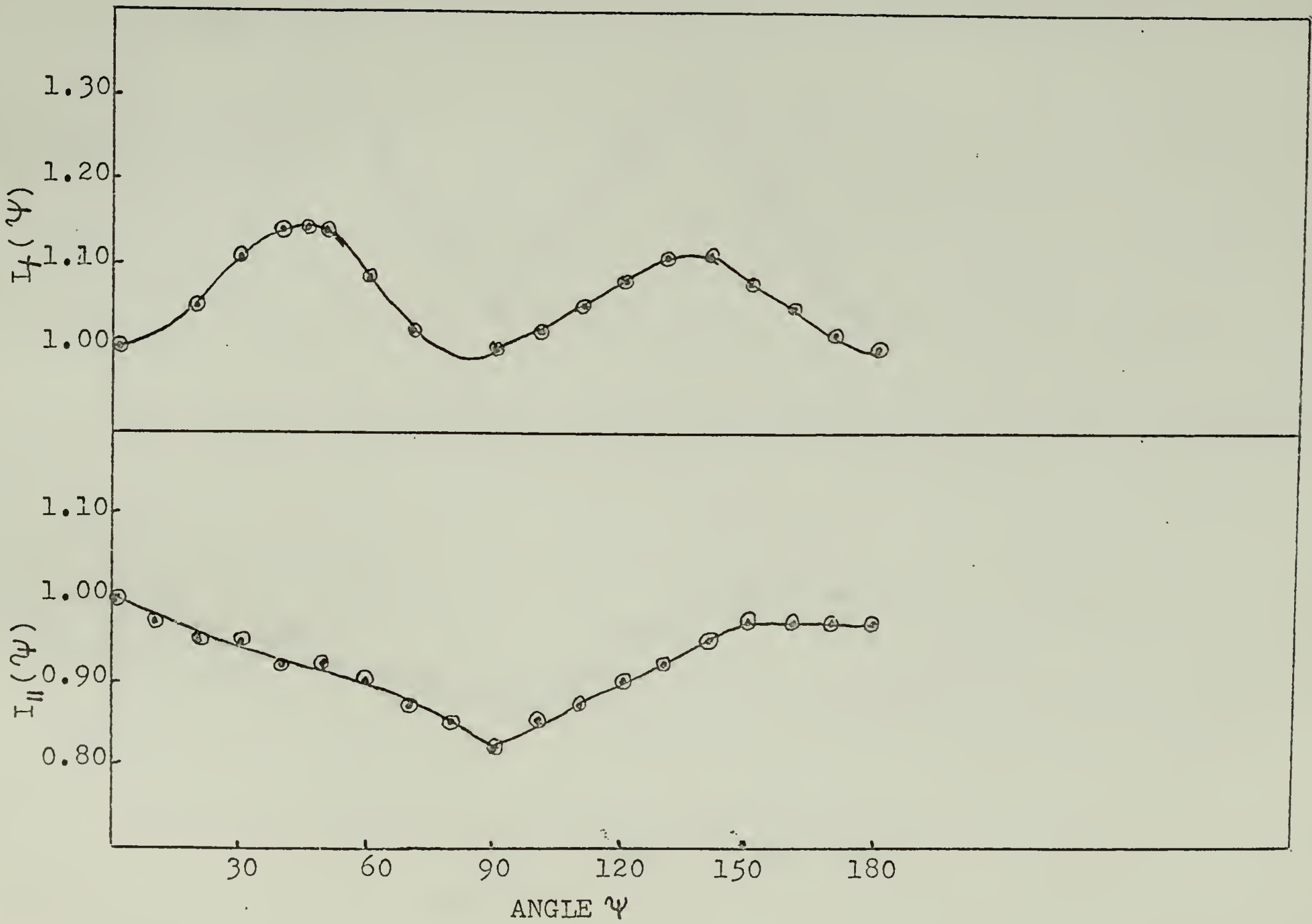

FIG. IVA-6. VARIATION OF I_+ AND I_{II} WITH Ψ FOR CHOLESTERYL MYRISTATE SAMPLE J-8 AT $\Theta = 2^\circ$

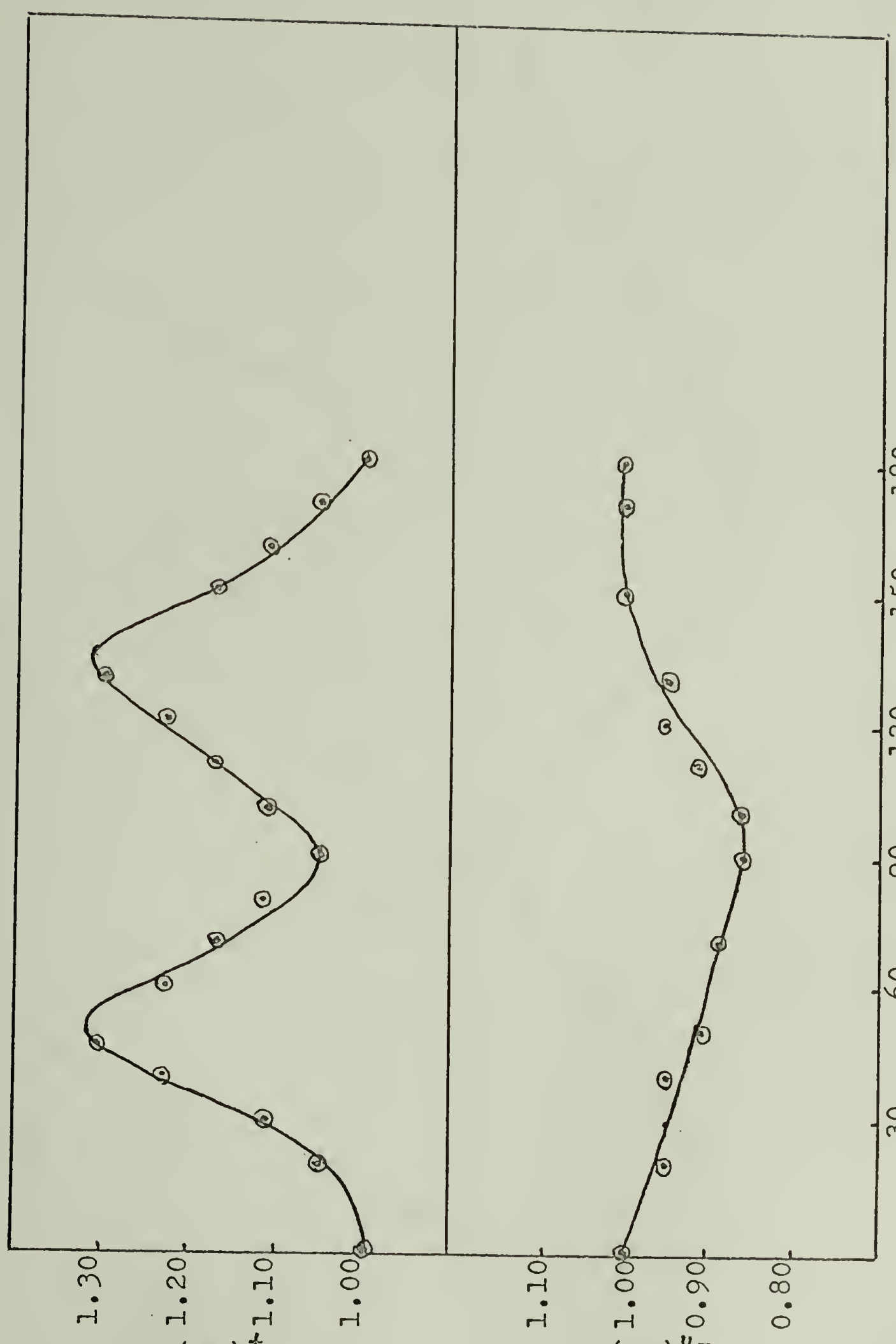

FIG. IVA-7. VARIATION OF I_+ AND $I_{||}$ WITH Ψ FOR CHOLESTERYL MYRISTATE SAMPLE J-8 AT $\theta = 5^{\circ}$

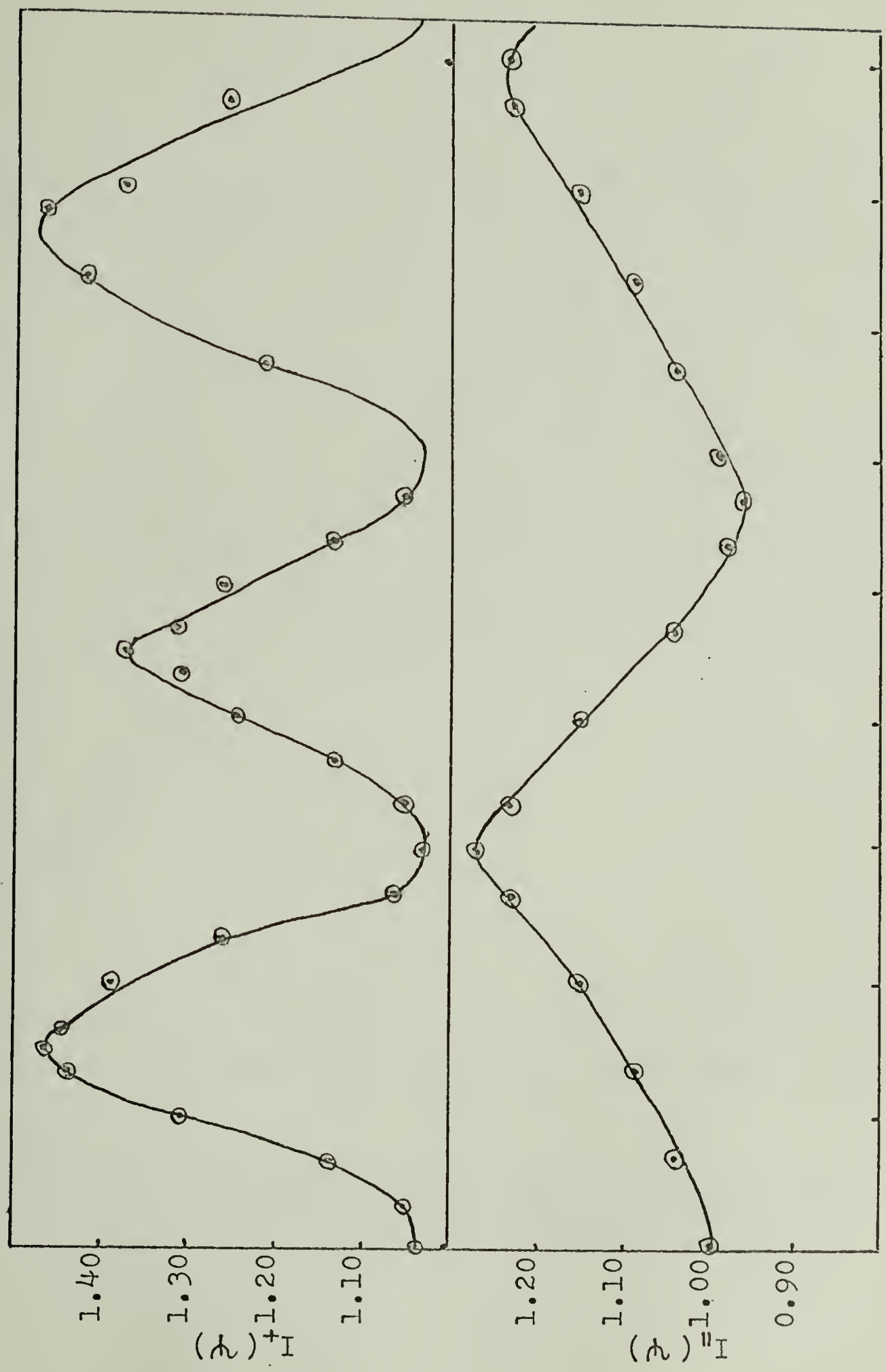

FIG. IVA-8. VARIATION OF I_+ AND $I_{||}$ WITH ψ FOR CHOLESTERYL MYRISTATE SAMPLE J-1 AT $\theta = 5^\circ$

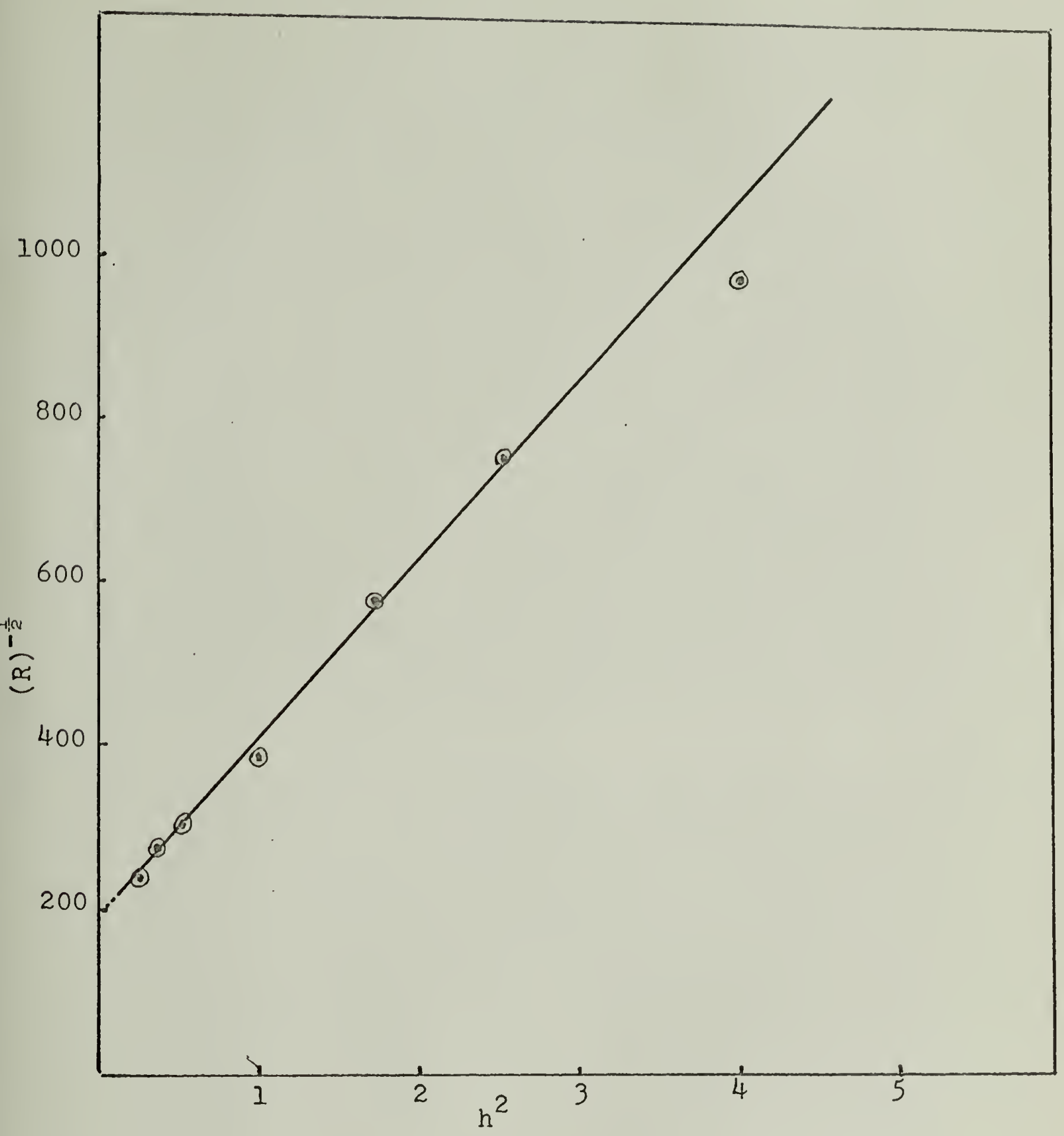

FIG. IVA-9. RECIPROCAL SQUARE ROOT OF RAYLEIGH RATIO (I_{HV}) VS. h^2 FOR CHOLESTERYL MYRISTATE SAMPLE J-9

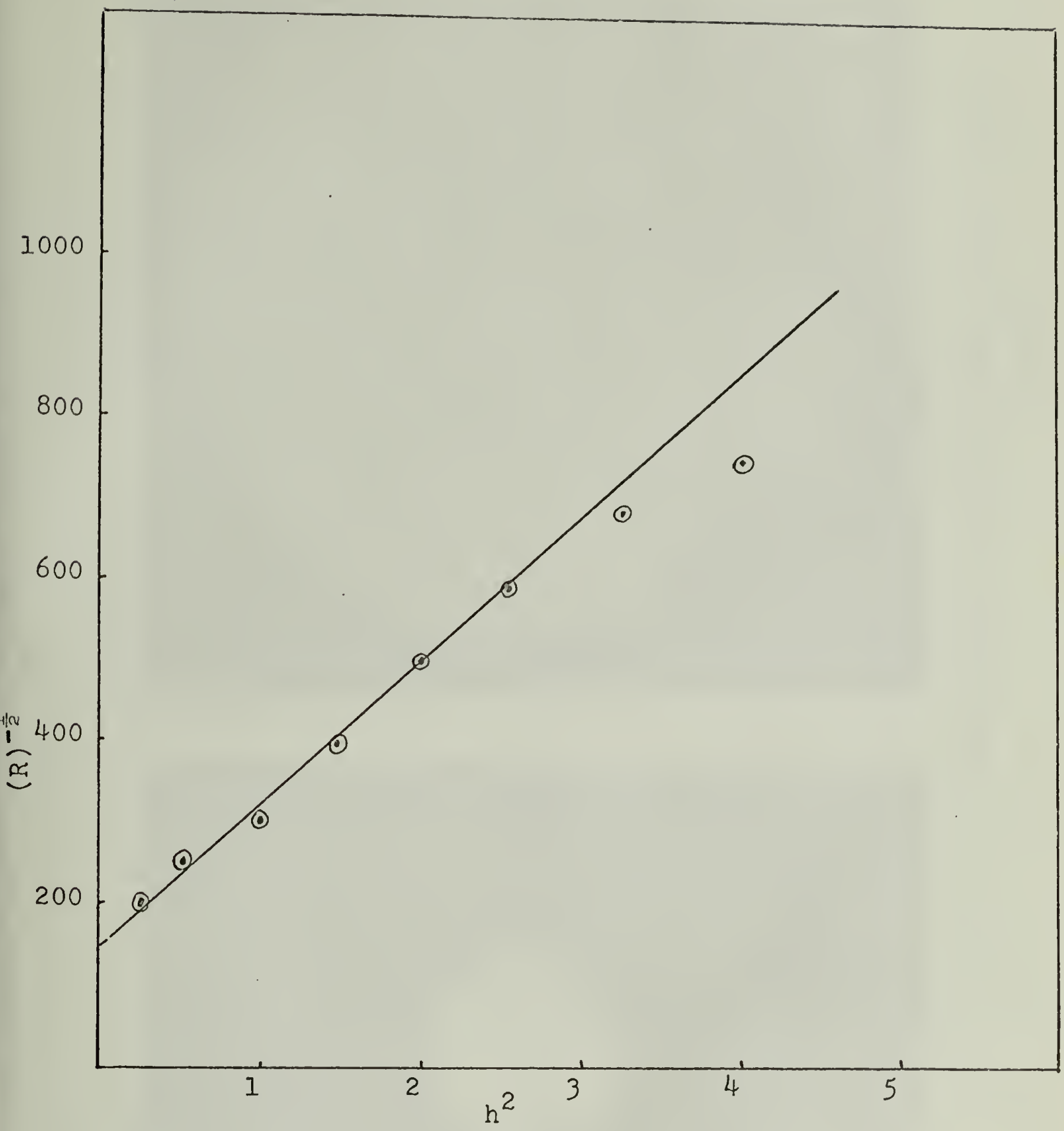

FIG. IVA-10. RECIPROCAL SQUARE ROOT OF RAYLEIGH RATIO (I_{HV}) VS. h^2 FOR CHOESTERYL MYRISTATE SAMPLE J-8

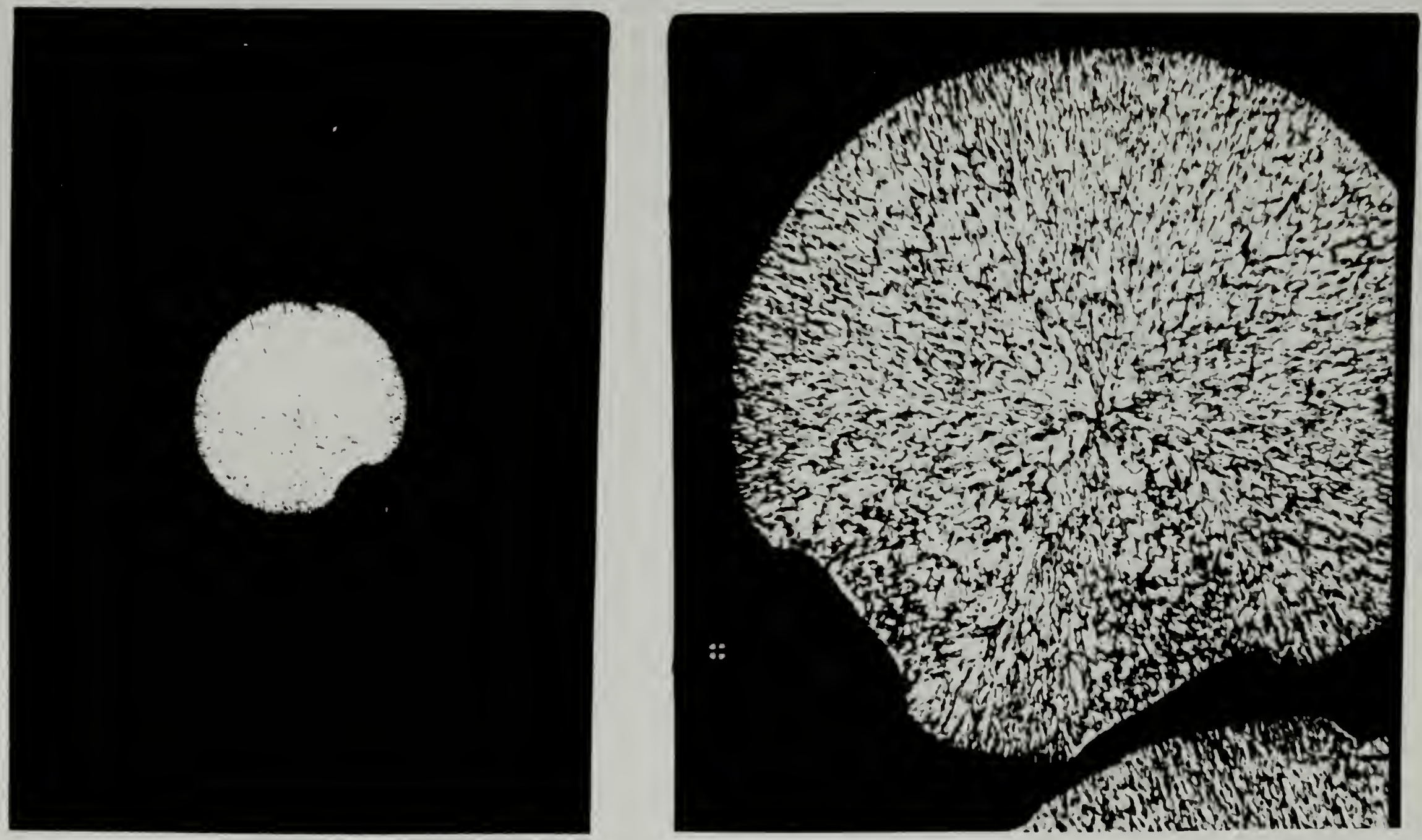

FIG. IVB-1. PHOTOMICROGRAPHS OF 1.5 MIL CHOLESTERYL MYRISTATE SAMPLE AT 80°C AFTER 13 AND 20 MINUTES.

80 μ

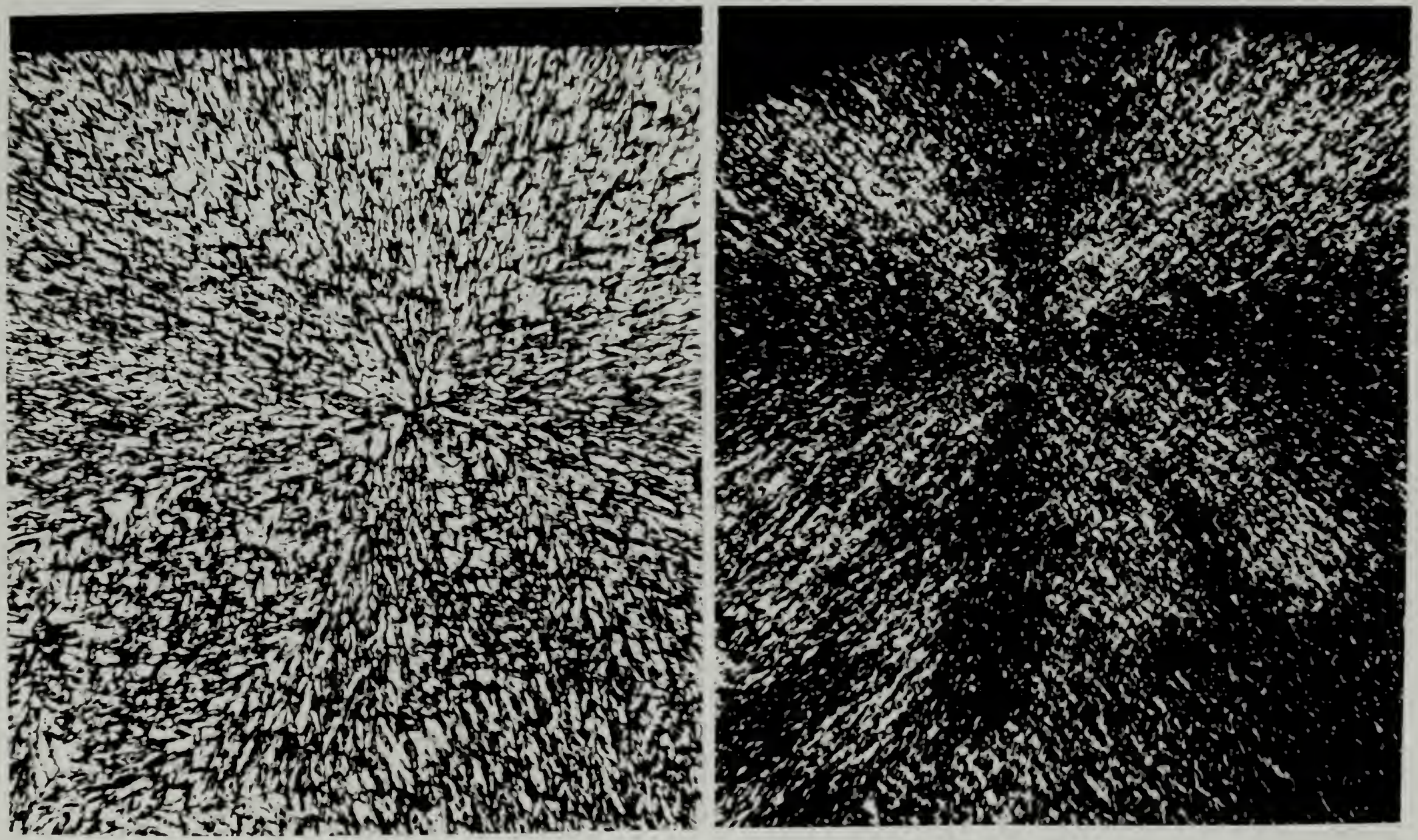

FIG. IVB-2. PHOTOMICROGRAPHS OF 1.5 MIL CHOLESTERYL MYRISTATE SAMPLE AT 80°C., WHEN COOLING FROM THE ISOTROPIC MELT (left) AND WHEN HEATING FROM THE SMETIC PHASE (right). —— 80 μ

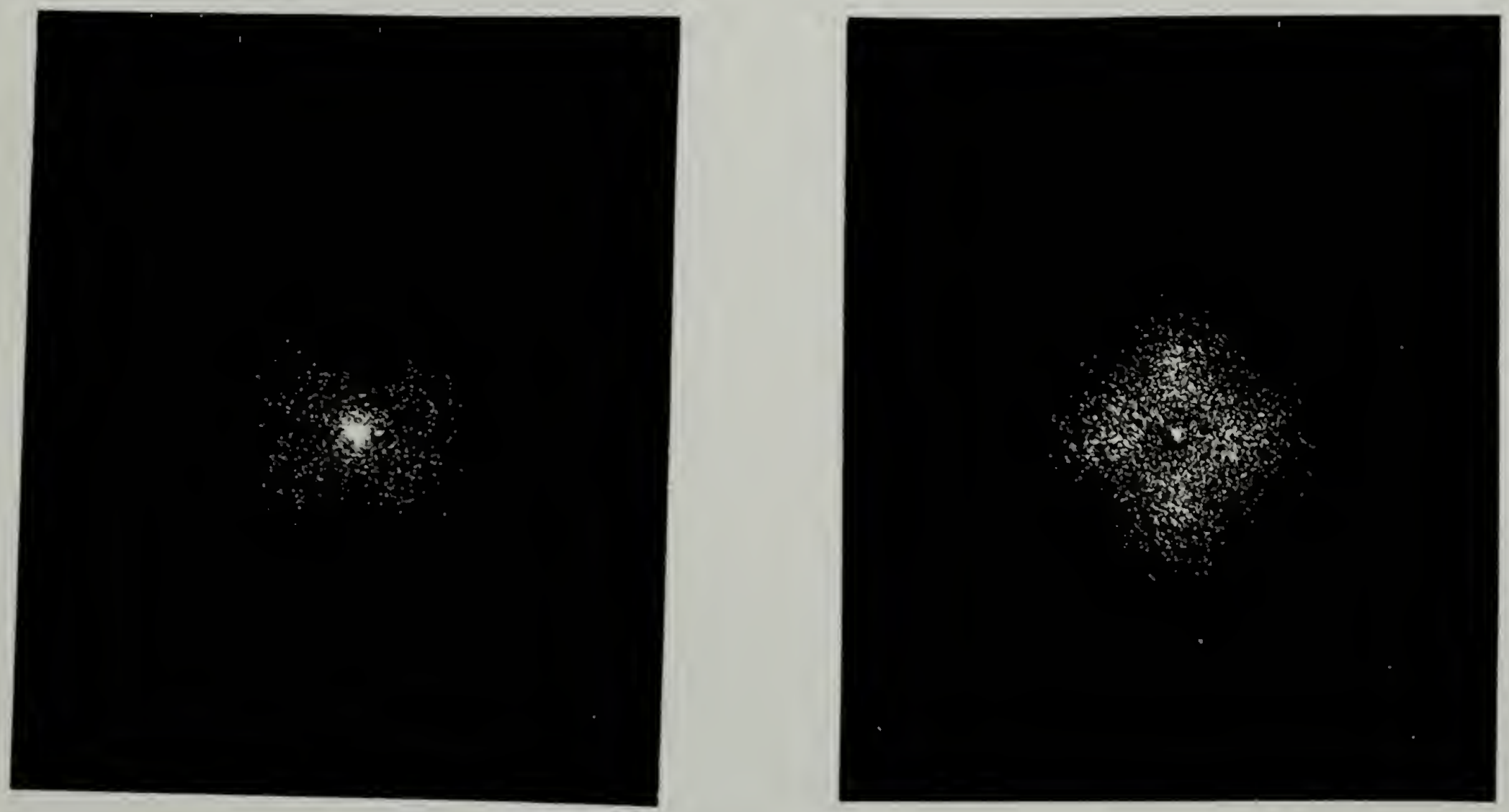

FIG. IVB-3. Hv LIGHT SCATTERING PATTERNS AT 80°C. OF 1.5 MIL CHOLESTERYL MYRISTATE WHEN COOLING (left) FROM ISOTROPIC MELT AND WHEN HEATING (right) FROM THE SMETIC PHASE.

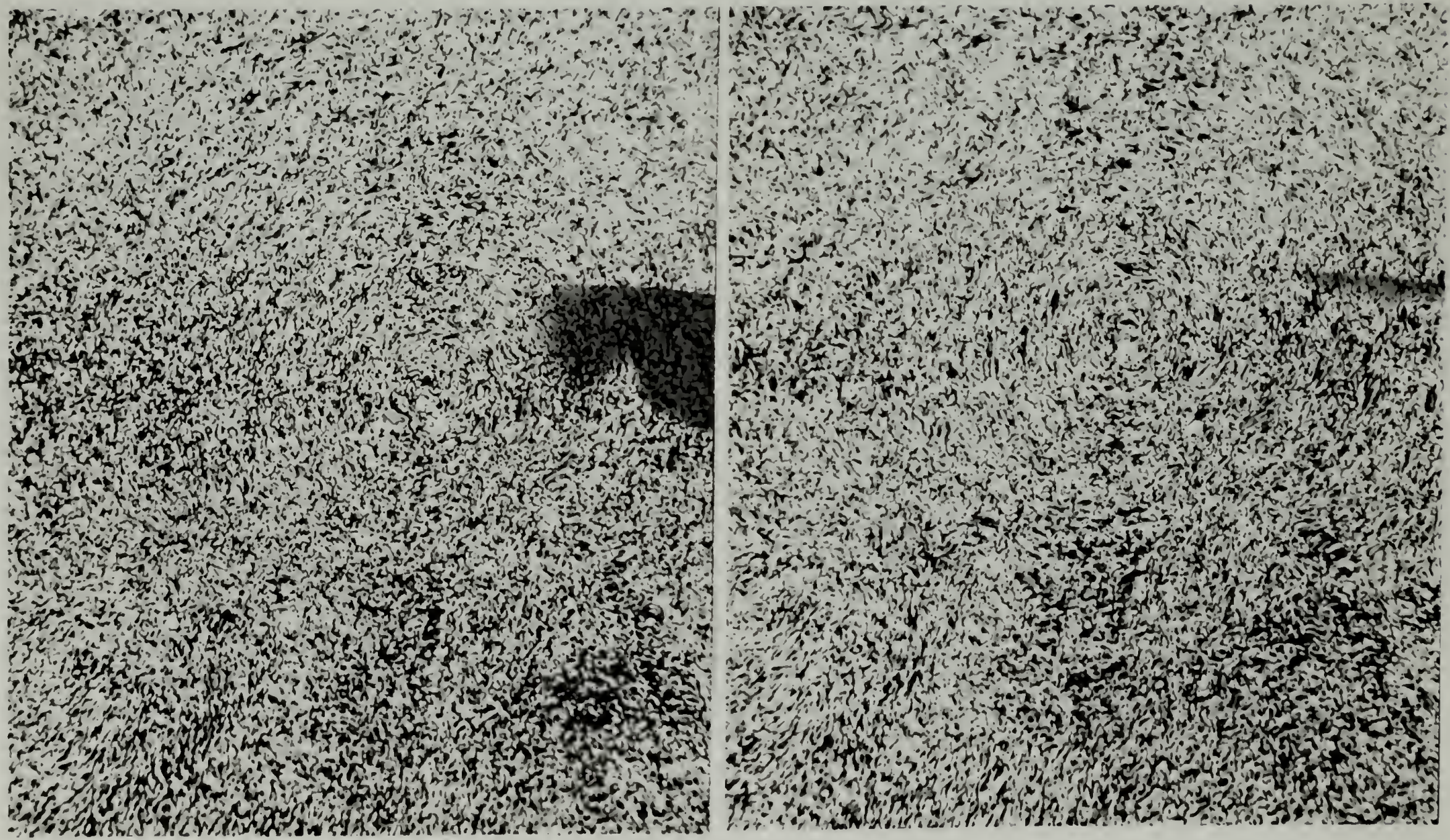

FIG. IVB-4. PHOTOMICROGRAPHS OF 1.5 MIL CHOLESTERYL MYRISTATE SAMPLE AT 75°C. WHEN COOLED FROM 80°C. (left) AND WHEN HEATED FROM 60°C. (right). —— 80μ

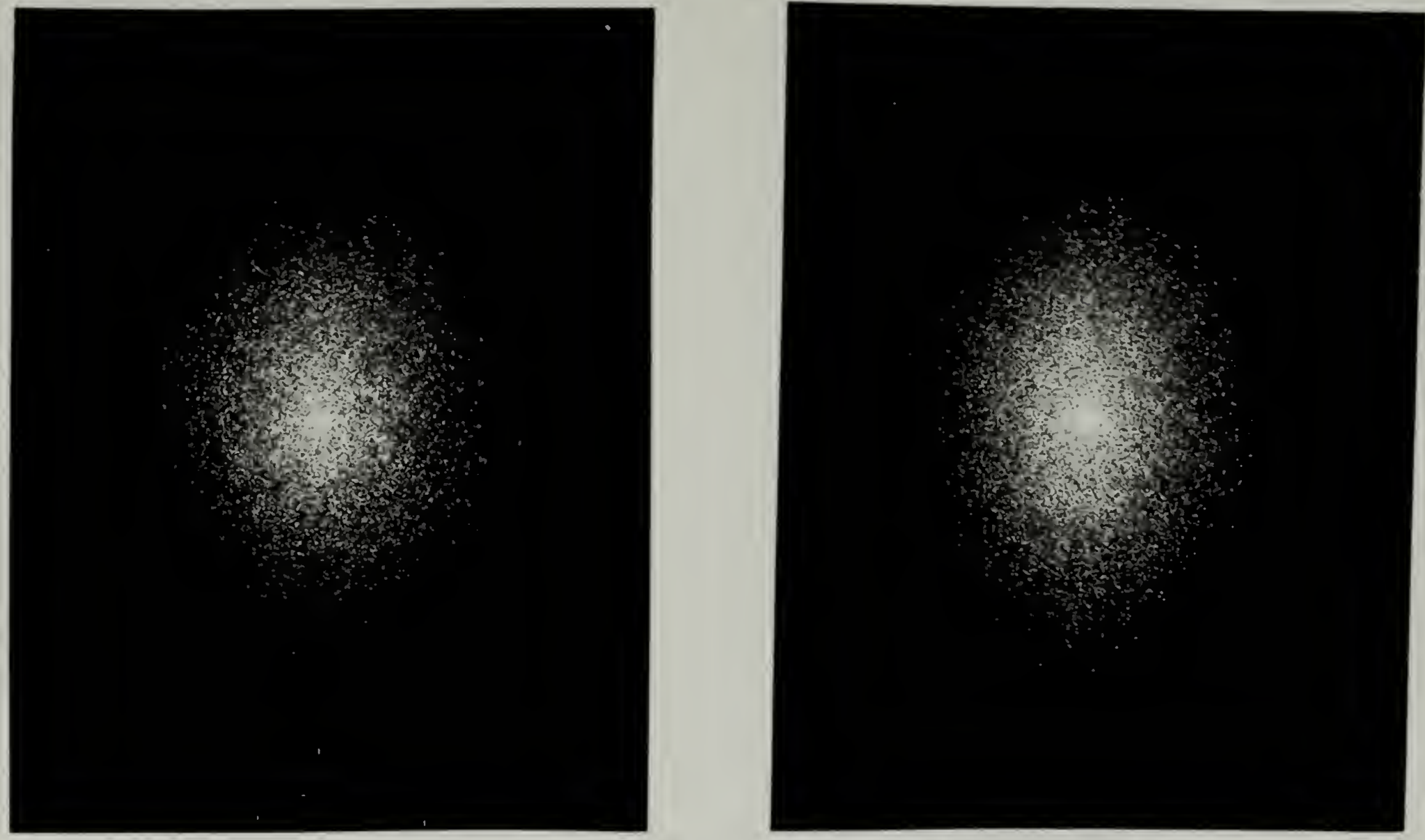

FIG. IVB-5. Hv (left) AND Vv (right) LIGHT SCATTERING PATTERNS OF 1.5 MIL CHOLESTERYL MYRISTATE SAMPLE AT 75°C.

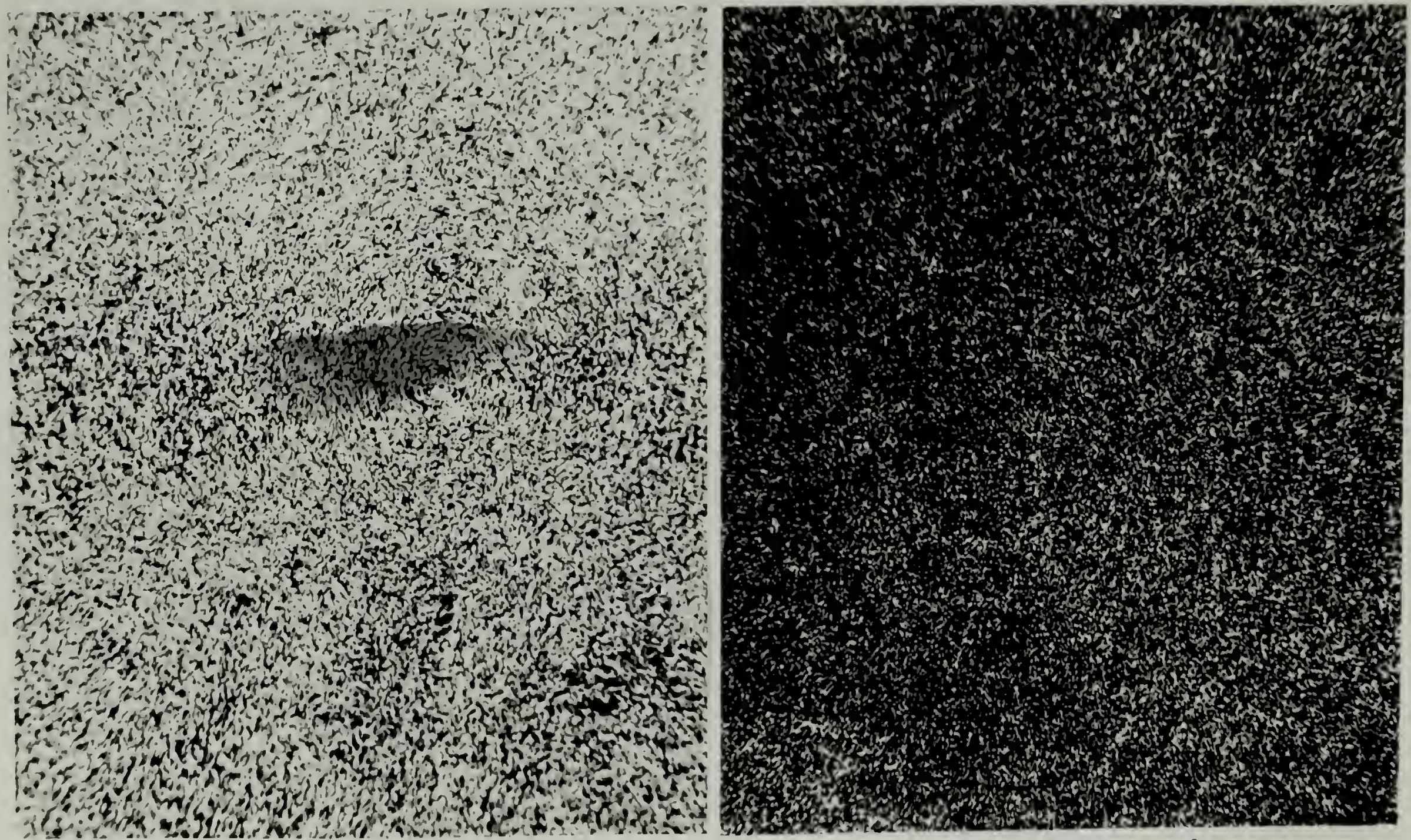

FIG. IVB-6. PHOTOMICROGRAPHS OF 1.5 MIL CHOLESTERYL MYRISTATE SAMPLE AT 60°C. WHEN COOLED FROM 75°C. (left) AND WHEN HEATED FROM 30°C. (right). —— 80 μ

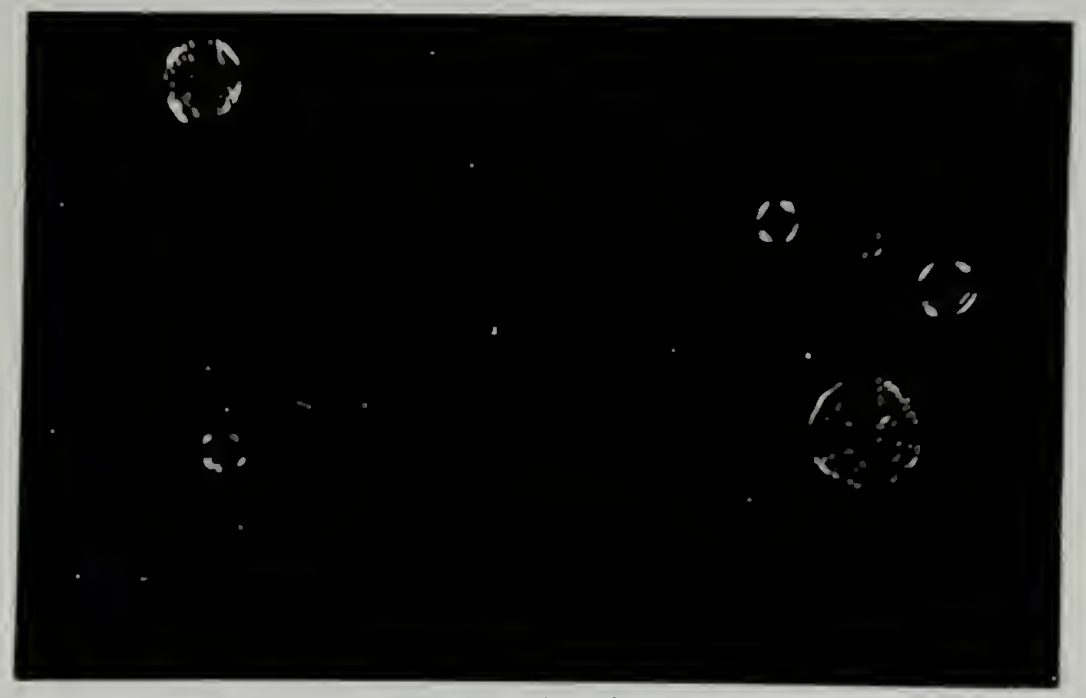

15 min.

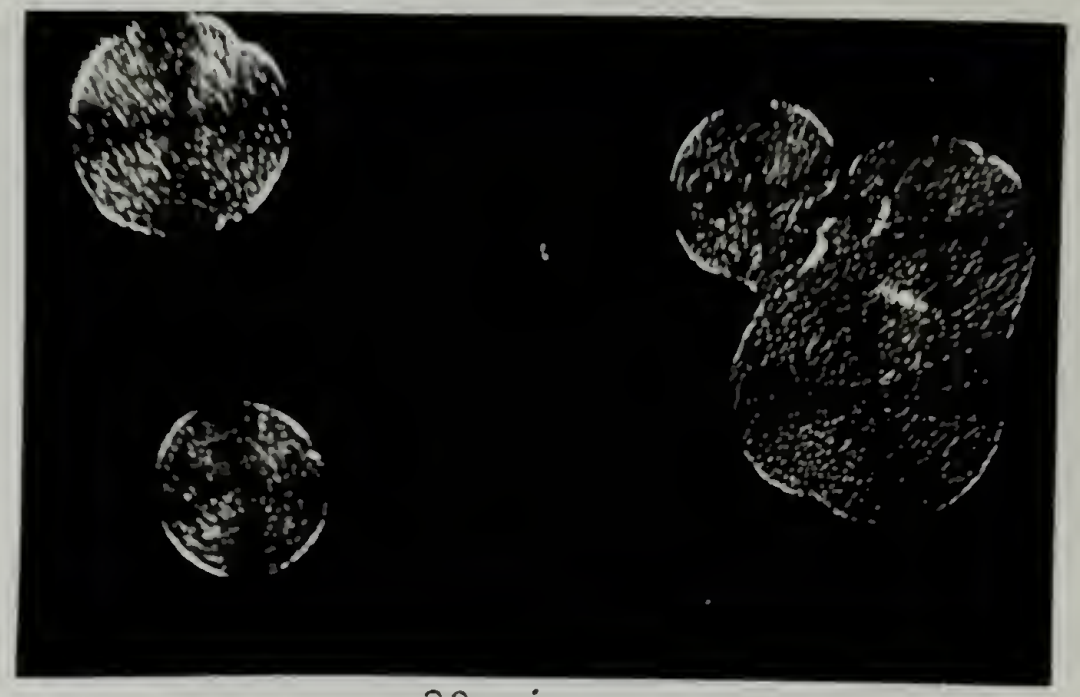

30 min.

45 min.

60 min.

FIG. IVC-1. PHOTOMICROGRAPHS OF 0.5 MIL CHOLESTERYL MYRISTATE SAMPLE AT 80°C. AT TIME INTERVALS.

80μ

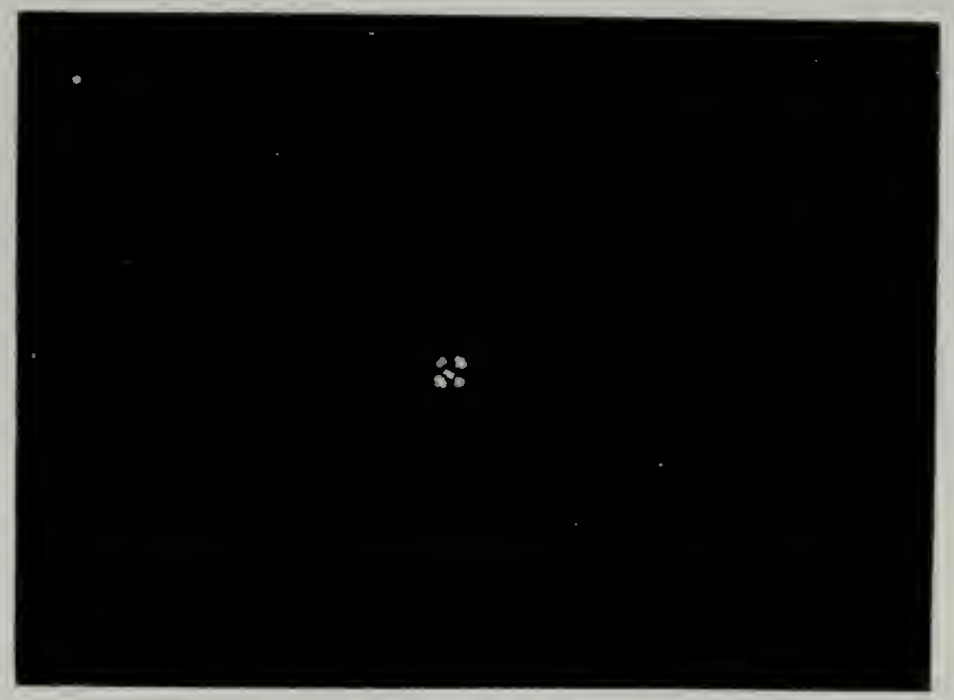

15 min.

30 min.

45 min.

60 min.

FIG. IVC-1b. Hv LIGHT SCATTERING PATTERNS OF 0.5 MIL CHOLESTERYL MYRISTATE SAMPLE AT 80°C AT DIFFERENT TIME INTERVALS.

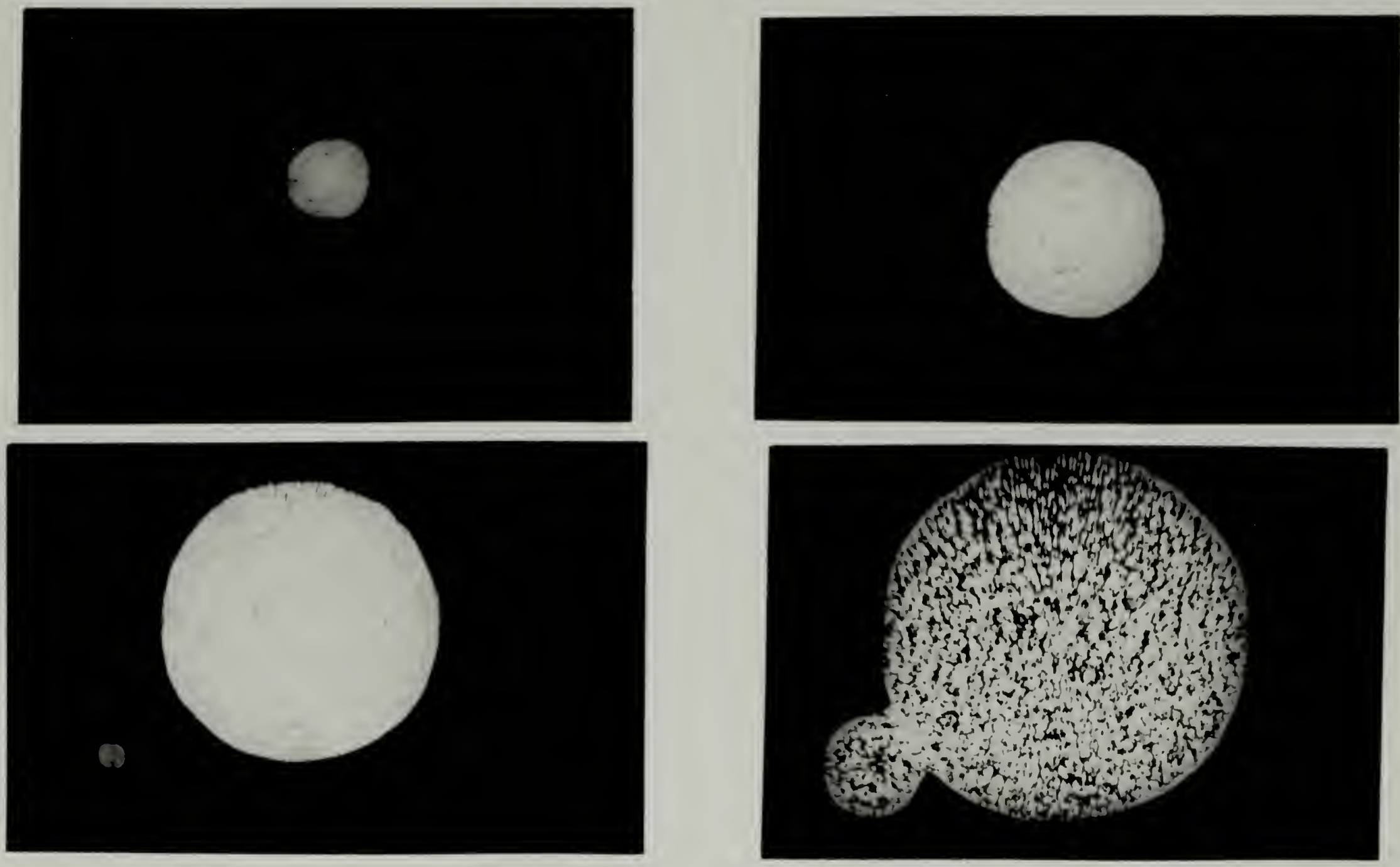

FIG. IVC-2. PHOTOMICROGRAPHS OF 1.5 MIL CHOLESTERYL MYRISTATE SAMPLE AT 79.8°C. AT TWO MINUTE TIME INTERVALS.

80μ

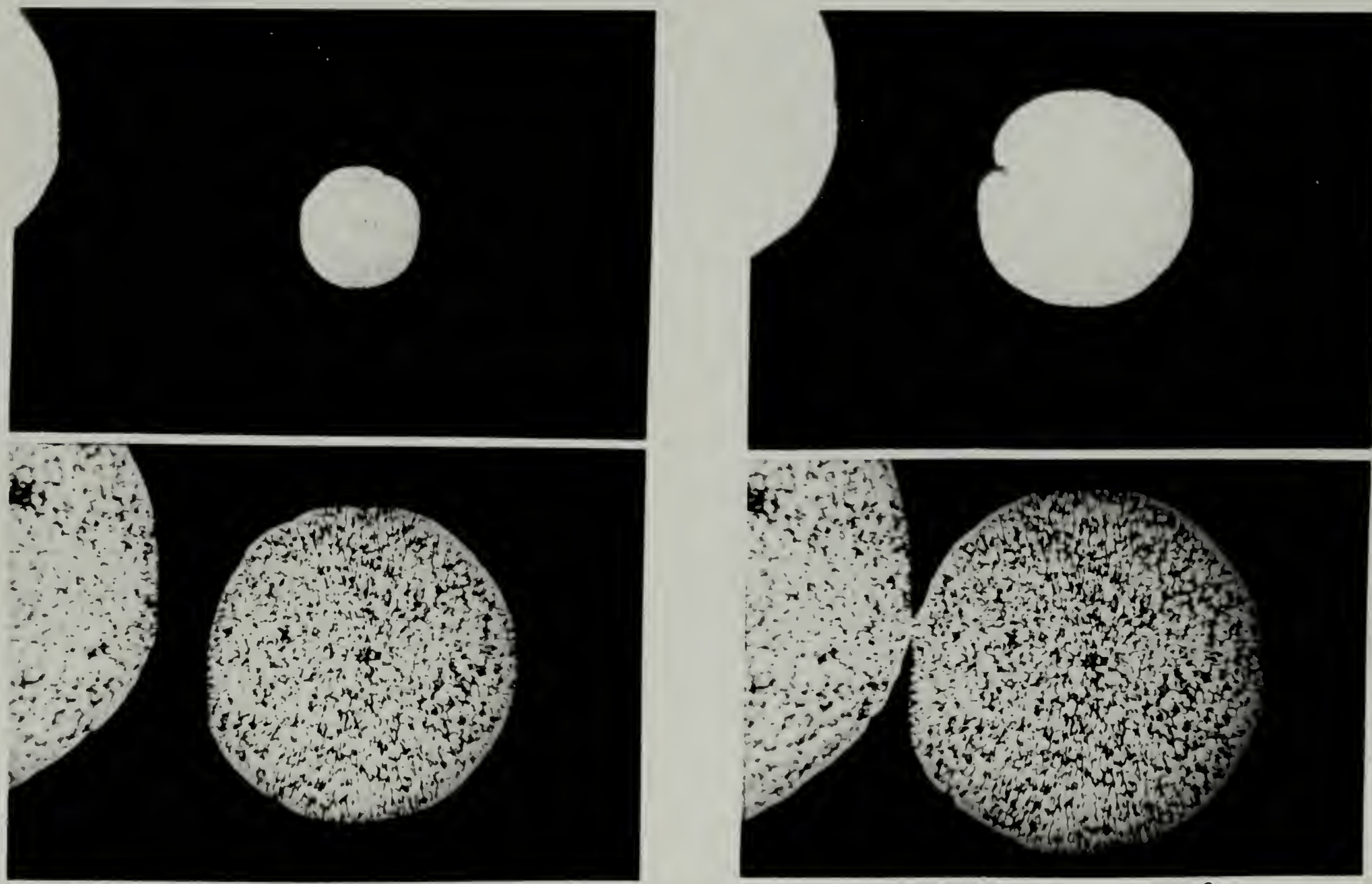

FIG. IVC-3. PHOTOMICROGRAPHS OF 1.5 MIL CHOLESTERYL MYRISTATE SAMPLE AT 79.8°C. (AT A DIFFERENT POSITION IN THE SAMPLE FROM THAT OF FIG. IVC-2) TAKEN AT TWO MINUTE TIME INTERVALS. —— 80μ

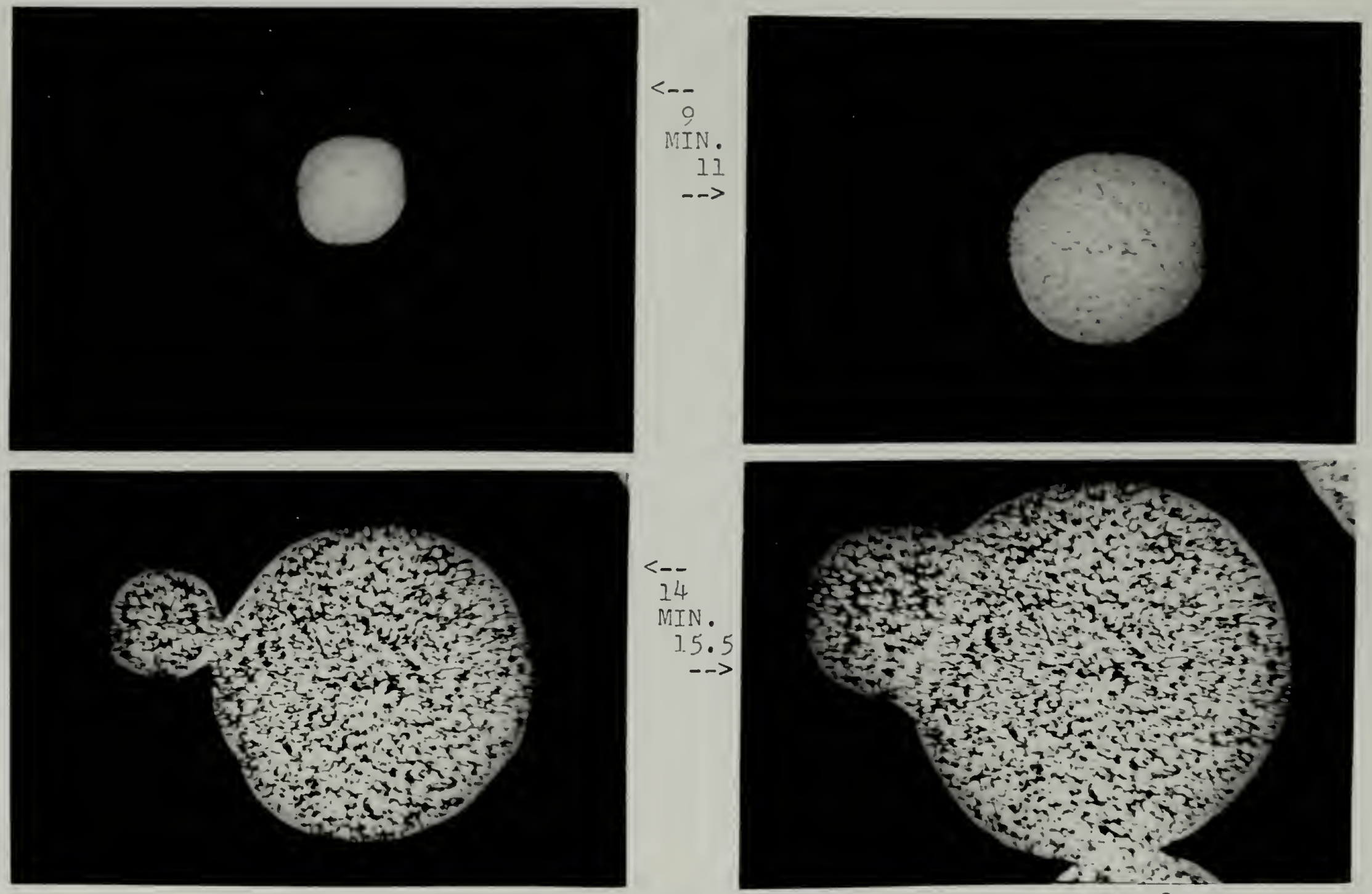

FIG. IVC-4. PHOTOMICROGRAPHS OF 1.5 MIL CHOLESTERYL MYRISTATE SAMPLE AT 80°C. AT DIFFERENT TIME INTERVALS.

15 min.

20 min.

30 min.

FIG. IVC-5. Hv LIGHT SCATTERING PATTERNS FOR 1.5 MIL CHOLESTERYL MYRISTATE SAMPLE AT 80°C. AT DIFFERENT TIME INTERVALS. ⌊——⌋ = 1°

<-- 25 min. 29 -->

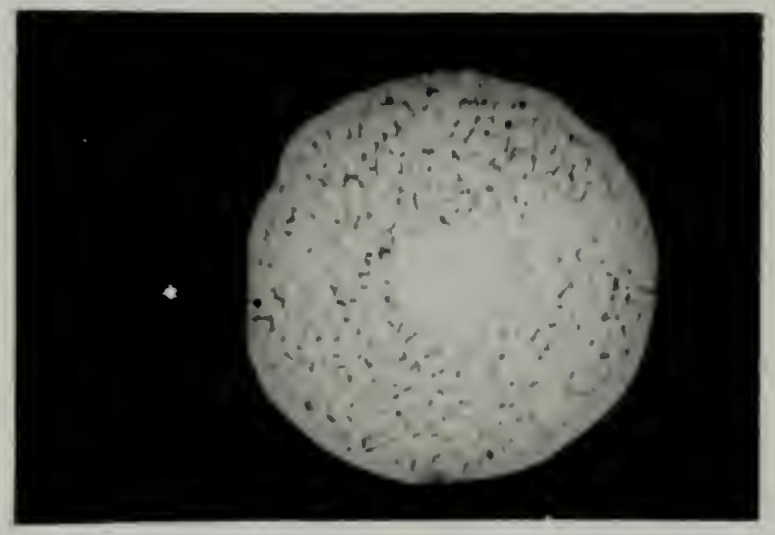

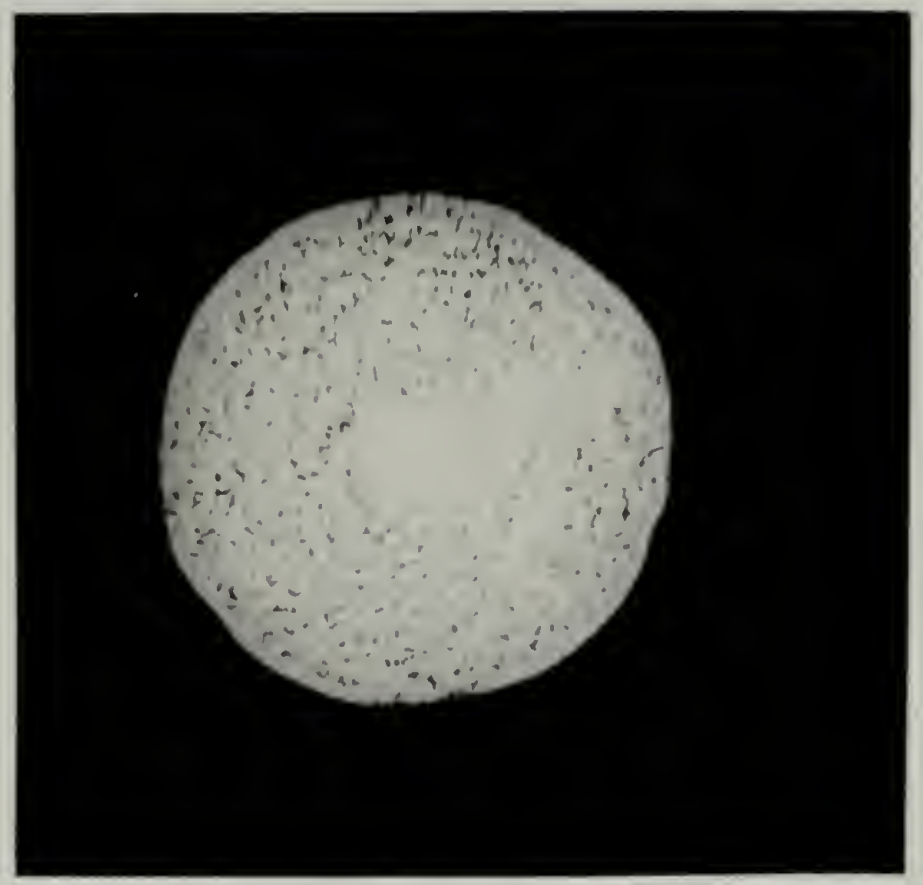

<-- 32 min. 40 -->

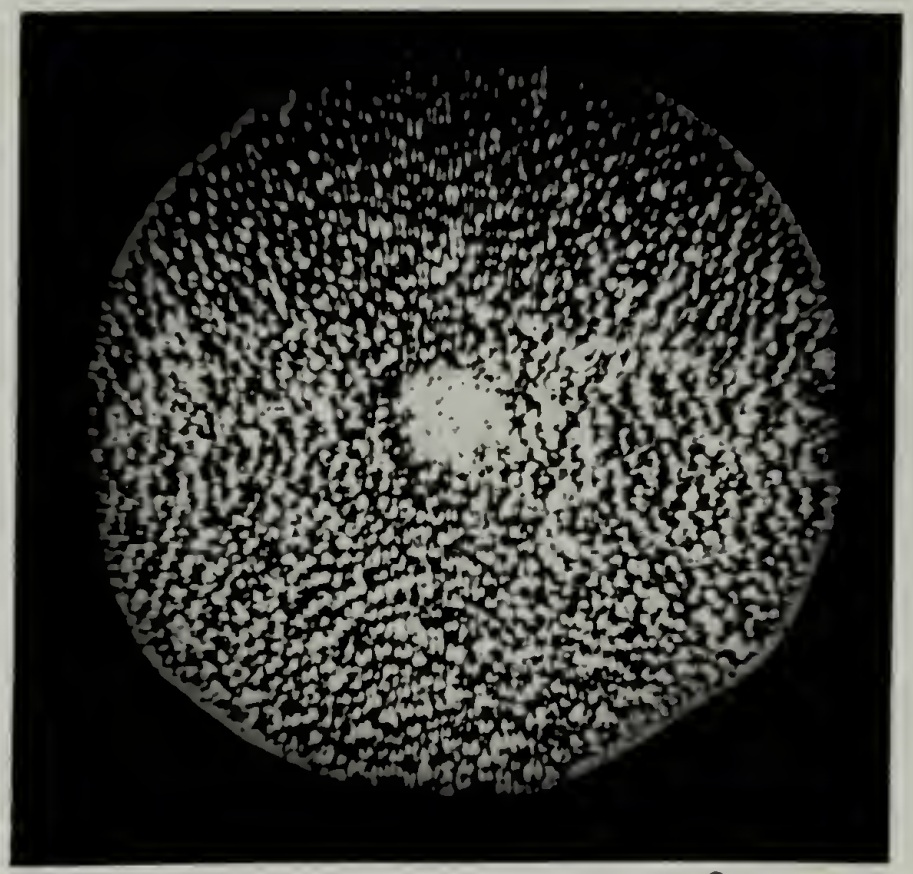

FIG. IVC-6. PHOTOMICROGRAPHS OF 1.5 MIL CHOLESTERYL MYRISTATE SAMPLE AT 80.5°C. AT DIFFERENT TIME INTERVALS.

80μ

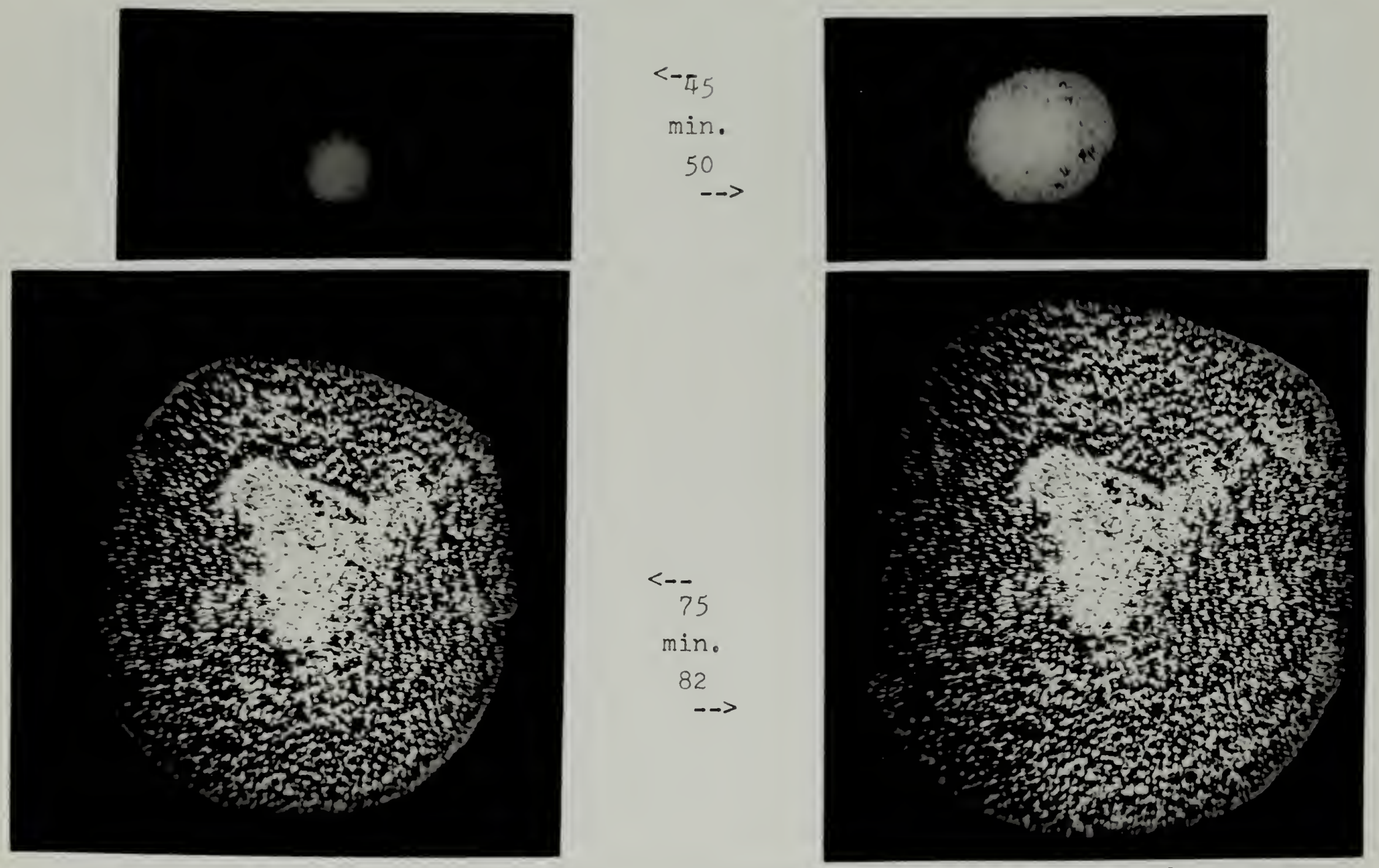

FIG. IVC-7. PHOTOMICROGRAPHS OF 1.5 MIL CHOLESTERYL MYRISTATE SAMPLE AT 81°C. AT DIFFERENT TIME INTERVALS.

FIG. IVC-8. PHOTOMICROGRAPHS OF 1.5 MIL CHOLESTERYL MYRISTATE SAMPLE AT 81.5°C. AT DIFFERENT TIME INTERVALS.

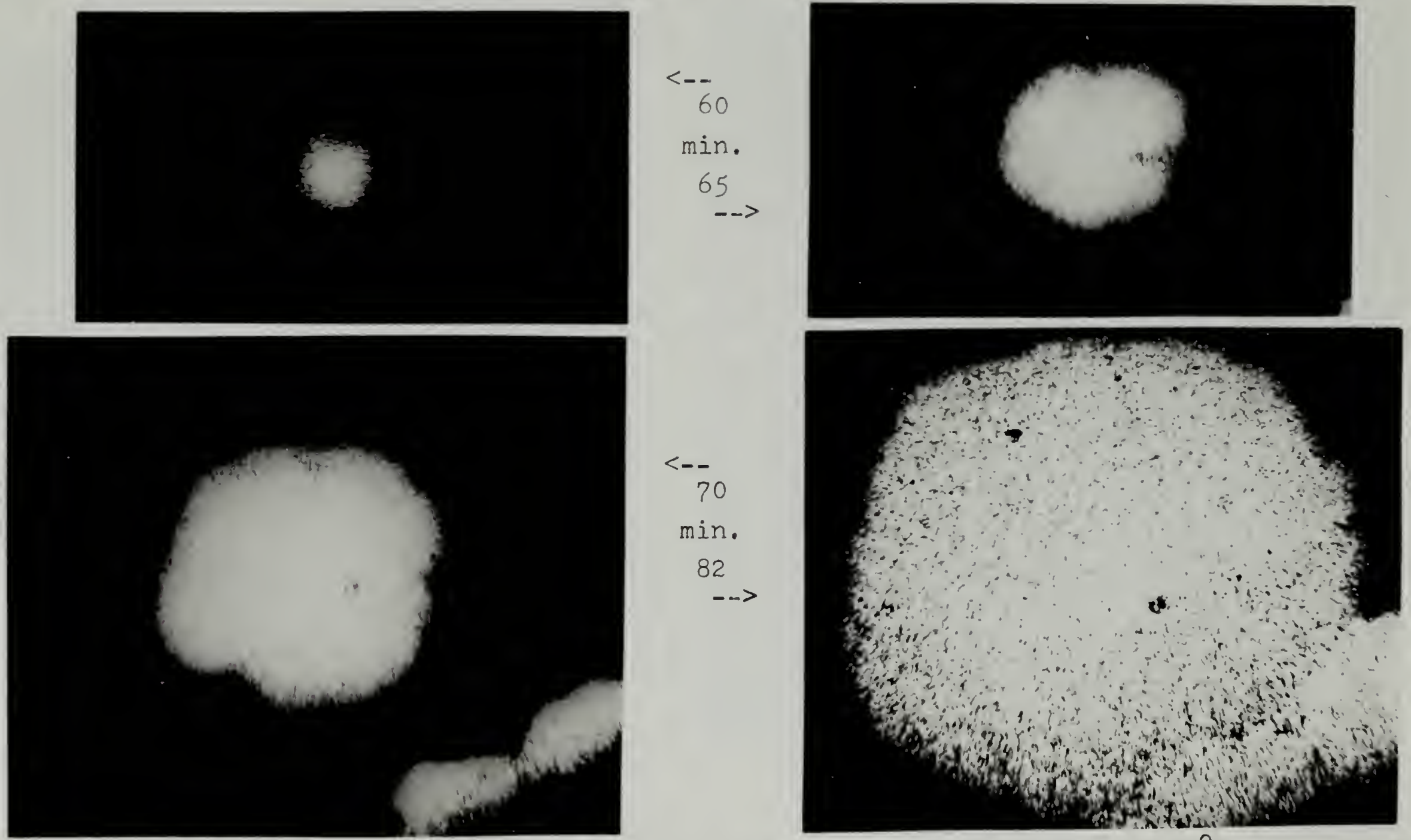

FIG. IVC-9. PHOTOMICROGRAPHS OF 1.5 MIL CHOLESTERYL MYRISTATE SAMPLE AT 82°C. AT DIFFERENT TIME INTERVALS.

80μ

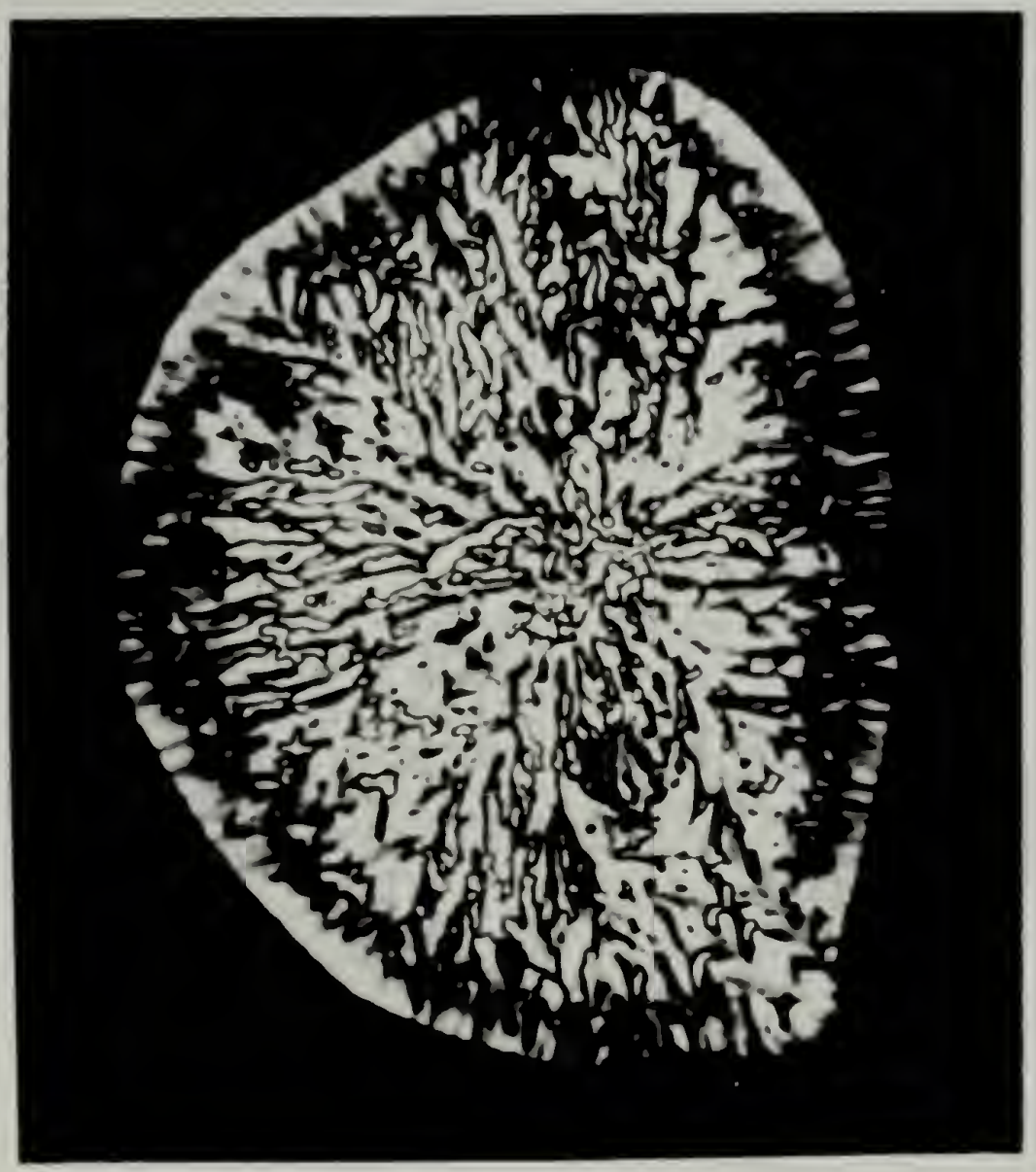

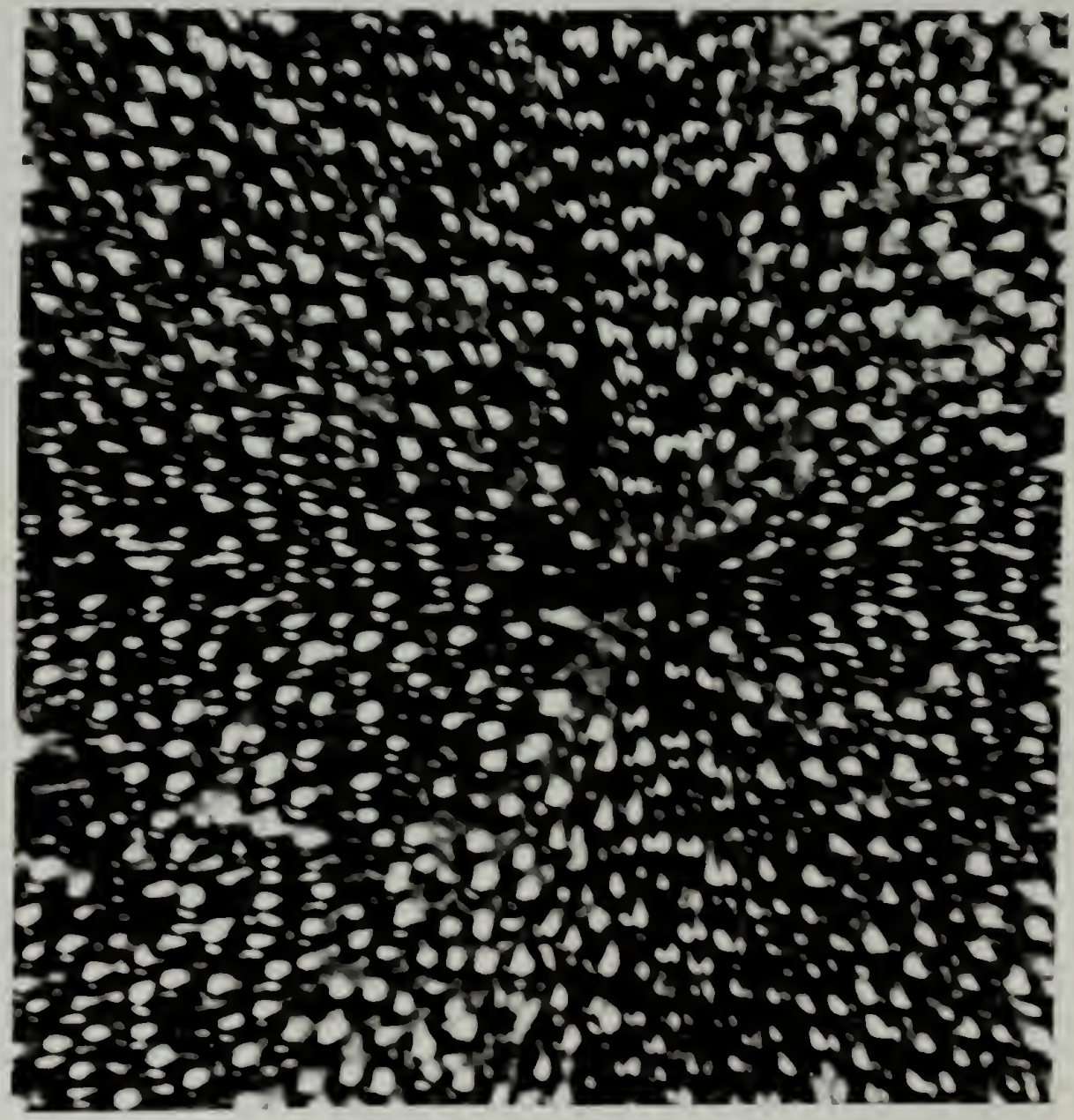

FIG. IVC-10. PHOTOMICROGRAPHS OF 1.5 MIL CHOLESTERYL MYRISTATE SAMPLE AT 82°C.(left) AND 80°C. (right).

⟵ 12.5 μ

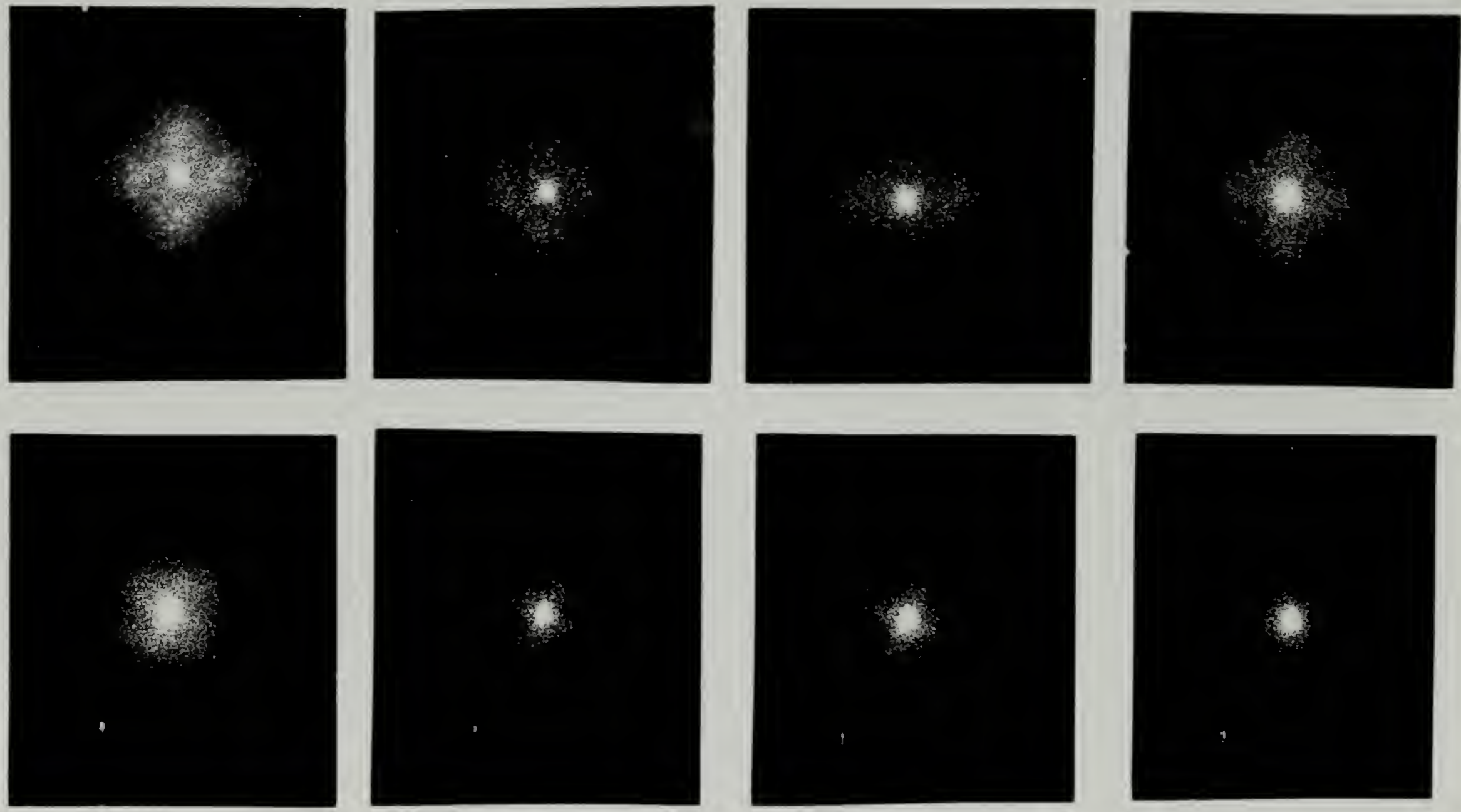

79.8°C 80.0°C 80.5°C 81°C

FIG. IVC-11. Hv (top) AND Vv (bottom) LIGHT SCATTERING PATTERNS FOR 1.5 MIL CHOLESTERY MYRISTATE SAMPLE AT DIFFERENT TEMPERATURES. —— = /°

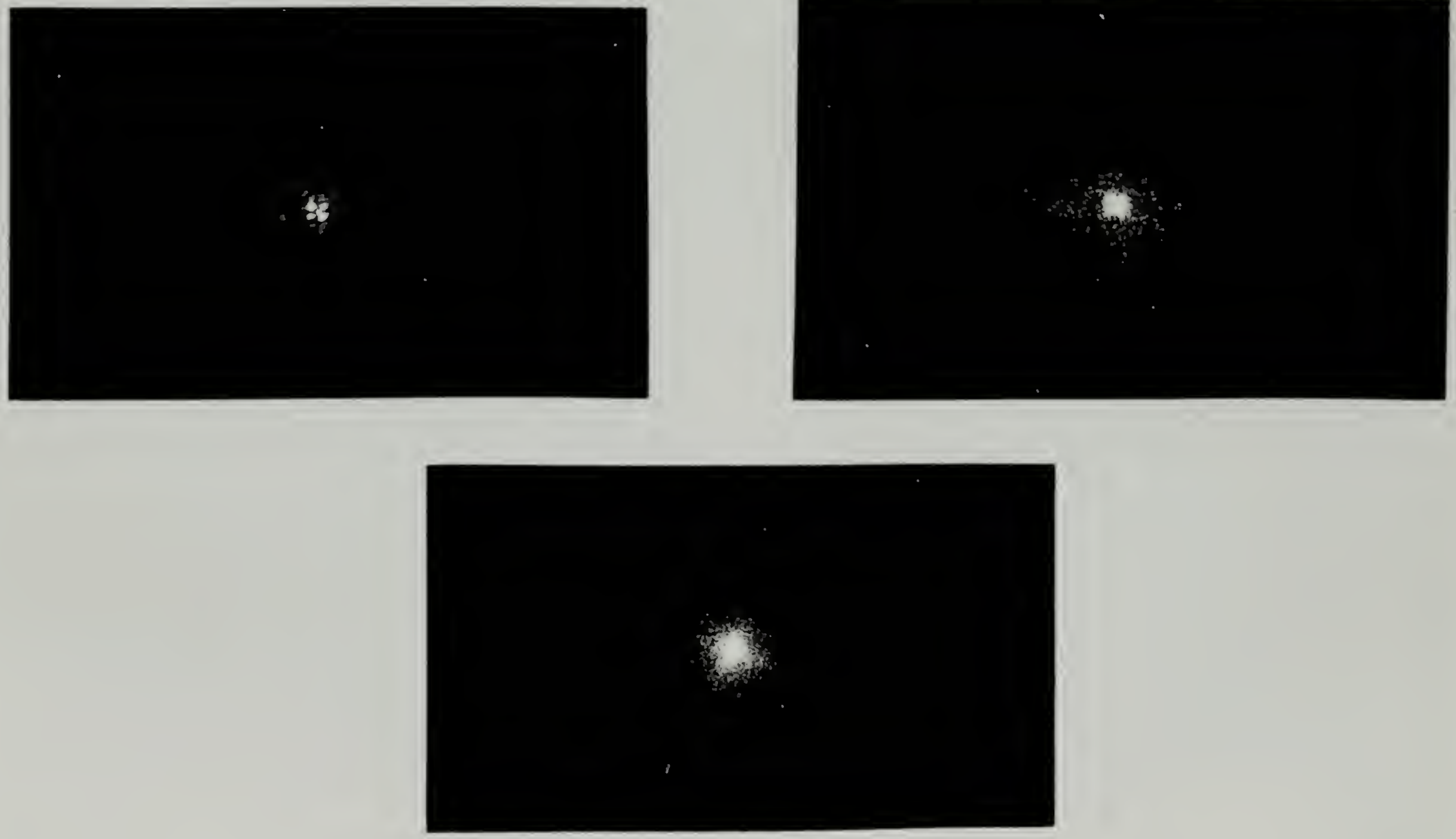

FIG. IVC-12. Hv (top) AND Vv (bottom) LIGHT SCATTERING PATTERNS FOR 1.5 MIL CHOLESTERYL MYRISTATE SAMPLE AT 82°C. (Hv on left is at 27 min., on right is at 50 min.; Vv is at 50 min.) ⌊⌋ = 1°

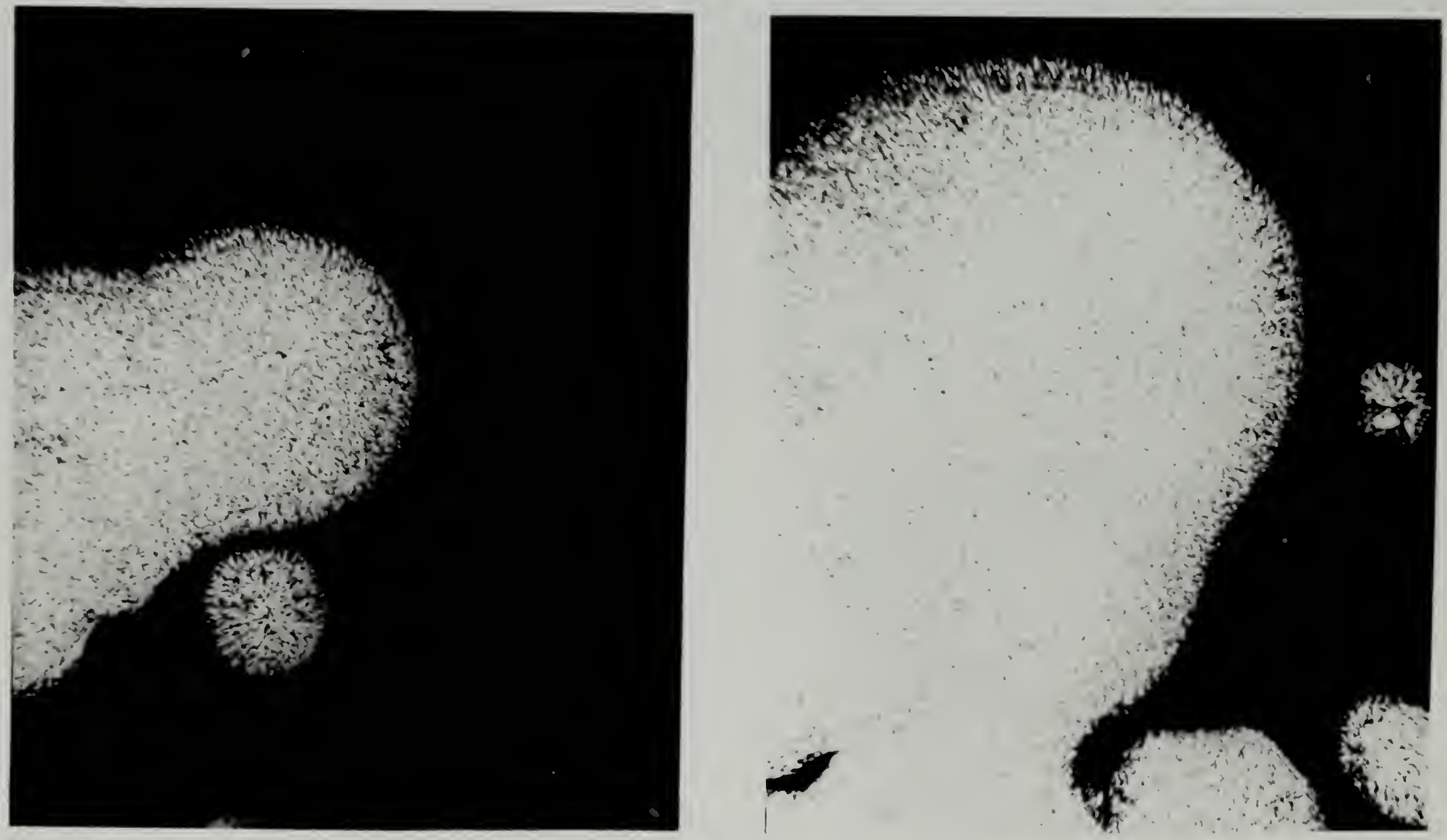

FIG. IVC-13. PHOTOMICROGRAPHS OF 3.0 MIL CHOLESTERYL MYRISTATE SAMPLE AT 81°C. AT 22 MINUTES (left) AND 30 MINUTES (right). ⟵ 80μ

5 min.

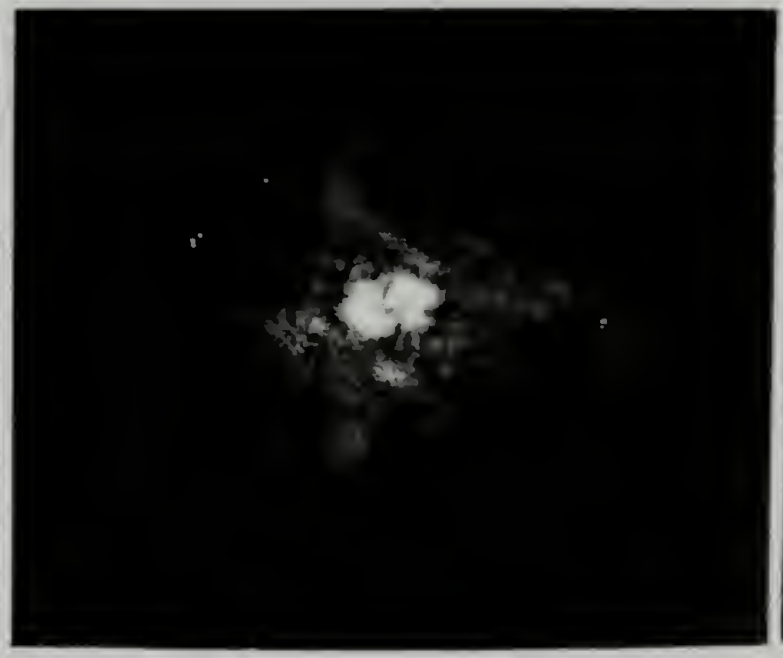

8 min.

12 min.

20 min.

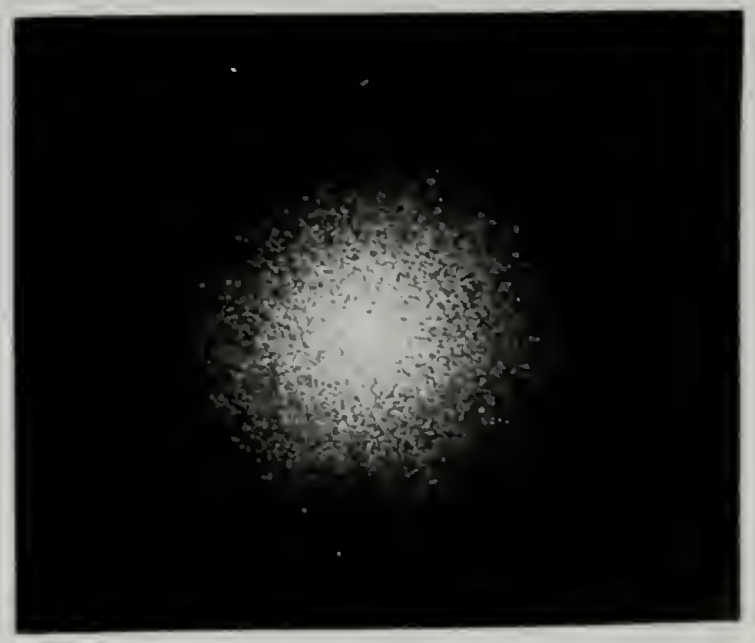

30 min.

FIG. IVC-14. Hv LIGHT SCATTERING PATTERNS FOR 3.0 MIL CHOLESTERYL MYRISTATE SAMPLE AT 81°C. AT DIFFERENT TIME INTERVALS.

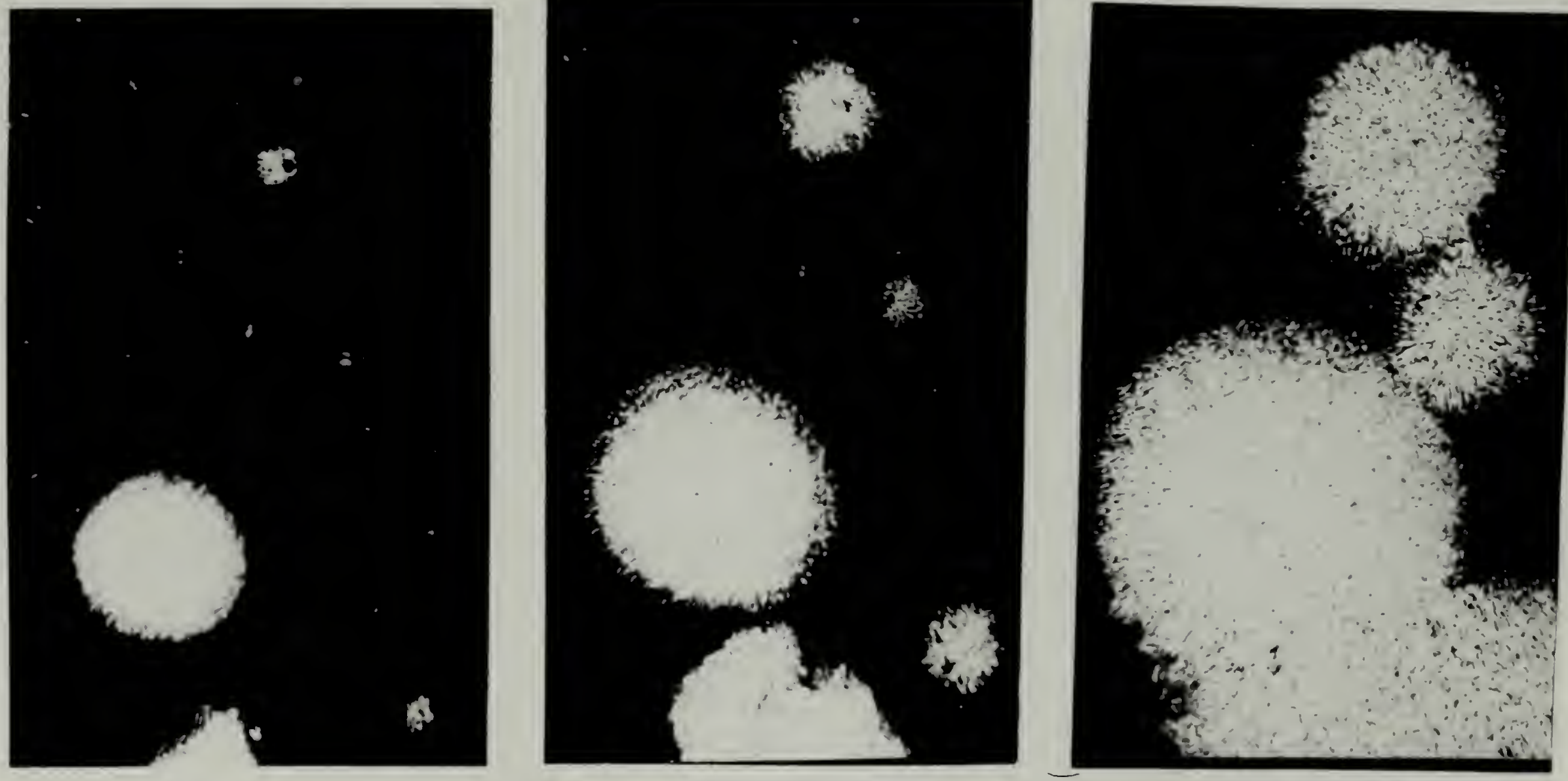

FIG. IVC-15. PHOTOMICROGRAPHS OF 3.0 MIL CHOLESTERYL MYRISTATE SAMPLE AT 82°C. AND AT 23 MINUTES (left), 30 MINUTES (center), 40 MINUTES (right). —— 80μ

FIG. IVC-16. Hv LIGHT SCATTERING PATTERNS FOR 3.0 MIL CHOLESTERYL MYRISTATE SAMPLE AT 82°C. AT 17 MINUTES (left), 23 MINUTES (center), 40 MINUTES (right).

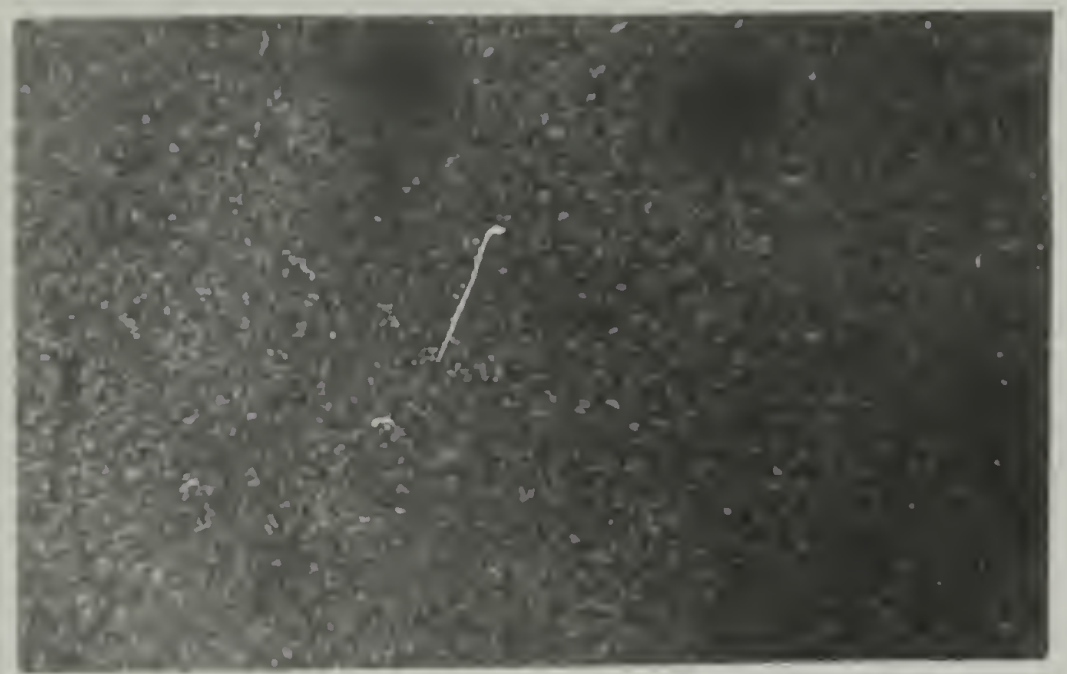

<-- 5 min. 23 -->

<-- 28 min. 35 -->

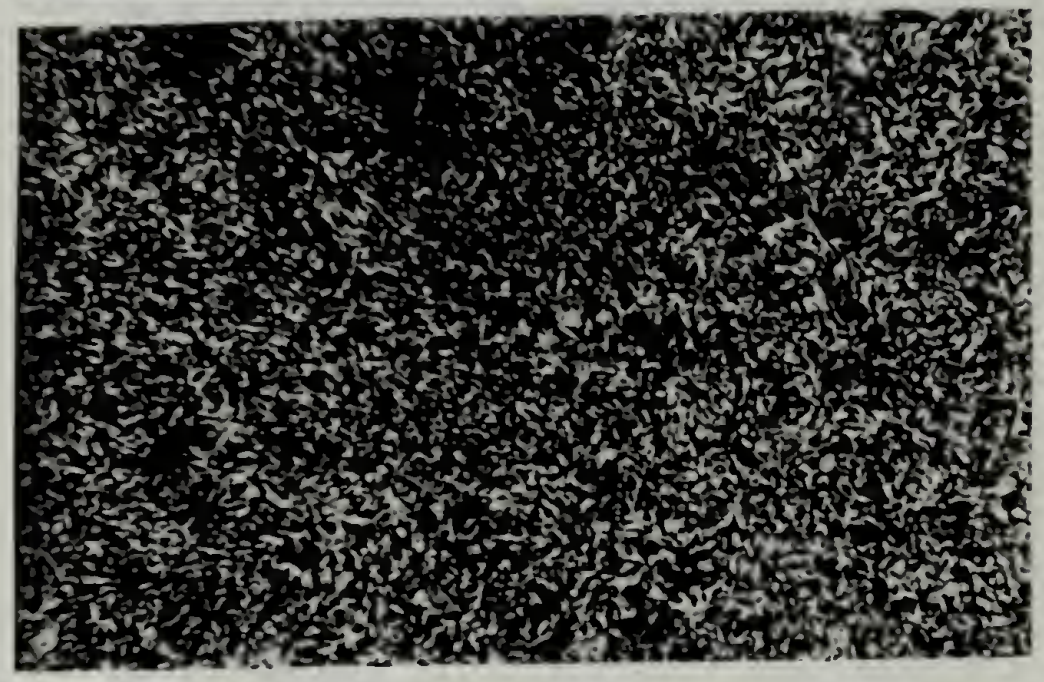

FIG. IVC-17. PHOTOMICROGRAPHS OF 6.0 MIL CHOLESTERYL MYRISTATE SAMPLE AT 81.5°C. AT DIFFERENT TIME INTERVALS.

80μ

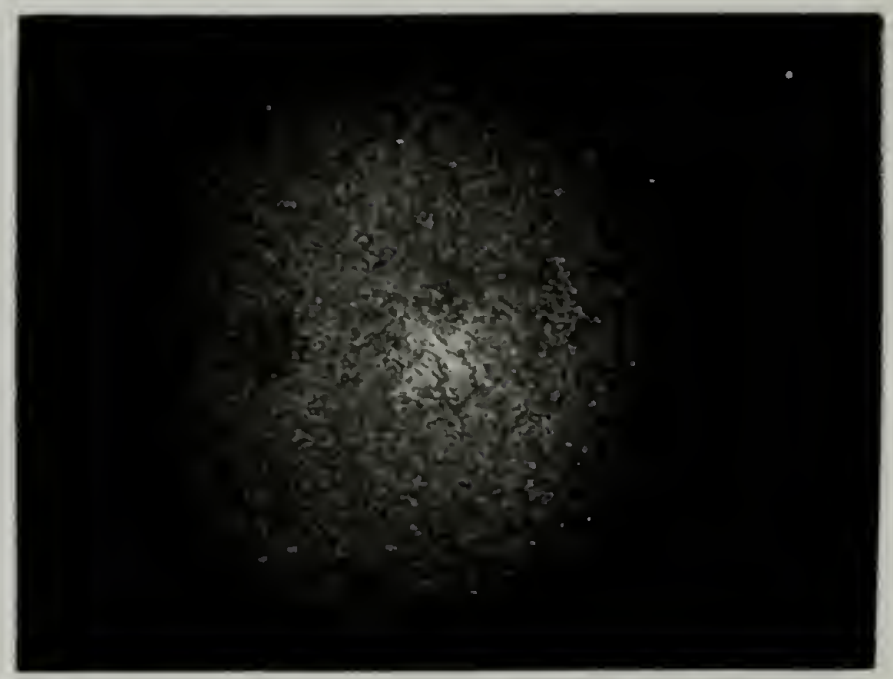

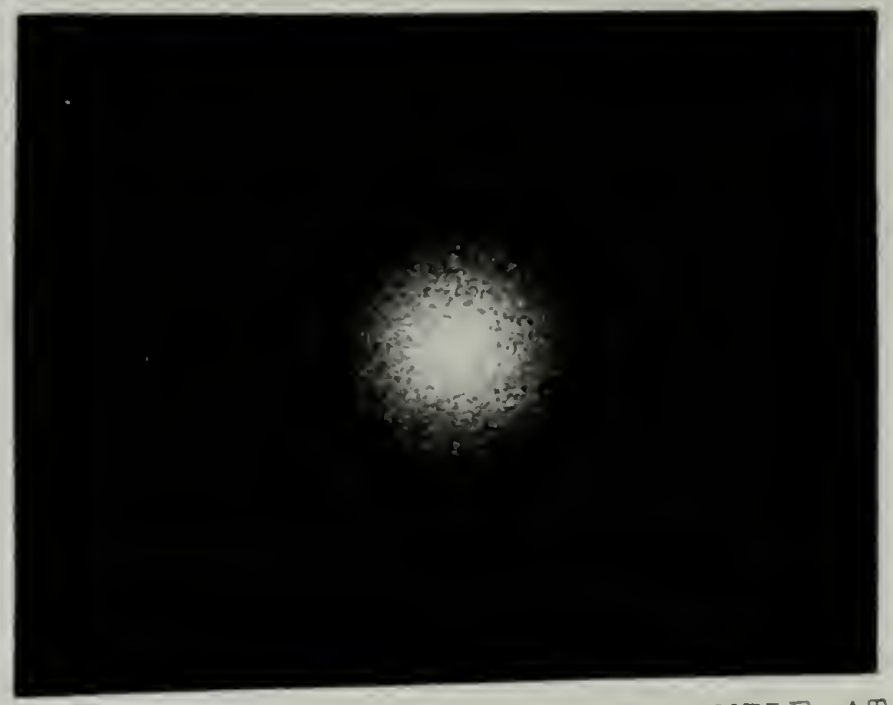

FIG. IVC-18. Hv LIGHT SCATTERING PATTERNS FOR 6.0 MIL CHOLESTERYL MYRISTATE SAMPLE AT 81.5°C. AT DIFFERENT TIME INTERVALS.

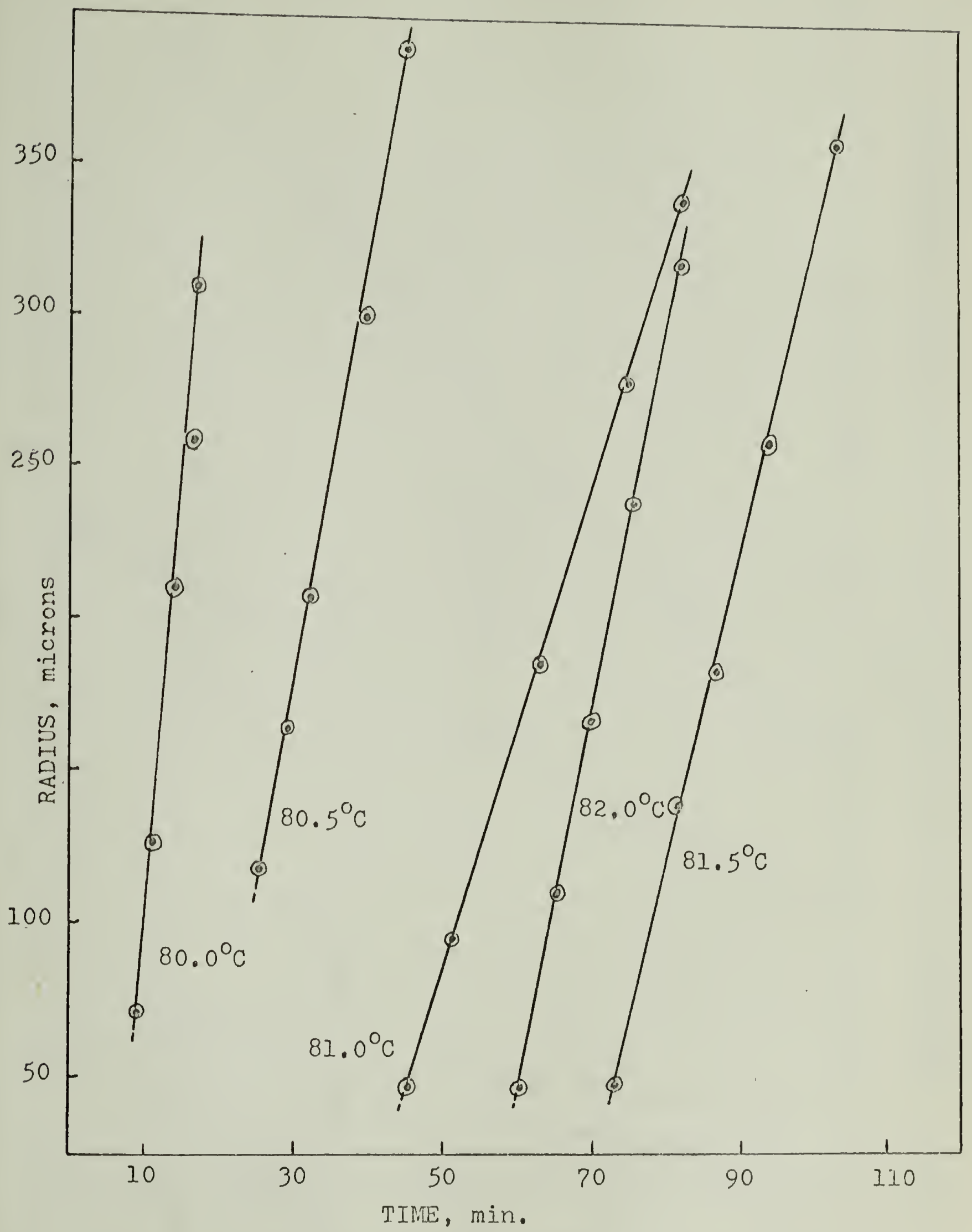

FIG. IVD-1. DEPENDENCE OF RADIAL GROWTH ON TIME AT VARIOUS GROWTH TEMPERATURES FOR 1.5 MIL CHOLESTERYL MYRISTATE SAMPLE

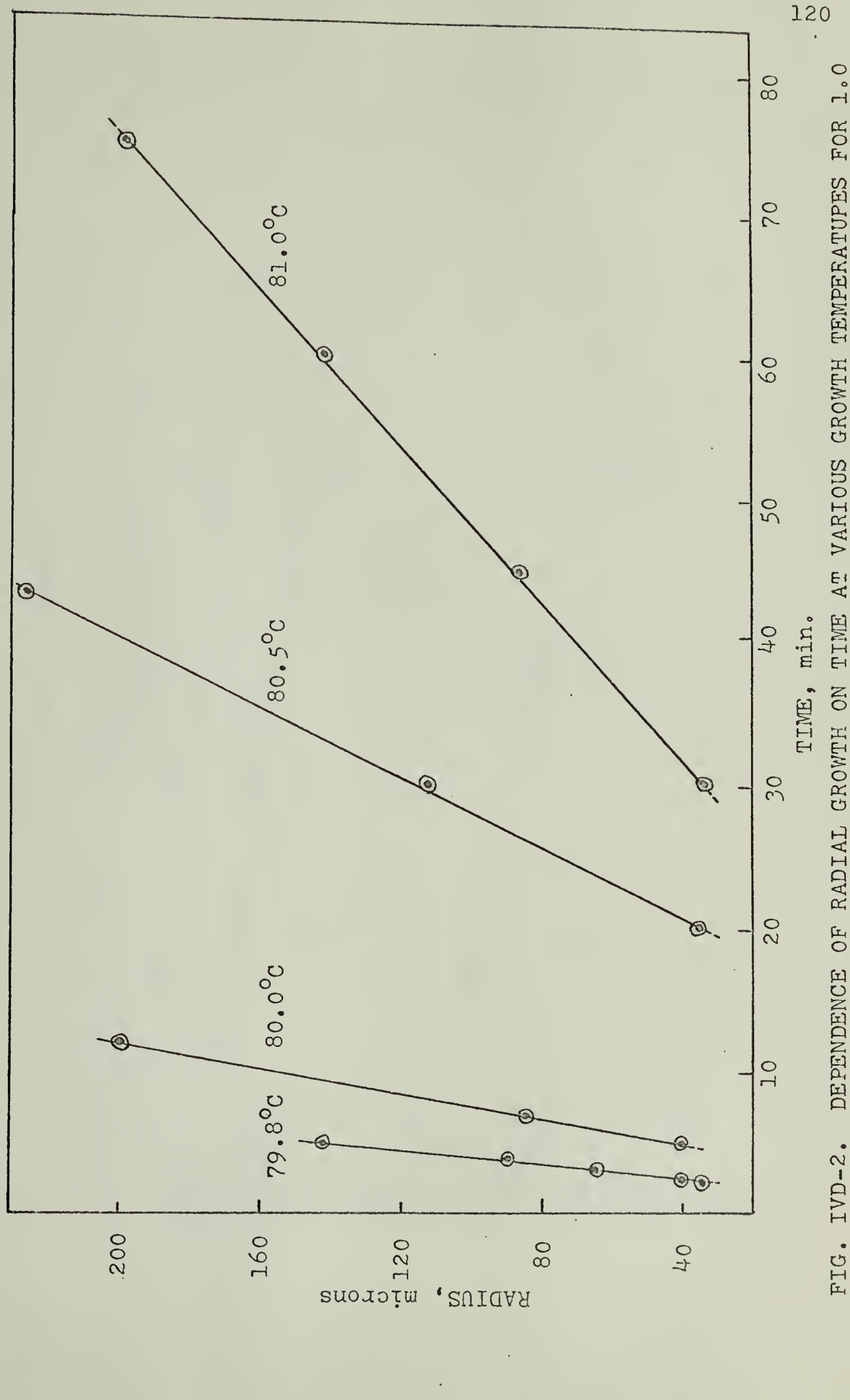

FIG. IVD-2. DEPENDENCE OF RADIAL GROWTH ON TIME AT VARIOUS GROWTH TEMPERATUPES FOR 1.0 MIL CHOLESTERYL MYRISTATE SAMPLE.

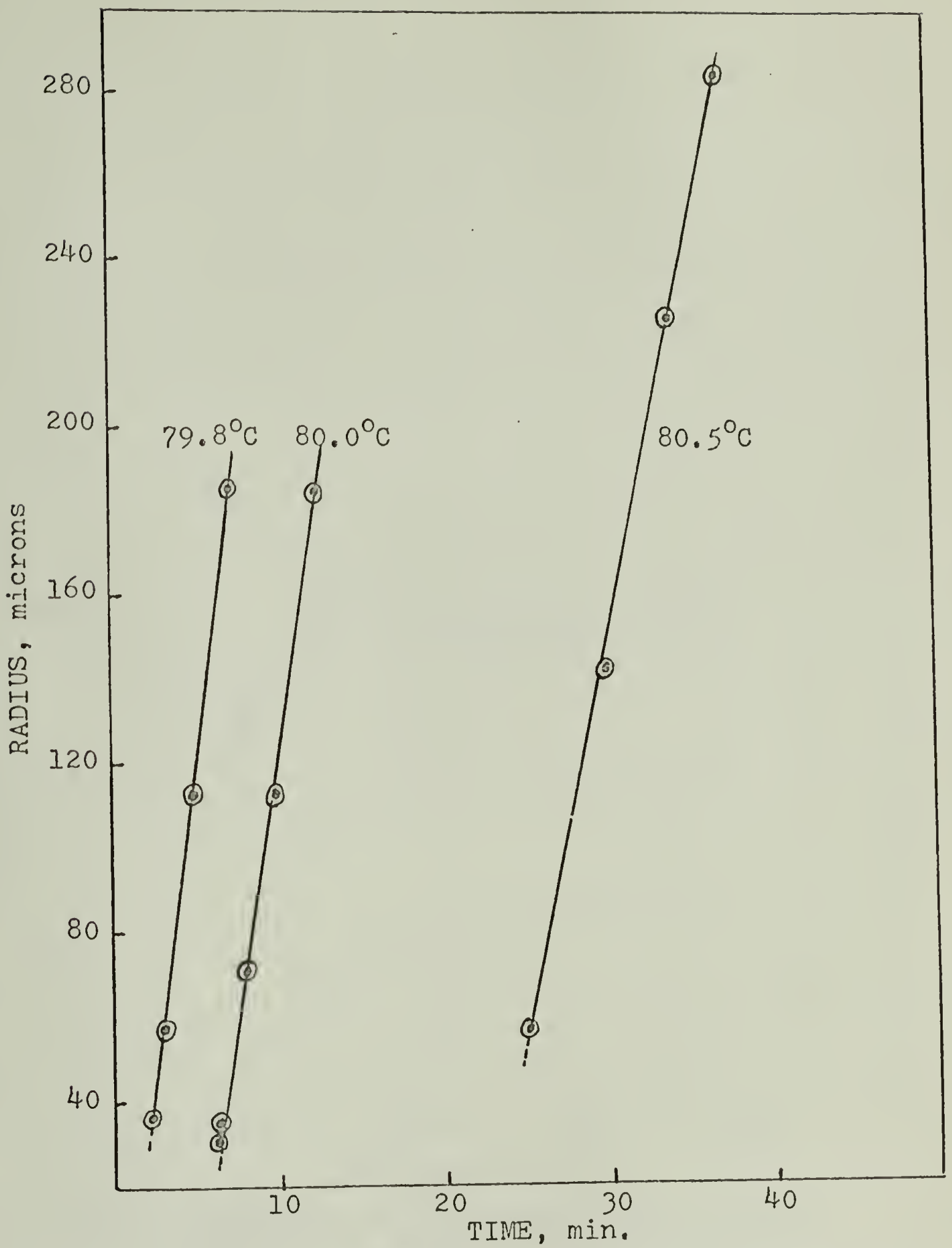

FIG. IVD-3. DEPENDENCE OF RADIAL GROWTH ON TIME AT VARIOUS TEMPERATURES FOR 3.0 MIL CHOLESTERYL MYRISTATE SAMPLE.

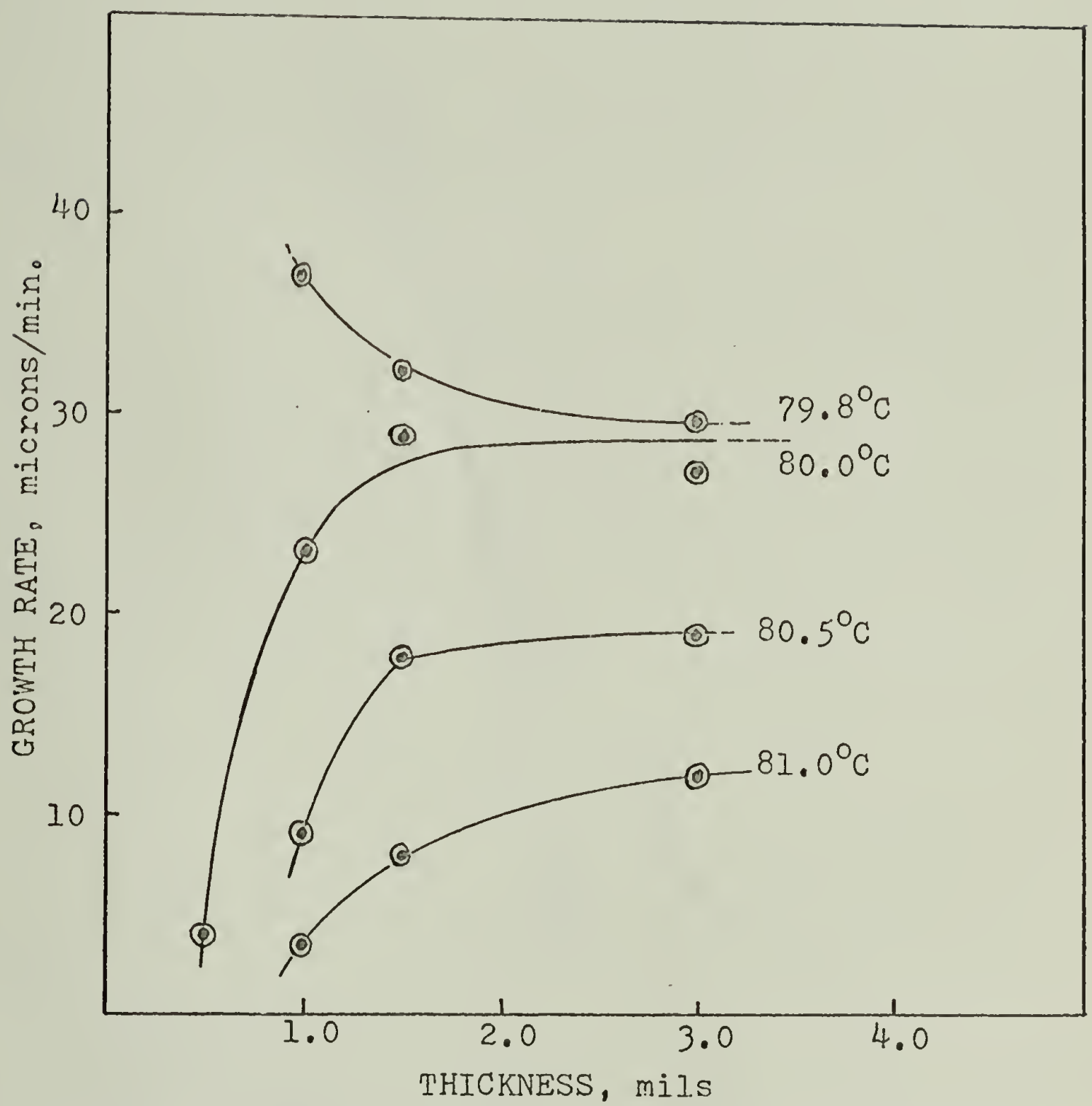

FIG. IVD-4. DEPENDENCE OF THE GROWTH RATE ON SAMPLE THICKNESS AT VARIOUS TEMPERATURES.

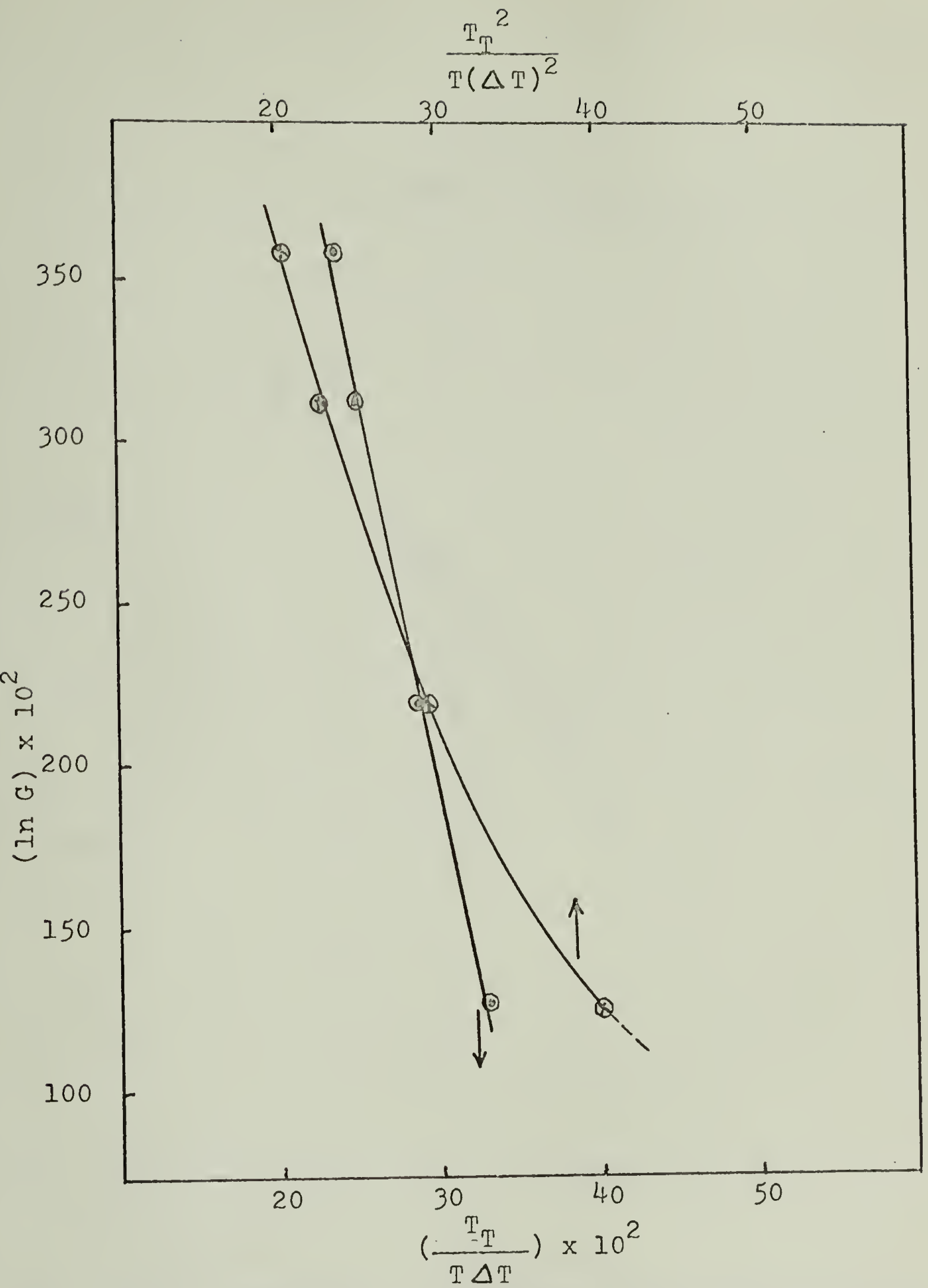

FIG. IVD-5. TEMPERATURE DEPENDENCE OF THE GROWTH RATE OF CHOLESTERYL MYRISTATE IN THE CHOLESTERIC PHASE FOR 1 MIL SAMPLE.

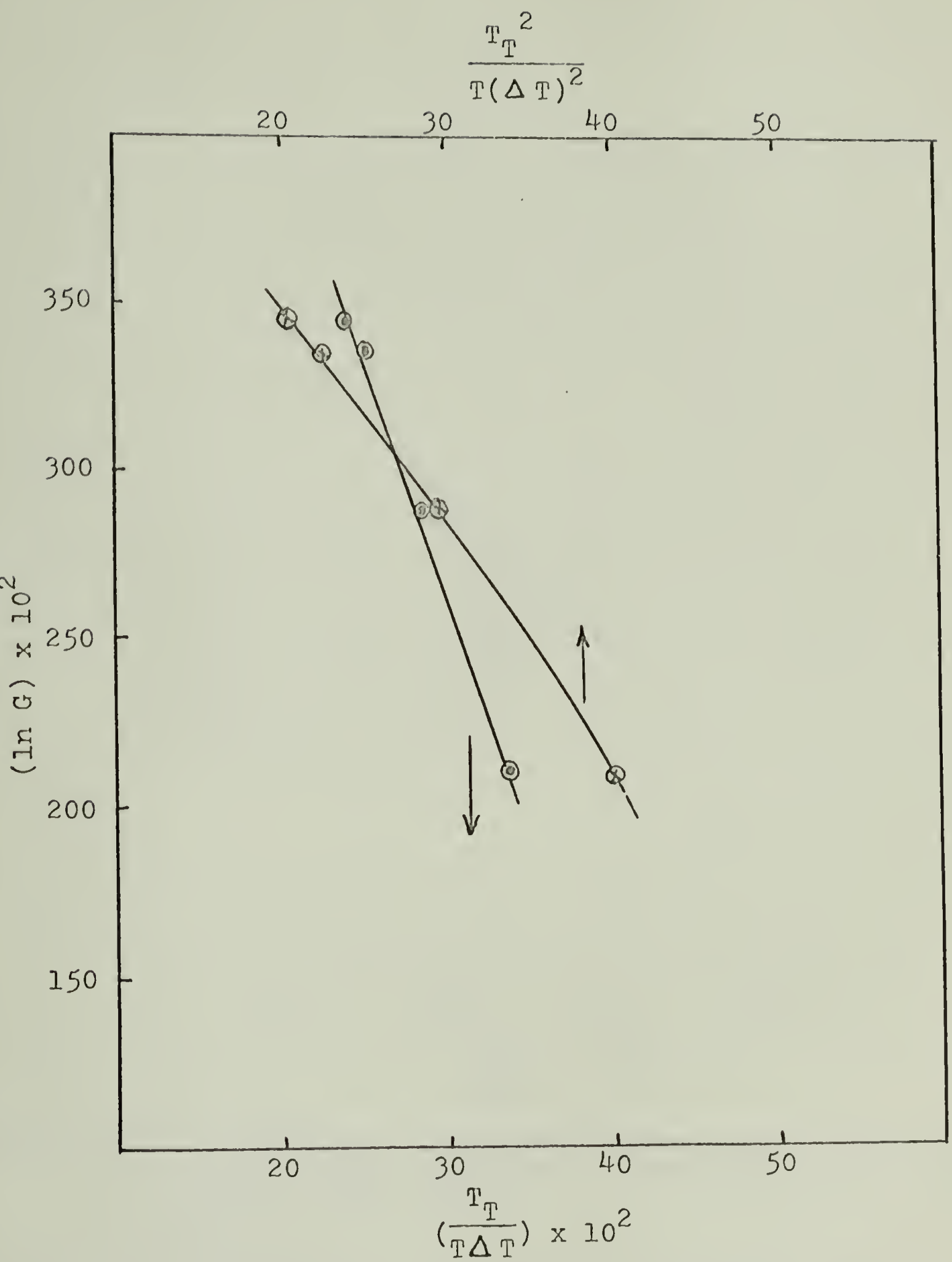

FIG. IVD-6. TEMPERATURE DEPENDENCE OF THE GROWTH RATE OF CHOLESTERYL MYRISTATE IN THE CHOLESTERIC PHASE FOR 1.5 MIL SAMPLE.

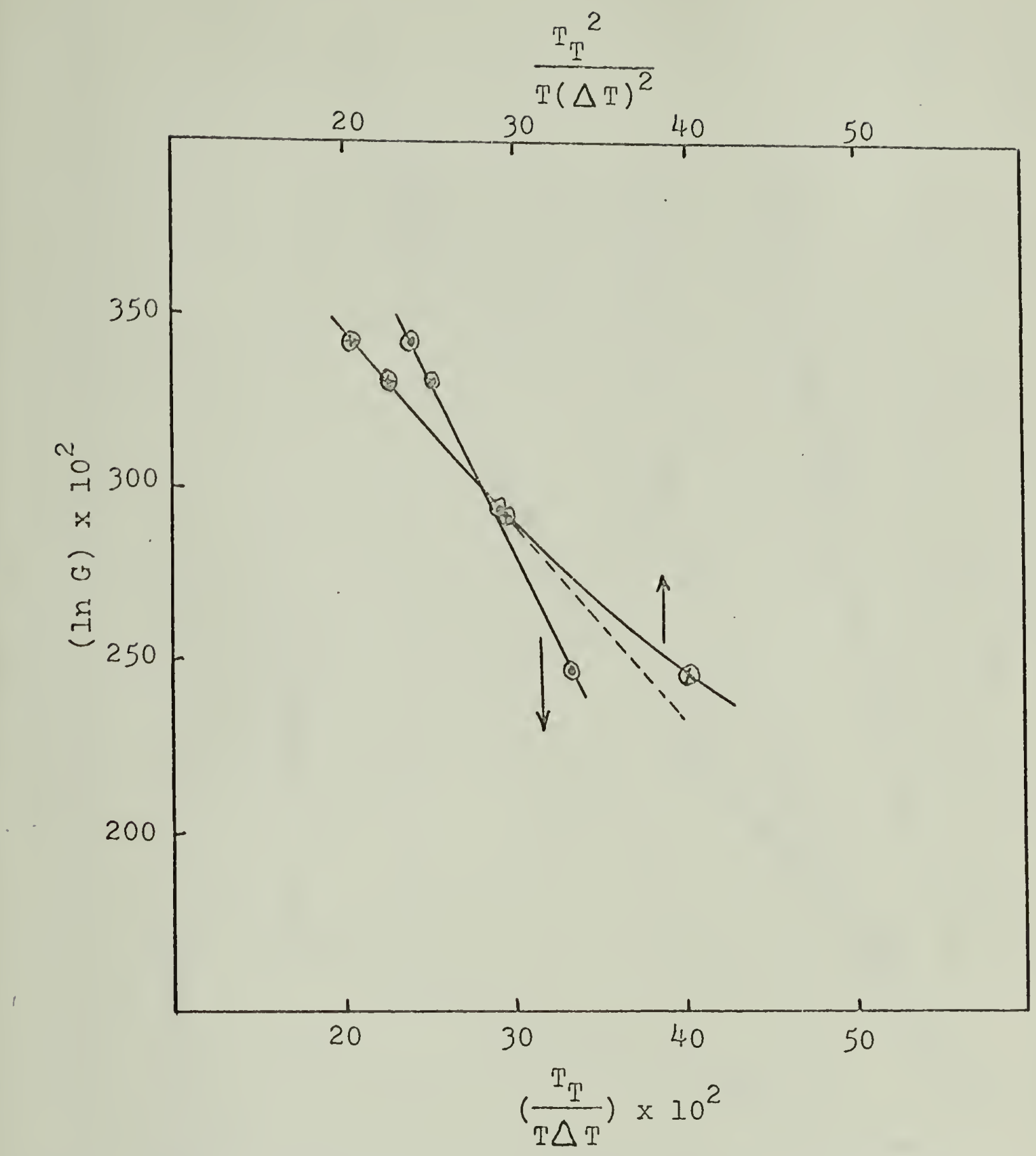

FIG. IVD-7. TEMPERATURE DEPENDENCE OF THE GROWTH RATE OF CHOLESTERYL MYRISTATE IN THE CHOLESTERIC PHASE FOR 3.0 MIL SAMPLE.

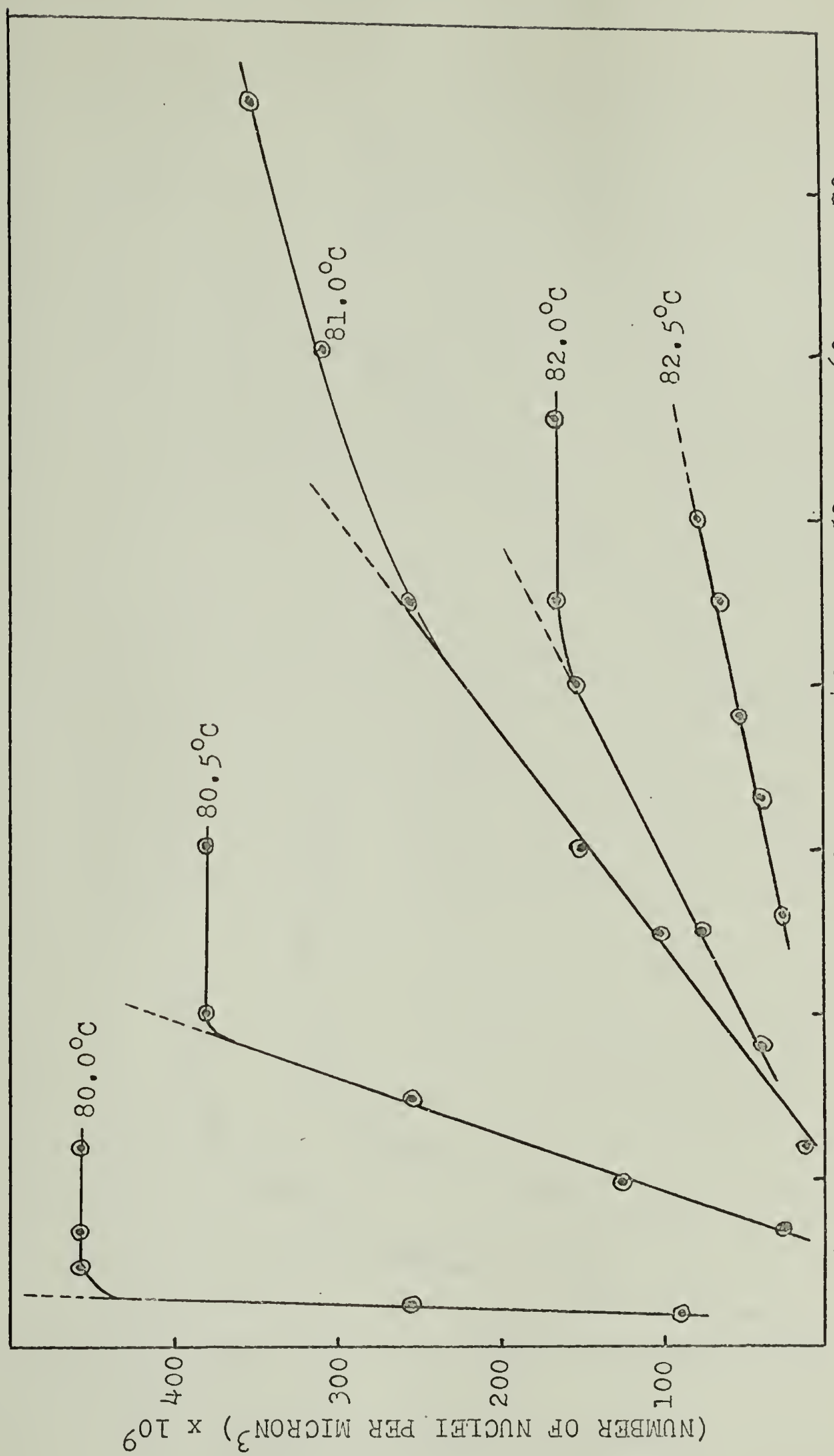

FIG. IVD-8. NUMBER OF NUCLEI PER UNIT VOLUME AS A FUNCTION OF TIME AT DIFFERENT TEMPERATURES FOR 1.0 MIL CHOLESTERYL MYRISTATE SAMPLE.

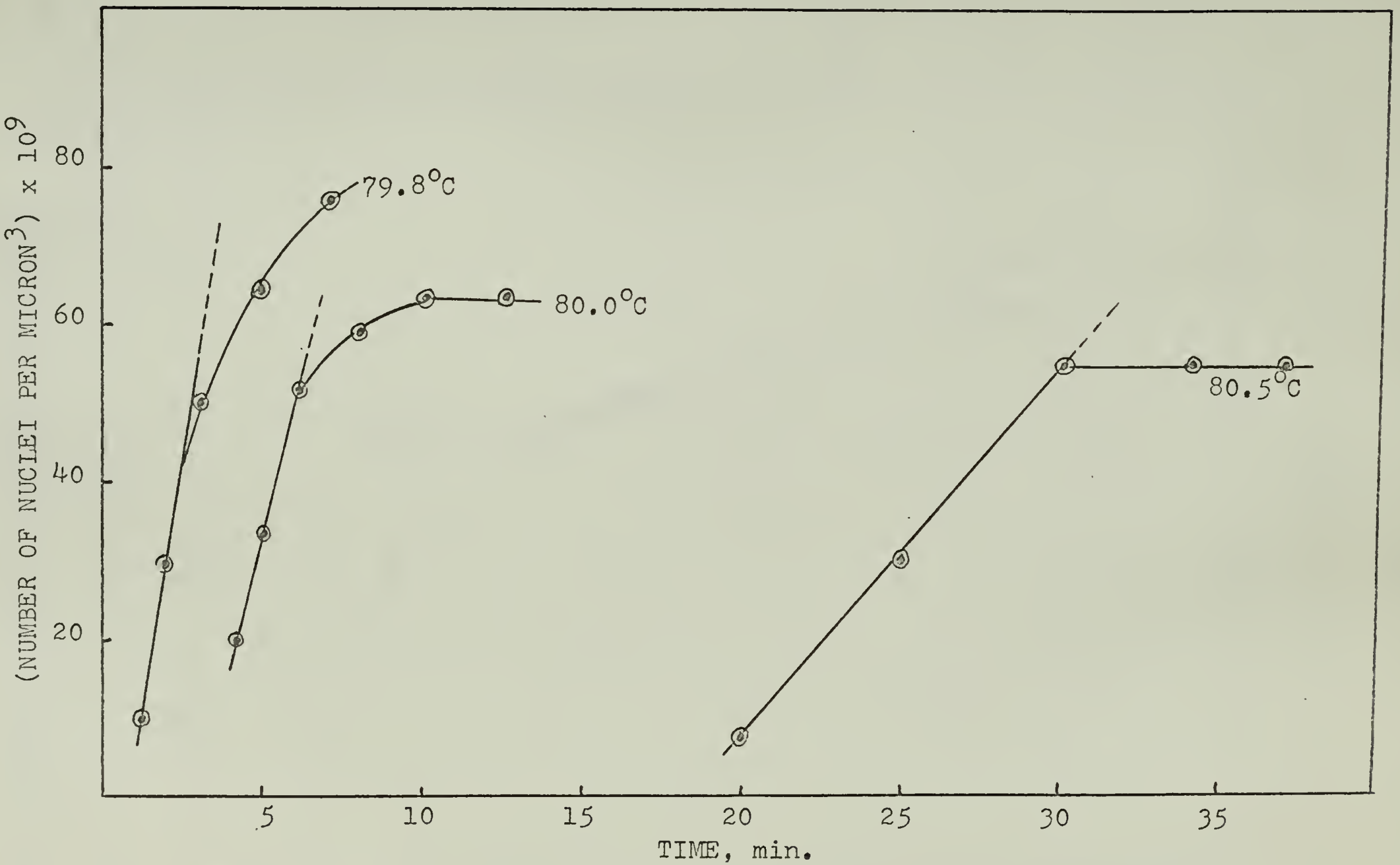

FIG. IVD-9. NUMBER OF NUCLEI PER UNIT VOLUME AS A FUNCTION OF TIME AT DIFFERENT TEMPERATURES FOR 3.0 MIL CHOLESTERYL MYRISTATE SAMPLE.

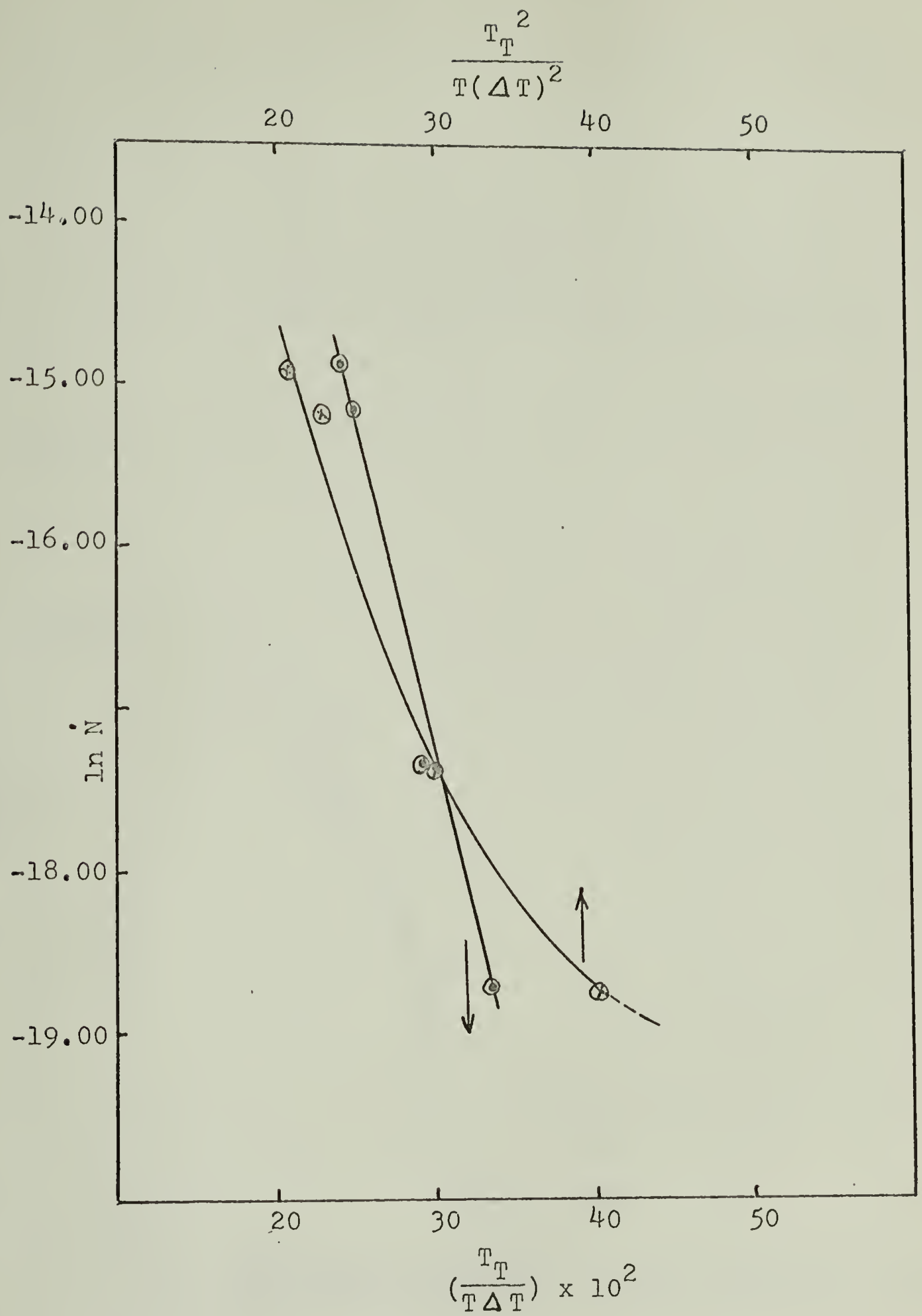

FIG. IVD-10. TEMPERATURE DEPENDENCE OF THE NUCLEATION RATE OF CHOLESTERYL MYRISTATE IN THE CHOLESTERIC PHASE FOR 1.0 MIL SAMPLE.

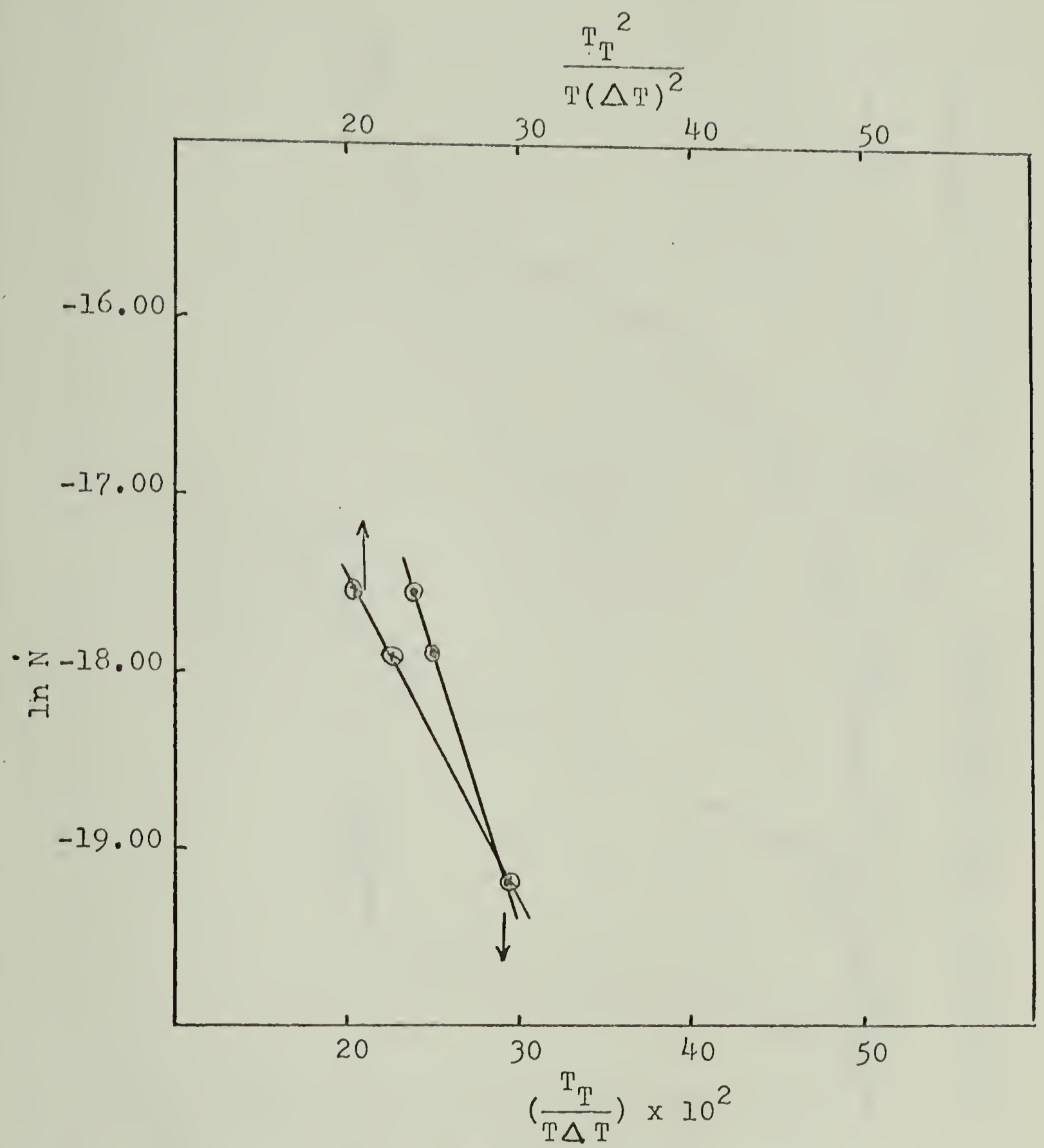

FIG. IVD-11. TEMPERATURE DEPENDENCE OF THE NUCLEATION RATE OF CHOLESTERYL MYRISTATE IN THE CHOLESTERIC PHASE FOR 3.0 MIL SAMPLE.

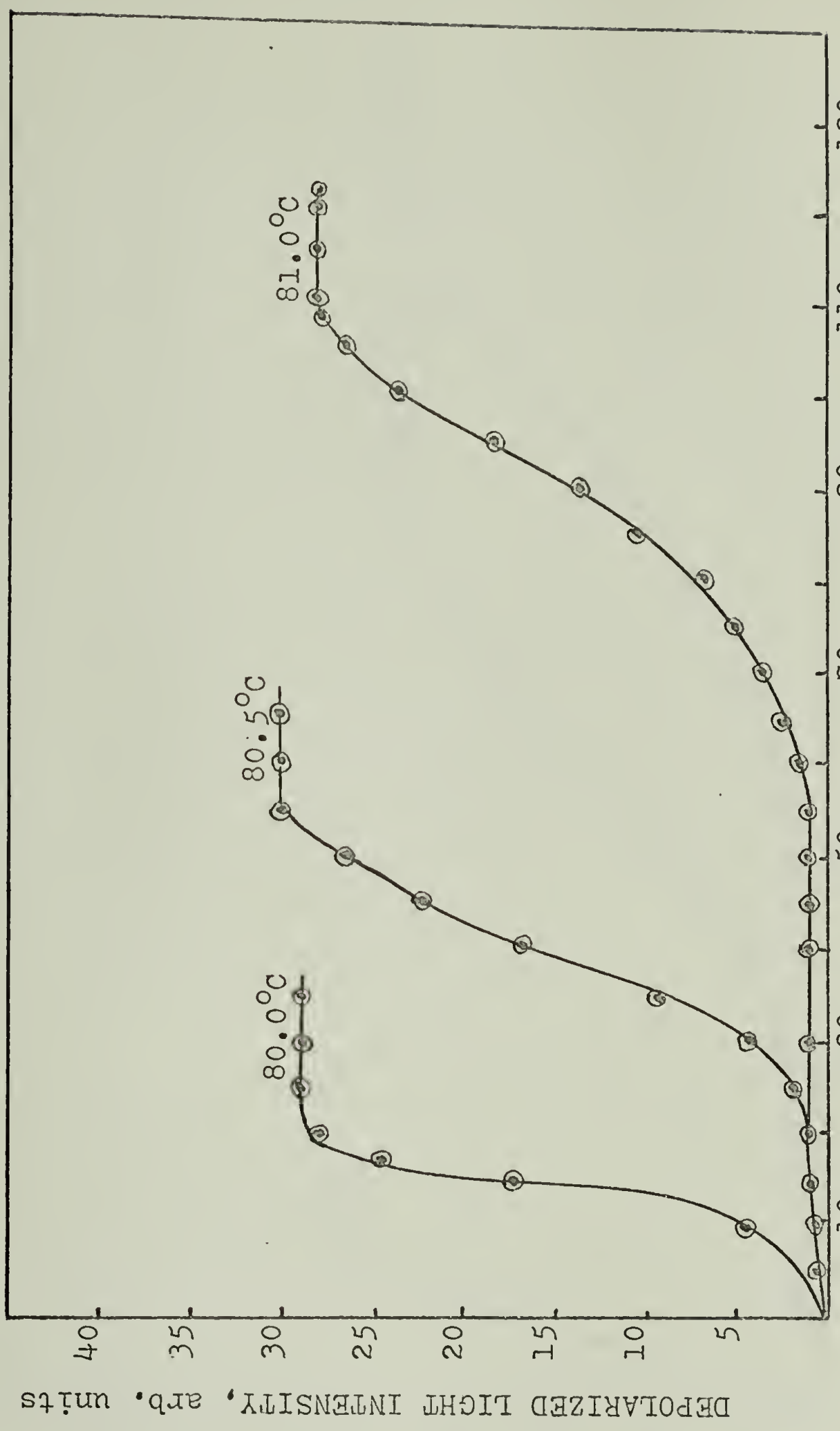

FIG. IVE-1. DEPOLARIZED LIHGT INTENSITY vs. TIME FOR VARIOUS TEMPERATURES OF 3.0 MIL CHOLESTERYL MYRISTATE SAMPLE.

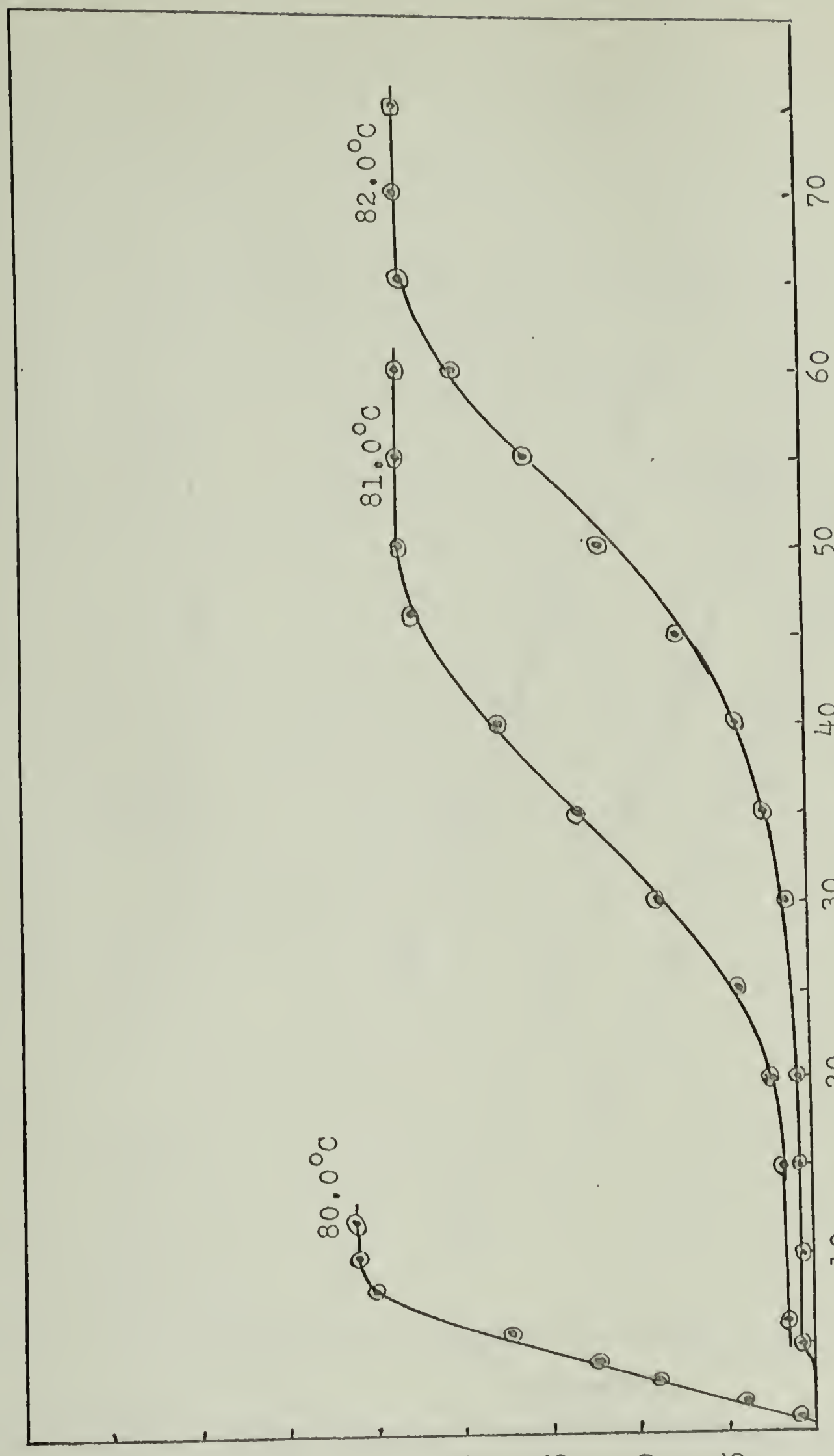

FIG. IVE-2. DEPOLARIZED LIGHT INTENSITY vs. TIME FOR VARIOUS TEMPERATURES OF 6.0 MIL CHOLESTERYL MYRISTATE SAMPLE.

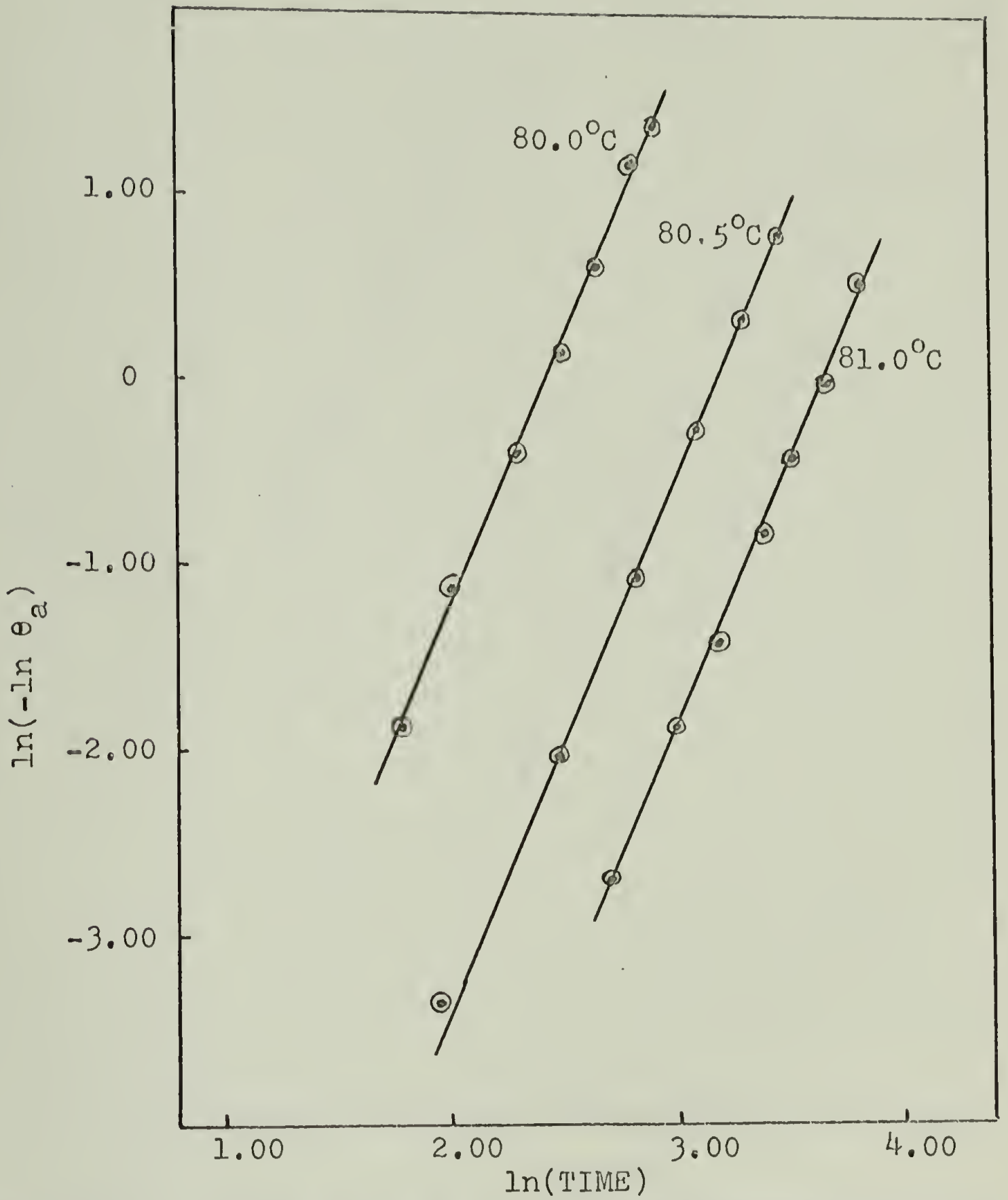

FIG. IVE-3. AVRAMI PLOT OF 3.0 MIL CHOLESTERYL MYRISTATE SAMPLE AT VARIOUS TEMPERATURES.

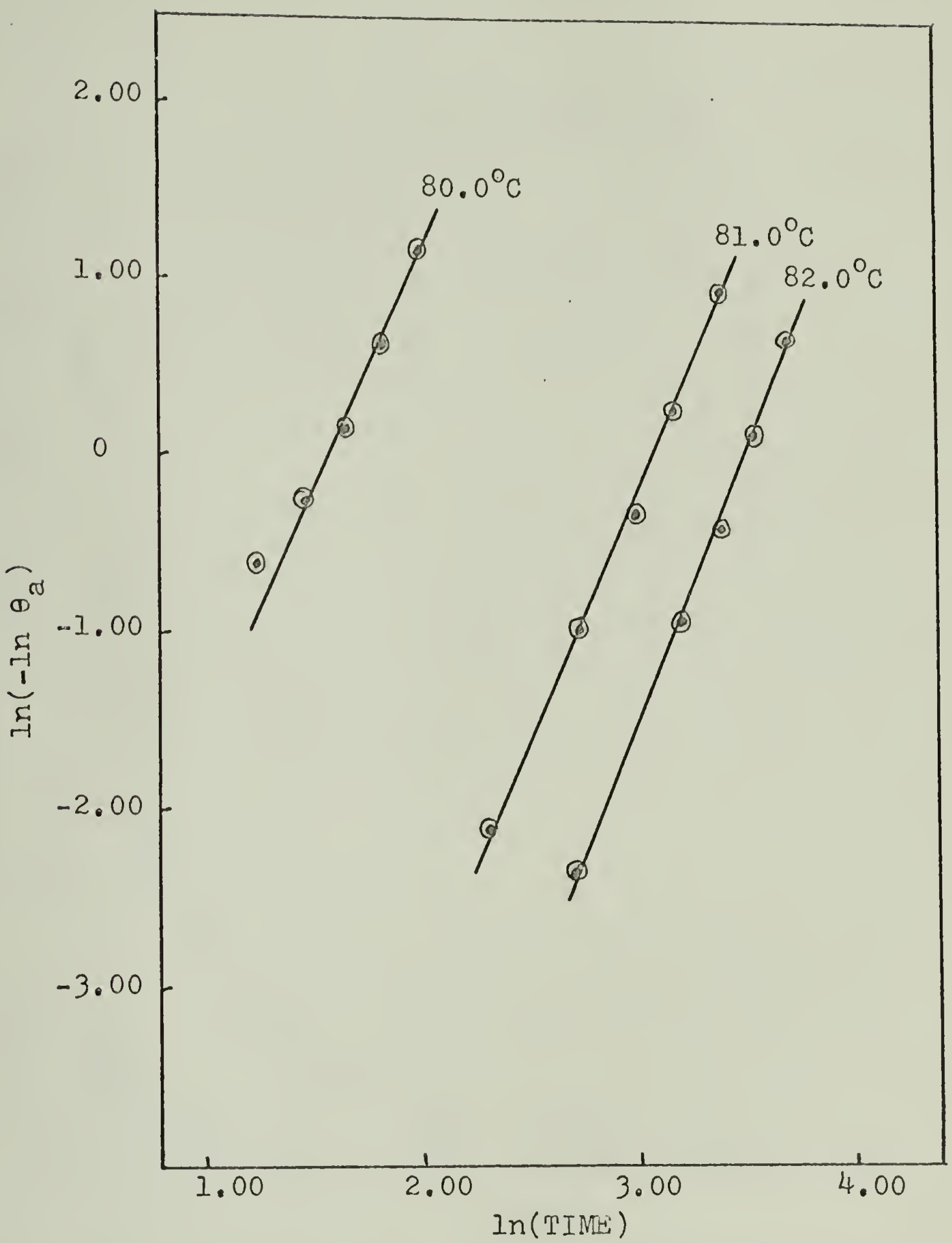

FIG. IVE-4. AVRAMI PLOT OF 6.0 MIL CHOLESTERYL MYRISTATE SAMPLE AT VARIOUS TEMPERATURES.

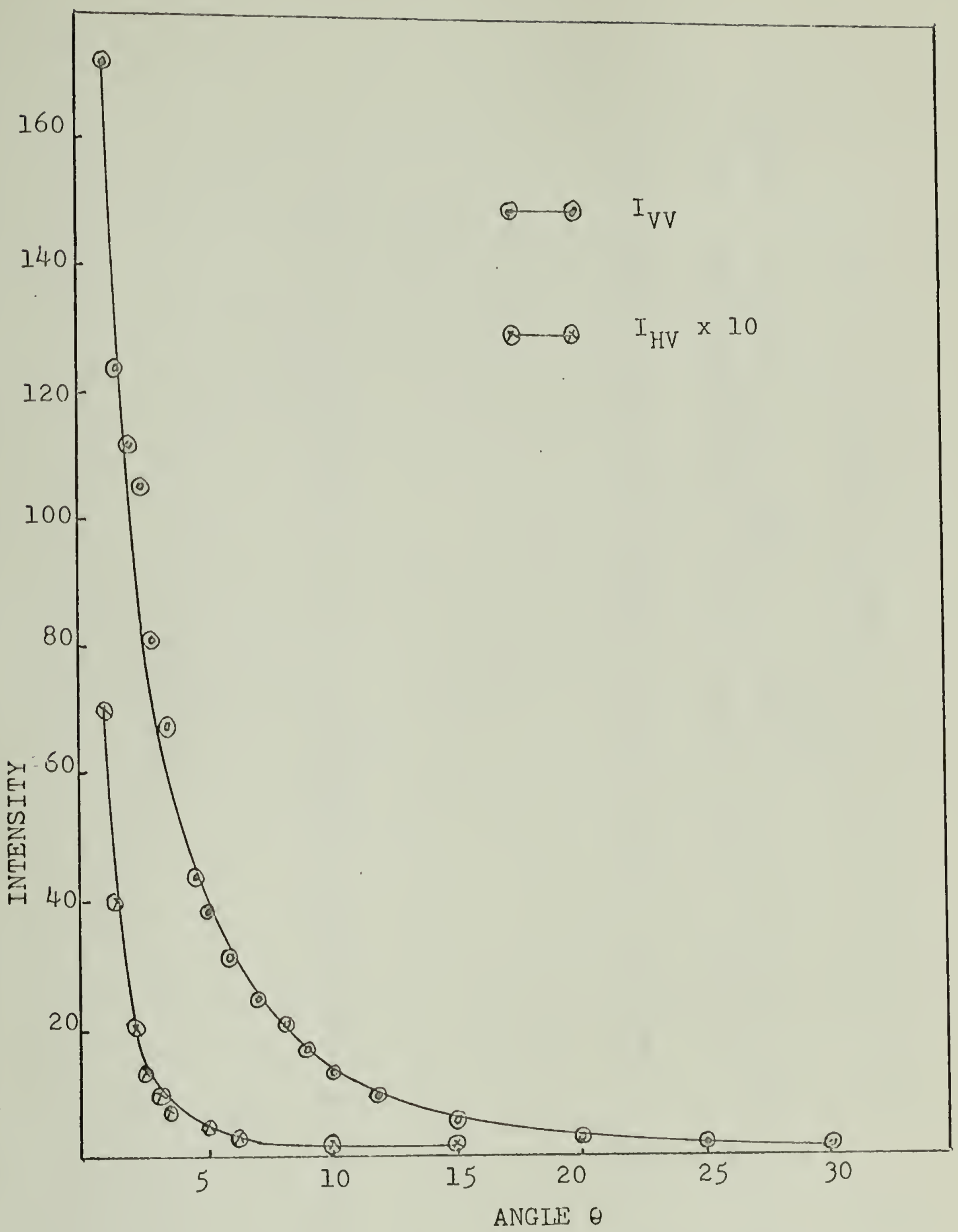

FIG. IVF-1. INTENSITY VS. ANGLE θ FOR CHOLESTERYL MYRISTATE AT 82°C

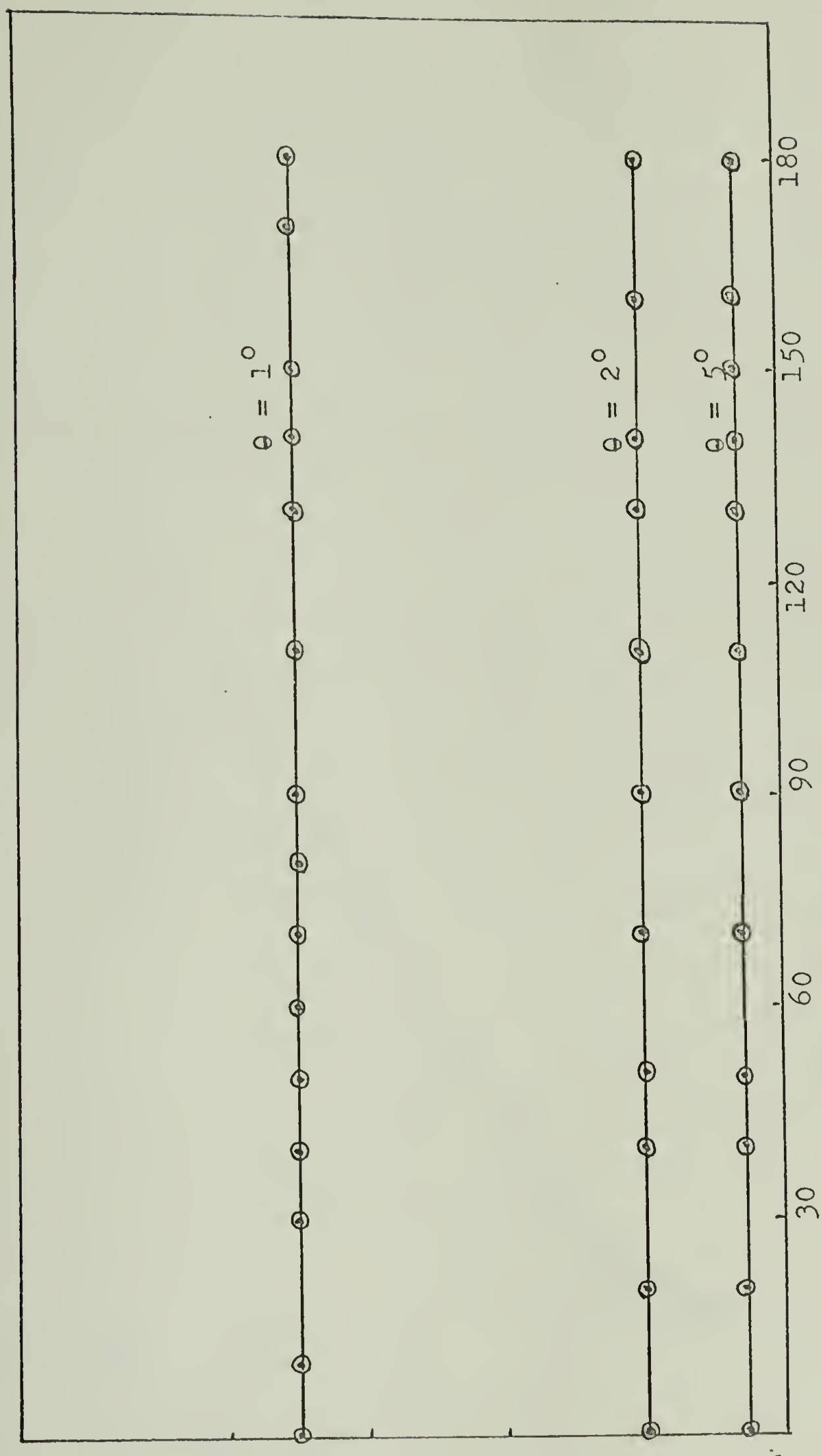

FIGURE IVF-2. VARIATION OF I_+ WITH Ψ FOR CHOLESTERYL MYRISTATE AT 82°C

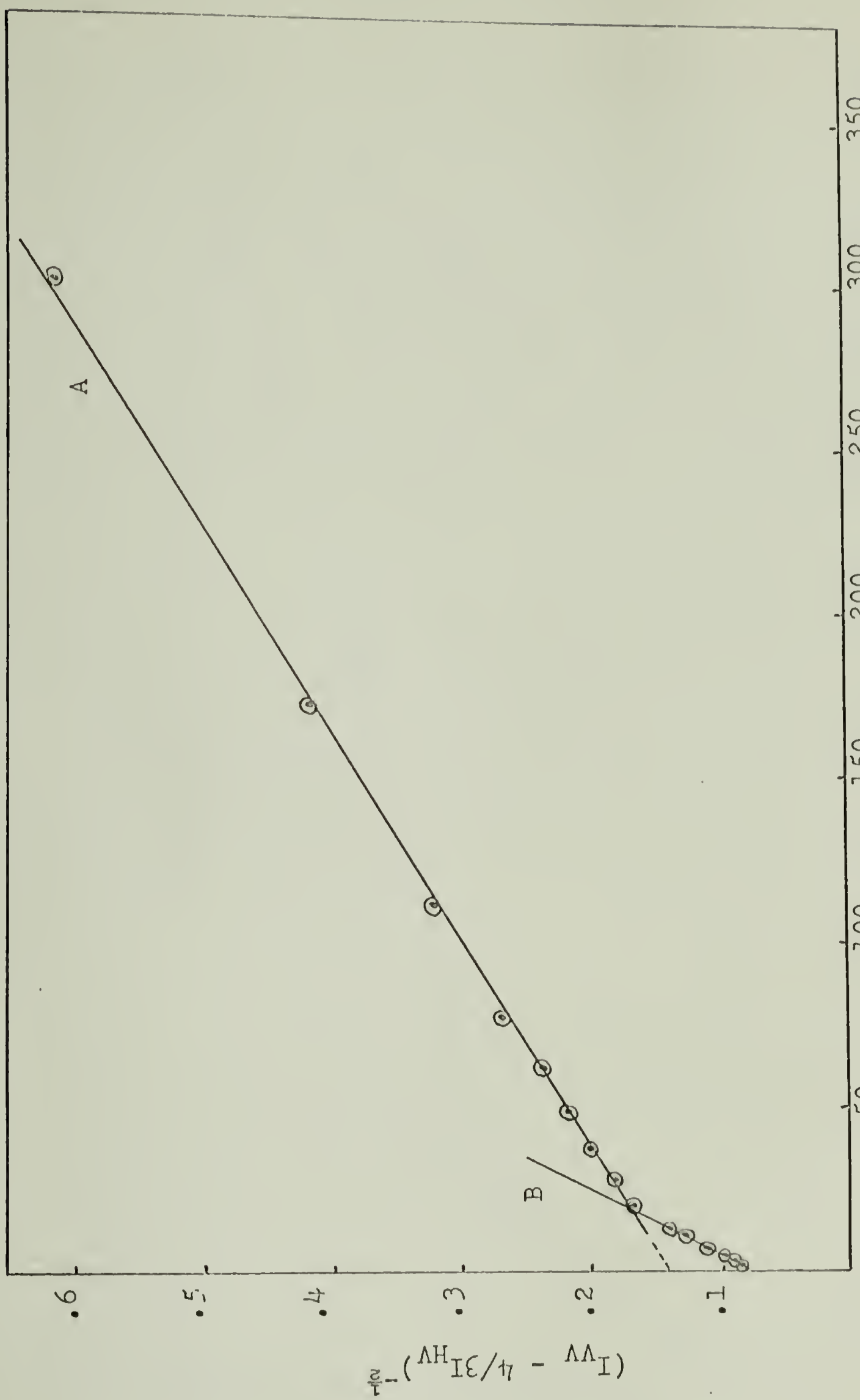

FIG. IVF-3. $(I_{VV} - 4/3I_{HV})^{-\frac{1}{2}}$ VS. $\sin^2(\theta/2)$ FOR DATA IN FIG. IVF-1

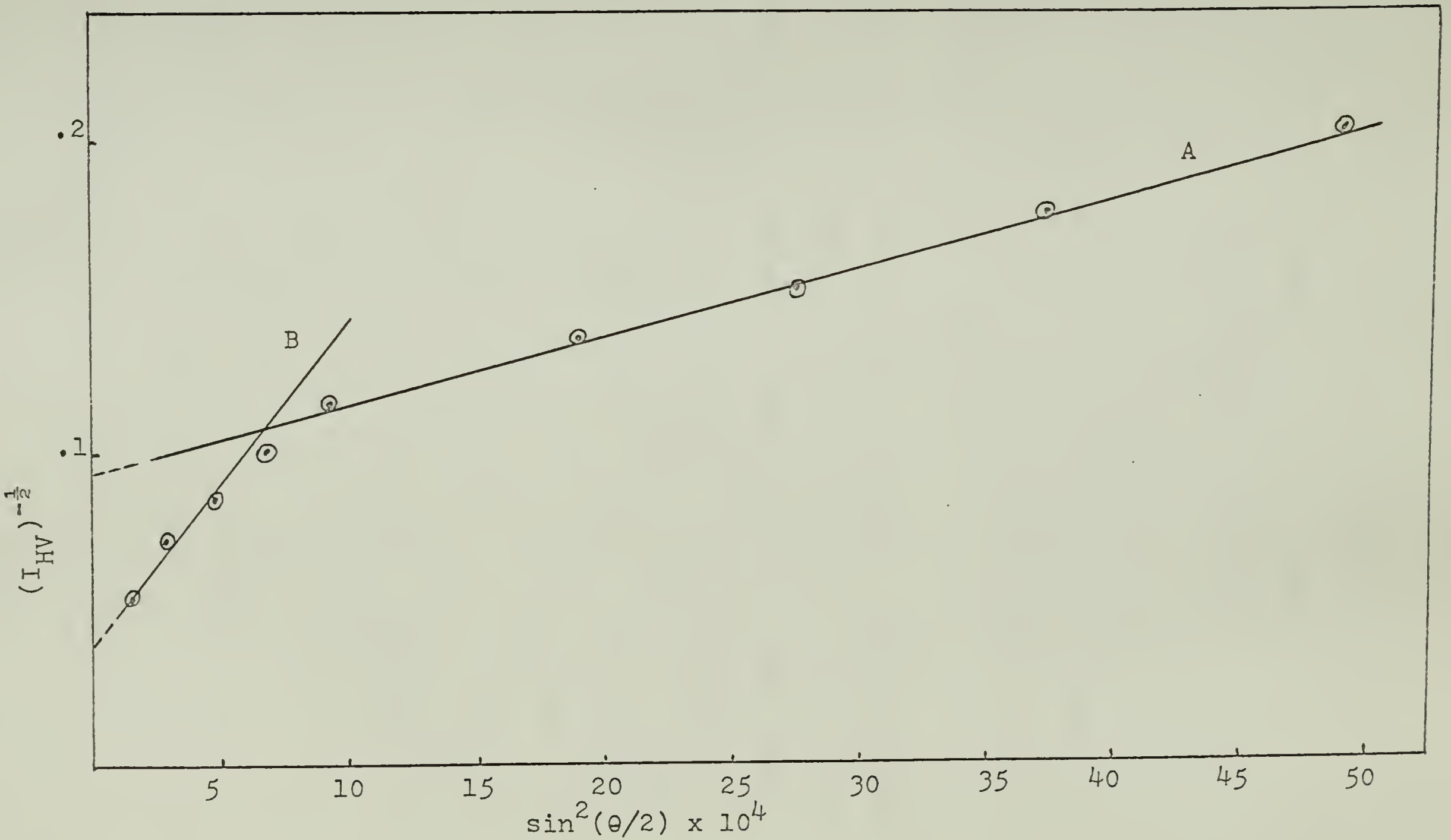

FIG. IVF-4. $(I_{HV})^{-\frac{1}{2}}$ VS. $\sin^2(\theta/2)$ FOR DATA IN FIGURE IVF-1

A P P E N D I X I

CALIBRATION OF THE LOW ANGLE LIGHT SCATTERING APPARATUS

A. Introduction

The scattering power of a material is usually defined in terms of the Rayleigh ratio of an infinitesimal element of volume, v:

$$R(\theta') = \frac{i(\theta')}{vI_o} r^2 \qquad (1)$$

where $i(\theta)$ is the average intensity of light scattered in a solid angle between θ' and $(\theta + d\theta')$ from the incident beam measured at a distance r away from the volume element.

In practice, one determines the scattering from a sample of finite volume in an instrument which has a response $T(\theta;\phi)$ which may be a potentiometer reading, a galvanometer or a recorder deflection, or a setting of an adjustable aperature.

Stein and Keane[60] developed the following expression for the determination of $R(\theta')$ from $T(\theta',\phi)$, taking into account the corrections for refraction, reflection, secondary scattering, intensity and volume correction.

$$R(\theta') = kr^2 I_o C_n R K_f T(\theta',\phi) \;/\; I'_\theta \cdot V_s \cdot t \qquad (2)$$

where k is a constant; I_o is the intensity of the incident beam; C_n is the refraction correction; K_f is the secondary scattering correction; I'_θ is the intensity correction; V_s is the actual scattering volume in the field of view of the photometer; t is the product of transmittances of filters in the

incident beam; $T(\theta',\phi)$ is the photometer response; r is the distance from the scattering volume to the detection point; and R is the reflection correction.

As seen from the equation 2, one can set $K=kr^2$. This is a constant characteristic of the apparatus. In order to obtain $R(\theta')$ from the photometer response one needs to determine K, the calibration constant. Before going on to describe the calibration procedure, a brief description of the apparatus is necessary.

B. Apparatus

The apparatus consists mainly of three parts. An optical component which produces a highly parallel incident beam; a light receiving photometer together with an amplifier for signal amplification; and a sample holder. A schematic diagram of the apparatus is shown in Figure 1.

The source of light is provided by a high pressure mercury lamp (GE H 100 A4) mounted in a lamp housing which is cooled by a water current. Immediately in front of the housing opening is a mechanical chopper (Princeton Applied Research, Princeton, N.J., Model BZ-1) in connection with a phase sensitive detector (Princeton Applied Research, Model JB-4). This arrangement inproves the signal to noise ratio by amplifying only the component of the photomultiplier output which is matched in phase and frequency with the chopper. The incident beam passes through a 57 mm. focal length lens, L_1, which

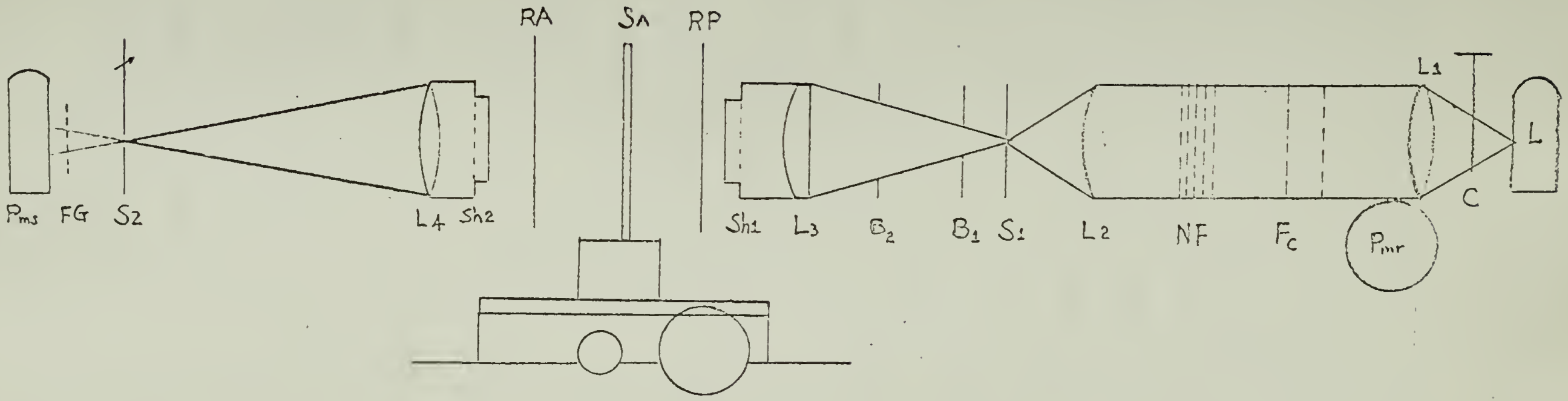

L, LAMP	L_3, COLLIMATING ACHROMATIC LENS
L_1, CONVERGING LENS	Sh_1, Sh_2, SHUTTERS
P_{mr}, REFERENCE PHOTOMULTIPLIER	RP, ROTATING POLARIZER
F_c, COLOR FILTER	S_A, SAMPLE HOLDER
N_F, NEUTRAL DENSITY FILTERS	RA, ROTATING ANALYZER
L_2, CONVERGING LENS	L_4, CONVERGING LENS
S_1, S_2, PINHOLES	FG, FROSTED GLASS
B_1, B_2, BAFFLES	P_{ms}, SIGNAL PHOTOMULTIPLIER

FIGURE 1. SCHEMATIC DIAGRAM OF THE LOW ANGLE LIGHT SCATTERING APPARATUS

gives a parallel beam. A set of monochromatic filters is provided to control the wavelength of the incident beam, followed by a set of neutral filters to control the intensity of the beam. The beam then passes through a converging lens of 30 mm. focal length and at the focus is a pinhole of two different sizes, 0.5 mm. and 1.5 mm. The two baffles are provided to block off the stray light. The beam passis again through a collimating achromatic lens of focal aength of 176 mm., which is followed by a photographic shutter and iris diaphragm to control the diameter of the incident beam. The incident beam is polarized by a rotating polarizer by which the angle Ψ_1 can be changed.

The scattered light receiving component is in principle similar to the incident beam producing component and it is composed of six parts. A rotating analyzer which controls the angle Ψ_2. A shutter with an iris diaphragm to control the scattered beam reaching the signal photomultiplier. A large lens of 183 mm. focal length and at its focus a pinhole with adjustable opening is located. A frosted glass piece is provided in order to randomize and diffuse the scattered beam before reaching the photomultiplier. This optical arrangement allows only scattered beam that is parallel to the incident beam to be received by the phototube and thus it is possible to make measurements in the presence of external light.

The light receiving component is mounted on a metal arm which con be rotated to vary the scattering angle θ' from 0^o

to 180°.

The sample holder is mounted on a metal wheel which can be rotated to vary the azimuthal angle.

C. Calibration

As mentioned above, it is necessary to calibrate the light-scattering in order to obtain an absolute value for the intensity of the scattered beam. The most usual and the best method is to make a measurement on a suitable scattering medium.

Requirements of a calibration medium.

1. All the light lost while passing through the solution must be due to scattering and none can be lost by absorption.
2. The solution must be stable and should not form aggregates for as long a time as is needed to perform the calibration.
3. The scattering particles must be small compared to the wavelength of light.
4. The particles must be optically isotropic.
5. The particles should be sufficiently dense in order to give reasonably high scattering power at the relatively low concentrations required for the calibration.

Ludox solution (suspension of colloidal silica) and benzene have been the most widely used media for calibration. However, since the apparatus has a high resolution the instrument is only capable of measuring the relatively high scattering from polymer films; it is not well suited for measuring the small scattering intensities of solution or solvents like

polystyrene solution or benzene. Ludox solution, on the other hand, has a relatively high scattering power at low concentrations and was therefore chosen for calibration purposes.

Material. The Ludox HS sample was supplied by E. I. duPont de Nemours & Co., Wilmington, Delaware; Massachusetts agent, Axton Cross Corporation, Halliston, Mass. Ludox solution is a suspension of colloidal silica of amorphous form with approximately spherical particles of diameter about 200 A^{o}. The following table shows the particle sizes for Ludox solution found by different methods.(61)

TABLE 1. PARTICLE SIZES OF LUDOX SOLUTION

Method	Particle size in A^{o}
electron microscope	199
ultracentrifuge	174
light-scattering	195
turbidity	195

The sample provided was a stock solution of 40% concentration. The samples were made up for study to the approximate concentrations of 1% and 2% by diluting the stock solution with distilled water and then filtering with ultrafine sintered-glass filters under nitrogen pressure of about 5 lb./sq.inch.

Determination of the calibration constant. The procedure was to measure the Rayleigh ratio of Ludox first on an already calibrated Brice Phoenix Light Scattering Photometer, Series

2000, and then the same solution was measured on the low angle apparatus.

The calibration constant is obtained from

$$R_L = K \cdot C_n \cdot T_L / V_L \qquad (3)$$

where R_L is the Rayleigh ratio for the Ludox solution. T_L is the instrument response for Ludox solution at 90^o. C_n is the refraction correction, which for a rectangular cell is equal to the square of the refractive index of Ludox solution, n_L^2. V_L is the actual scattering volume of Ludox. However, because of the refraction, the scattering volume seen by the photomultiplier will be larger than the calculated volume. Therefore, a volume correction, C_V, must be introduced where

$$C_V = V \text{ uncorrected} / V \text{ scattered.}$$

This correction factor has been worked out by Plaza.[62] The geometry of the C_V term is given in Figure 2, where I_o is the direction of the incident beam. b Is the diameter of the entrance aperature. C is the rectangular cell containing the Ludox solution. m Is the distance from the center to the edge of the cell. z Is the distance from the cell to the exit aperature. l Is the diameter of the exit aperature. x Is the refraction distance due to the angle θ. y Is the refraction distance due to the angle θ'. θ is the distance between the center of the lens and the outside diameter of the photomultiplier pinhole. θ' is the refraction angle which is approximated by θ/n, where n is the refractive index of the calibration liquid. D is the shutter on the photomultiplier side.

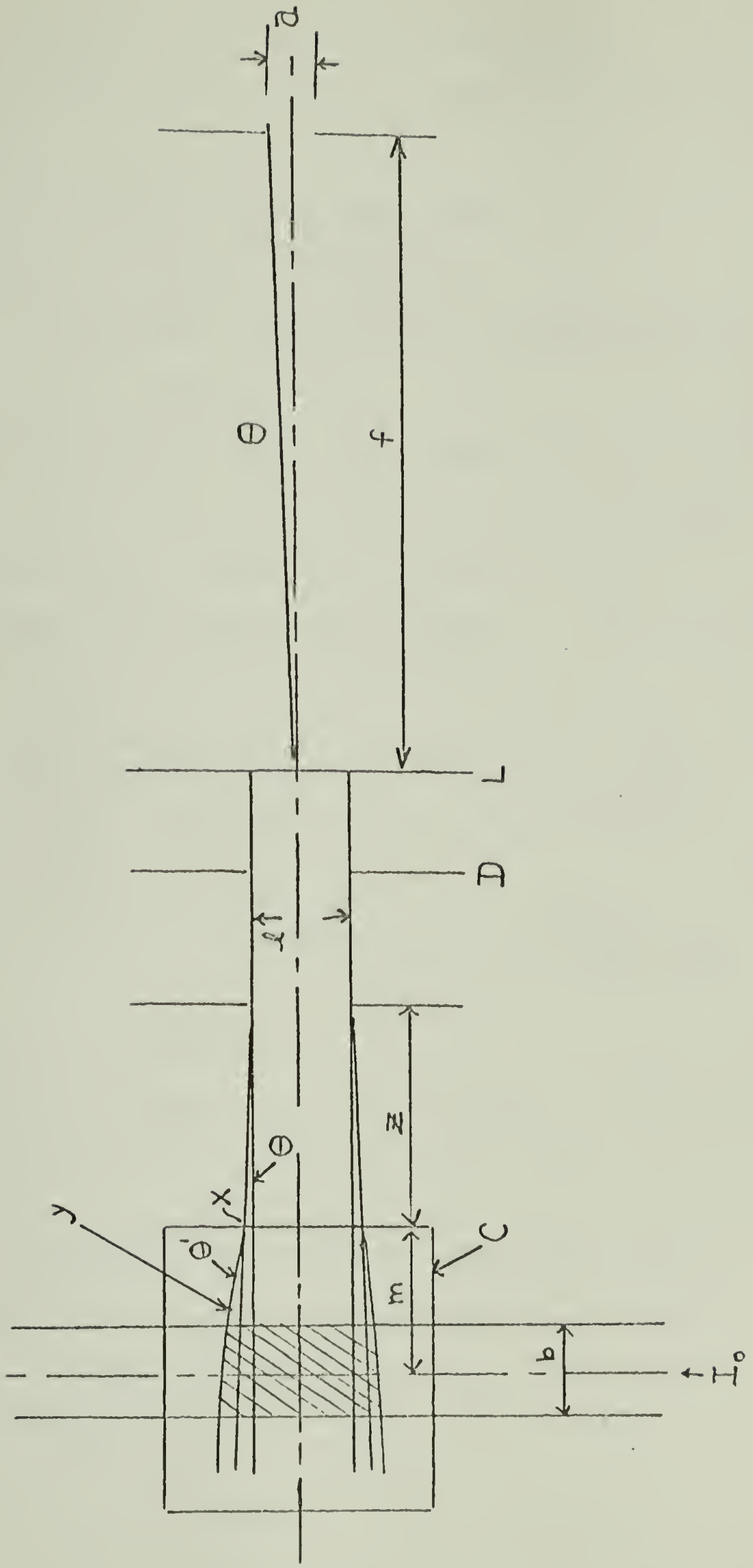

FIG. 2. C_V GEOMETRY

L is the lens on the photomultiplier side. f Is the focal length of the lens. a Is the diameter of the photomultiplier pinhole.

From Figure 2 it is seen that:

$$V_{\text{uncorrected}} = \pi(b/2)^2 \ell F \qquad (4)$$

$$V_{\text{scattered}} = \pi(b/2)^2 \ell' F = \pi(b/2)^2(\ell/C_v)F \qquad (5)$$

where $\ell' = \ell + 2x + 2y$ (6)

and F is a factor which takes into account that the volume common to two cylinders is not really a cylinder. The derivation of this factor will be shown below.

From the angular relationship, x and y can be estimated as:

$\tan \theta = a/2f = x/z$ and $x \cong az/2f$

$\tan \theta' = \tan(\theta/n_L) = y/m$ and $y \cong ma/2nf$

Therefore,

$$C_v = \ell/\ell' = \frac{\ell}{\ell + 2x + 2y} = \frac{\ell}{\ell + \frac{az}{f} + \frac{ma}{nf}}$$

In this instrument:

a = 1.22 mm.	z = 140 mm.	f = 183 mm.
m = 15 mm.	l = 19.4 mm.	n = 1.334

In order to calculate F, one should first calculate the volume common to the two intersecting cylinders.

Volume Common to Two Intersecting Cylinders.

Let B be the radius of the incident beam and A be the radius of the scattered beam. The geometry of the intersection is as follows:

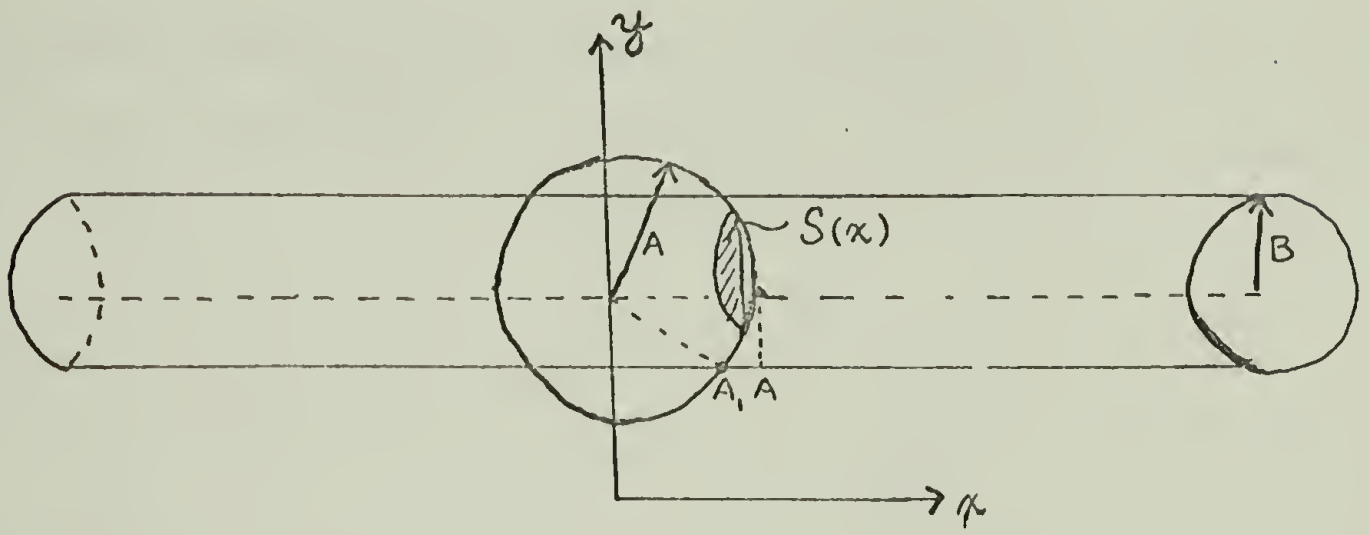

The volume of intersection is:

$$V = 2\int_0^{A_1} \pi B^2 dx + 4\int_{A_1}^{A} S(x)\, dx$$

where $A_1^2 = A^2 - B^2$ or $A_1 = (A^2 - B^2)^{\frac{1}{2}}$

After making the proper trigonometric substitution one has:

$$V = 2\pi B^2(A^2 - B^2)^{\frac{1}{2}} + 2B^2\int^{A} \{\text{Arcsin}\left[(A^2-x^2)^{\frac{1}{2}}/B\right] + (A^2-B^2)^{\frac{1}{2}}$$

$$(1/B^2)(A^2-x^2)^{\frac{1}{2}}(B^2-A^2+x^2)^{\frac{1}{2}}\} dx$$

Let $V_B = 2\pi B^2 A$ and $w = x/A$.

$$F = V/V_B = (A^2-B^2)^{\frac{1}{2}}/A + 1/\pi A \int_{\sqrt{A^2-B^2}}^{A} \{\text{Arcsin}\left[(A^2-x^2)^{\frac{1}{2}}/B\right] + 1/B^2(A^2-x^2)^{\frac{1}{2}}(B^2-A^2+x^2)^{\frac{1}{2}}\} dx$$

$$F = \left[1-(B/A)^2\right]^{\frac{1}{2}} + 1/\pi \left\{\int \text{Arcsin}\left[\frac{(1-w^2)^{\frac{1}{2}}}{B/A}\right] + A^2/B^2(1-w^2)^{\frac{1}{2}} \cdot (B^2/A^2 - 1 + w^2)^{\frac{1}{2}}\right\} dw$$

let $f = B/A$

then

$$F = (1-f^2)^{\frac{1}{2}} + 1/\pi \int_{\sqrt{1-f^2}}^{1} \left\{ \text{Arcsin}\left[(1-w^2)^{\frac{1}{2}}/f\right] + 1/f^2(1-w^2)^{\frac{1}{2}} (f^2-1+w^2)^{\frac{1}{2}} \right\} dw$$

The above equation was solved by computer for several values of f. The following is a table of the values of f and F.

f	F
.05	.9992
.10	.9969
.15	.9929
.20	.9874
.25	.9802
.30	.9713
.35	.9606
.40	.9480
.45	.9335
.50	.9169
.55	.8979
.60	.8763
.65	.8519
.70	.8242
.75	.7925
.30	.7559
.85	.7127
.90	.6600
.95	.5900

Figure 4 shows the plot of F versus f. From the curve, one can obtain the value of F for axial-ratios between .05 and .95.

Results.

The axial ratio for the incident beam to the scattered beam is 0.515. Now from Figure 4, the corresponding F value is 0.90. The true scattering volume is calculated from equation 5. The following is a table of the results:

CONCENTRATION	R_2 measured	C_v calc.by eq.7	$T(\theta,\phi)$ measured	V_L calc.by eq.5	K
1%	27.16×10^{-4}	0.951	3.5 (a)	$1.441cm^3$	6.27×10^{-4}
2%	44.05×10^{-4}	0.951	5.3 (b)	$1.441cm^3$	6.72×10^{-4}

(a) Back pinhole #3, front pinhole #1, signal .001

(b) Back pinhole #3, front pinhole #1, signal .001

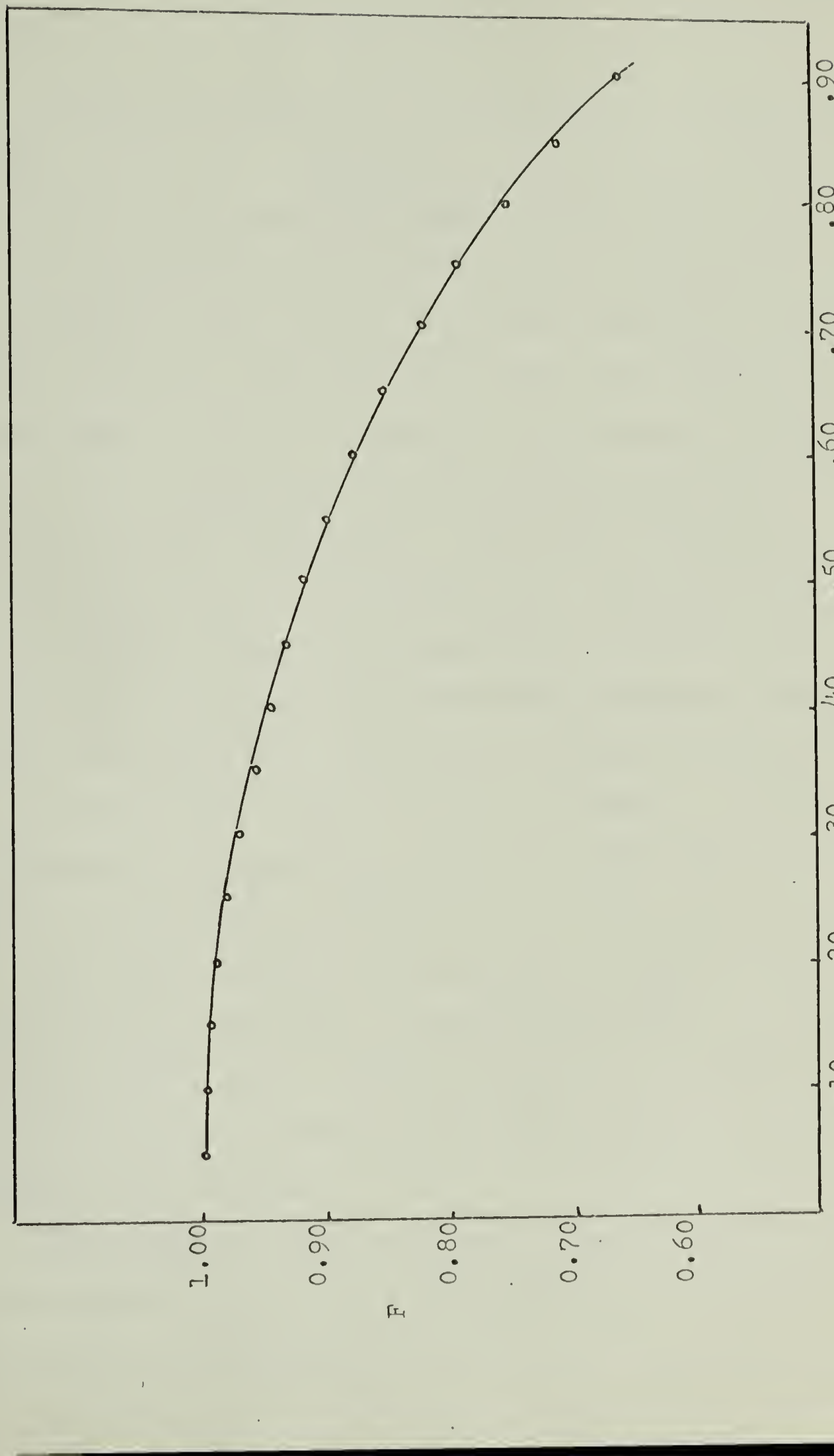

FIG. 4. RELATIONSHIP BETWEEN F AND f.

A P P E N D I X I I

HOT STAGE CELL

A schematic diagram of the hot stage cell is shown in Figures 1 through 3. The window is large enough to allow measurement of the scattered beam up to $\theta = 45^{o}$.

The main part of the oven (Figure 2) is constructed from two aluminum blocks in which four heater cartridges are imbedded. The inner two, each of 30 watts, are supplied constantly with current by a Variac. This current is regulated so that the temperature of the oven is approximately 10% below the desired temperature. The outer two heaters are fed by current which is also regulated by a Variac and which is controlled by an Electronic Temperature Controller, model 2158, product of Cole--Parmer Instrument Company. The temperature is measured by a thermocouple inserted in the block and it is very near the sample as shown in Figure 1. By this arrangement it is possible to keep the temperature of the oven constant within $\pm$ 0.1^{o}C.

The sample holder is illustrated in Figure 3. The sample, between cover slips, is sandwiched between two square aluminum sheets with a circular opening of 0.5 inches. The sample holder is fastened to the drawer which is in turn inserted into the oven.

The aluminum blocks were black anodized and the outer surfaces were enclosed with teflon sheets of thickness 0.125 inches for good insulation.

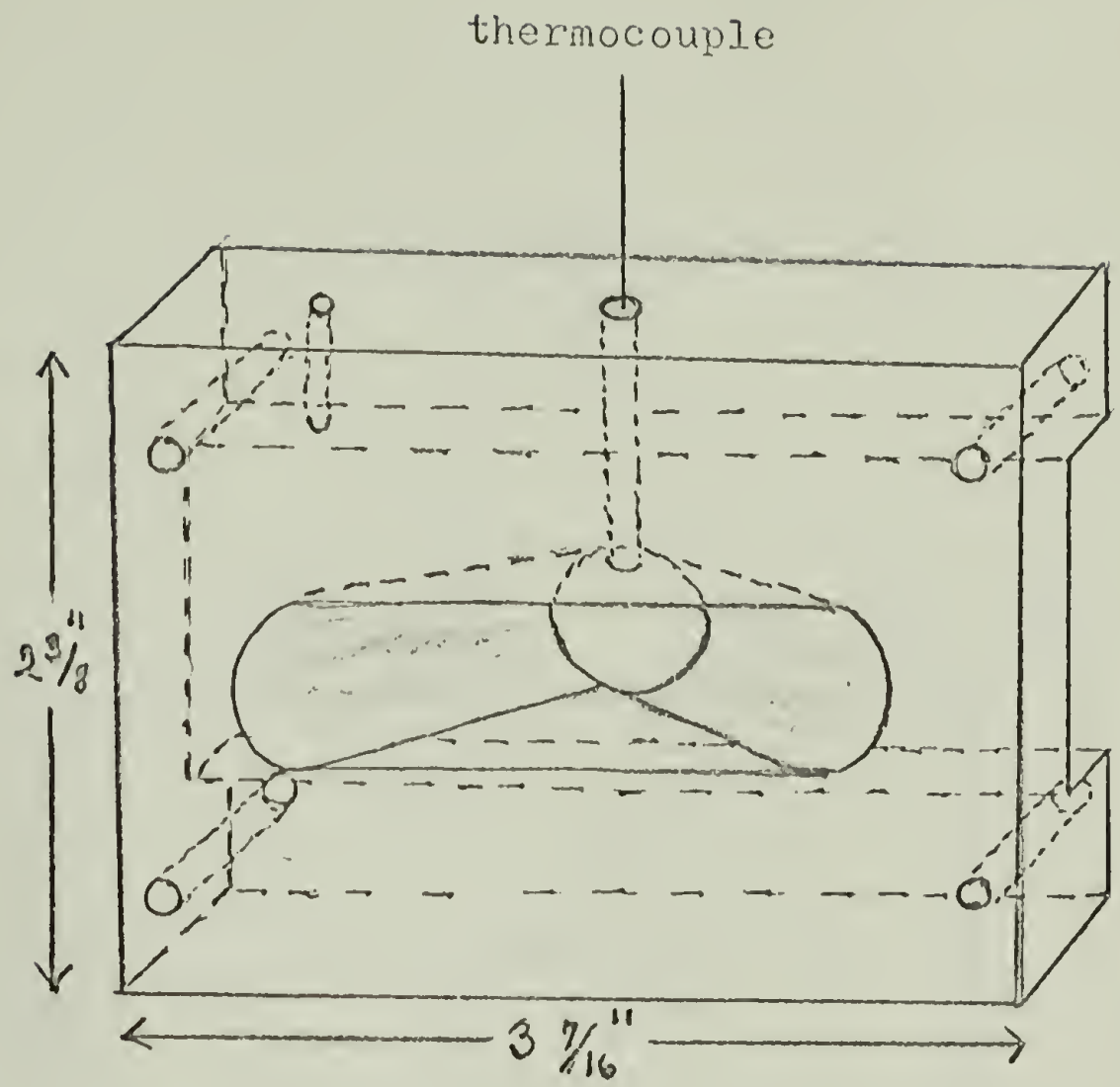

FIG. 1. FRONT VIEW OF THE HOT STAGE CELL

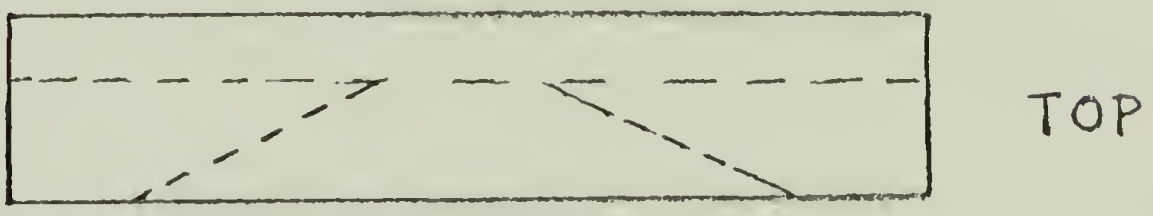

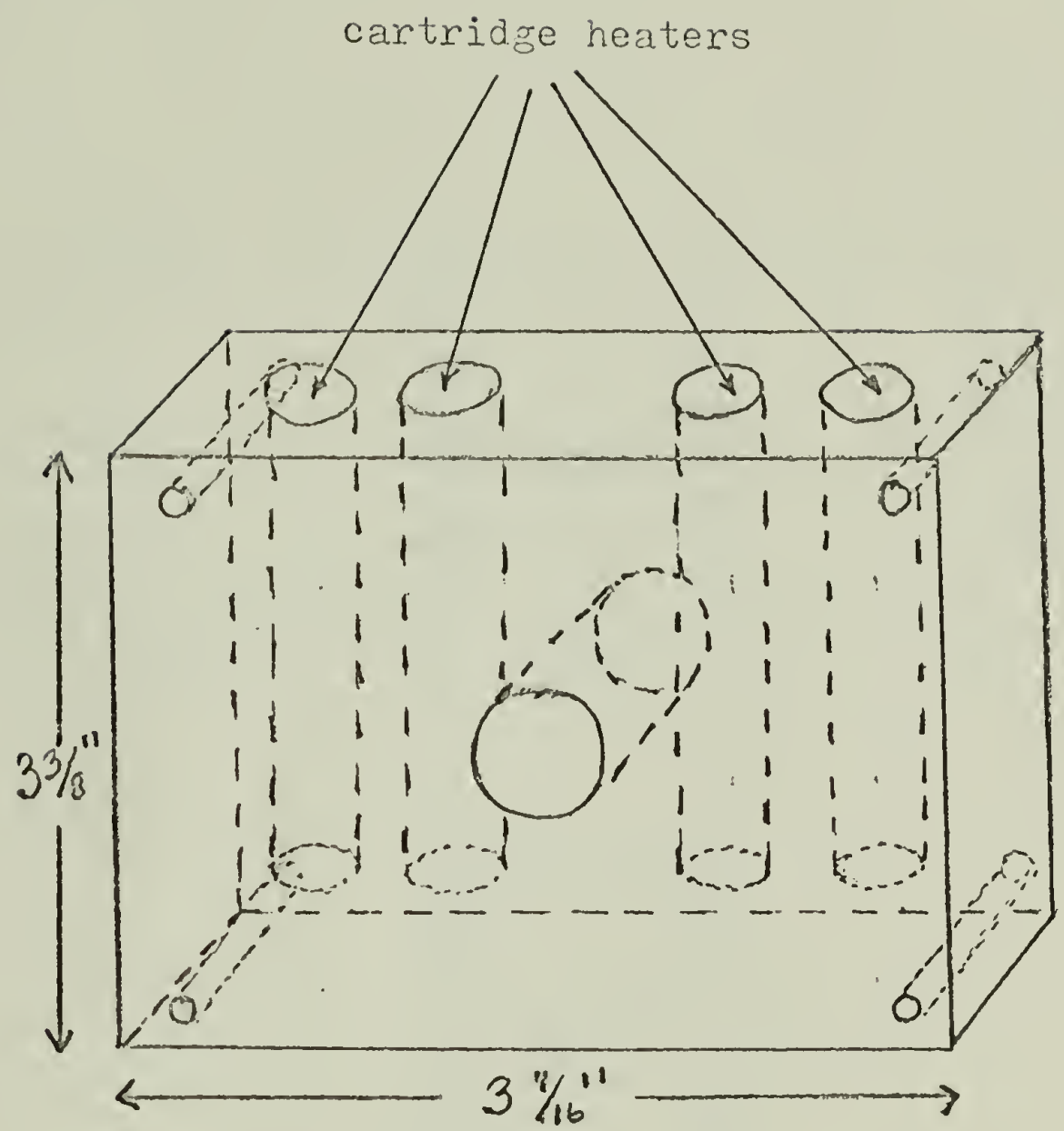

FIG. 2. CONSTANT TEMPERATURE OVEN

DRAWER

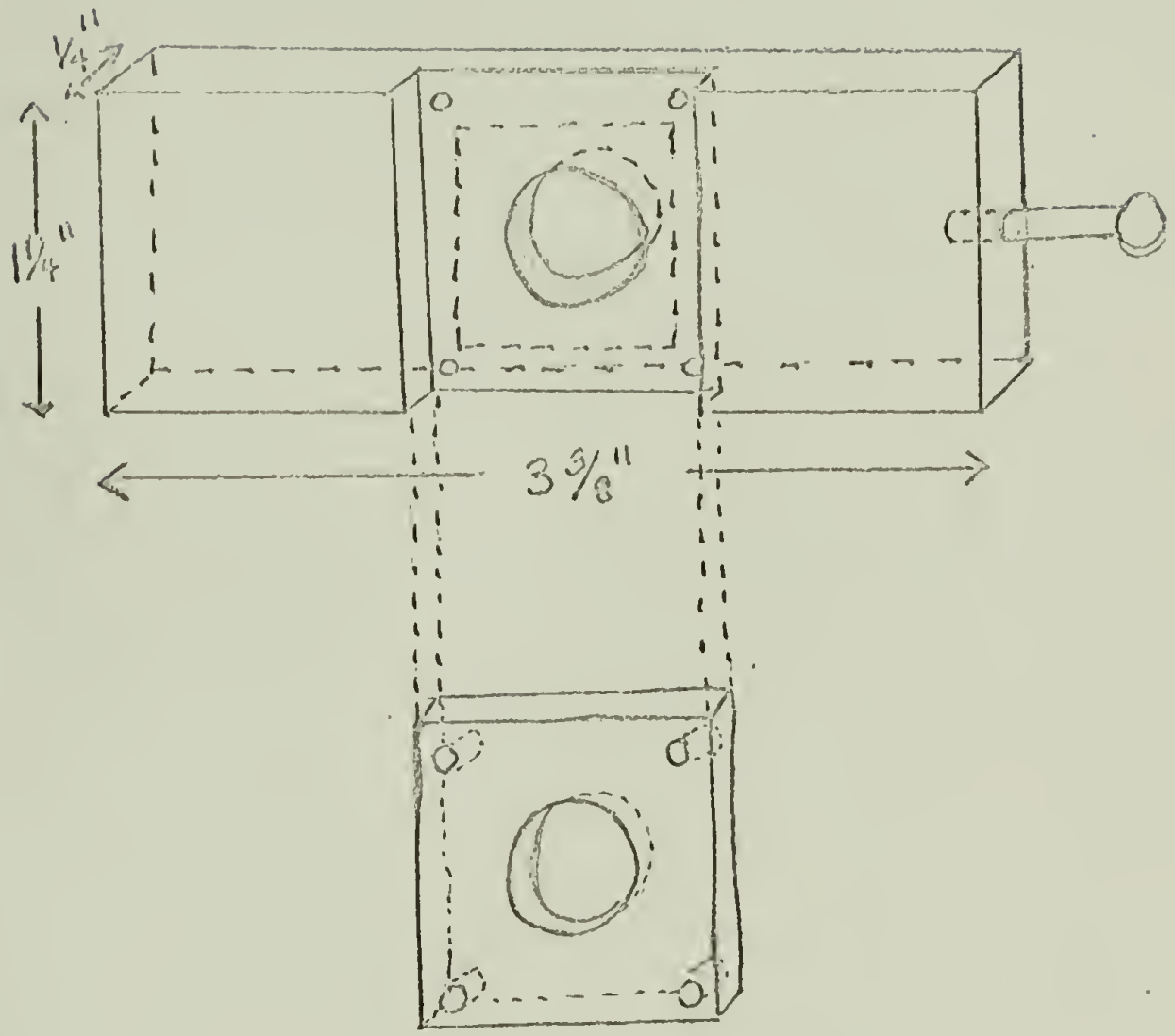

FIG. 3. SAMPLE HOLDER AND DRAWER